

Introduction to Gas-Turbine Design Analysis

Matthias Ihme

Stanford University

Version 3.0

January 14, 2025

© mihme@stanford.edu

Contents

Recommended Reading	4
Nomenclature	6
Chapter 1. Introduction	7
Chapter 2. Aerodynamics and Aircraft Performance	9
2.1. Aerodynamics: Drag, Lift, and Airfoil Theory	9
2.2. Aircraft Performance	14
2.3. Propulsive Thrust Generation	17
2.4. Fuel Consumption and Range Equation	21
2.5. Performance Parameters	23
2.6. Altitude Effects	26
Chapter 3. Thermodynamics	29
3.1. Conservation Equations	29
3.2. Thermodynamics of Gases	31
Chapter 4. Aircraft Jet Engines	39
4.1. General Gas Turbine Engine Concepts	39
4.2. Analysis of Turbojet Engines	42
4.3. Analysis of Turbofan Engines	48
4.4. Examples of Turbofan Engines	50
Chapter 5. Gas Turbine Engine Components	59
5.1. Combustion and Combustor	59
5.2. Turbomachinery	87
Chapter 6. Mechanical Design of Gas Turbines	111
6.1. Engine Development Cycle	111
6.2. Engine Loads	112
6.3. Failure Modes	113
6.4. Design Against Failure	117
6.5. Blade Design Criteria	118
Bibliography	123

Recommended Reading

Since this course covers material from different subject areas (including aerodynamics, thermodynamics, gas turbines, and specialized topics on internal combustion engines and rocket-propulsion), we are relying on different references. Below is a list of complementary reading material for this course; all books are on reserve at the library:

- Thermodynamics:
 - Cengel & Boles: Thermodynamics: An Engineering Approach, McGraw-Hill [1];
 - Reynolds & Perkins: Engineering Thermodynamics, McGraw-Hill [2].
- Aerodynamics:
 - Anderson: Introduction to Flight, McGraw-Hill [3];
 - Anderson: Modern Compressible Flow, McGraw-Hill [4].
- Gas Turbine Engines
 - Mattingly: Elements of Propulsion: Gas Turbines and Rockets, AIAA Ed. Series. [5] (Recommended Text)
 - Saravanamuttoo, Rogers, Cohen, & Straznicky: Gas Turbine Theory, Pearson [6]
 - Hill & Peterson: Mechanics and Thermodynamics of Propulsion, Addison-Wesley [7];
 - Lefebvre: Gas Turbine Combustion, Taylor & Francis [8];
 - Farokhi: Aircraft Propulsion, Wiley [9];
 - Cumpsty: Jet Propulsion – A Simple Guide to the Aerodynamic and Thermodynamic Design and Performance of Jet Engines, Cambridge University Press [10];
 - Rolls Royce: The Jet Engine – A Complete Overview of the Modern Gas Turbine [11].
 - Dixon & Hall: Fluid Mechanics and Thermodynamics of Turbomachinery, Butterworth-Heinemann (also available as online resource: <http://www.sciencedirect.com/science/book/9780124159549>)
 - Online resource to Jane's aero engines: <https://janes.ihs.com>
- Internal Combustion Engines:
 - Heywood: Internal Combustion Engine Fundamentals, McGraw-Hill [12];
 - Stone: Introduction to Internal Combustion Engines, Palgrave MacMillan [13];
 - Lumley: Engines – An Introduction, Cambridge University Press [14].
- Rocket Propulsion
 - Sutton & Biblarz: Rocket Propulsion Elements, Wiley [15];

- Huzel & Huang: Modern Engineering for Design of Liquid-Propellant Rocket Engines, American Institute of Aeronautics and Astronautics [16].

Nomenclature

Symbol	Description	Value	Units
H	Enthalpy	-	J
M (or W)	Molecular weight	-	g/mol
N_A	Avogadro constant	6.022×10^{23}	mol^{-1}
N	Number of particles/molecules	-	-
Q	Heat	-	J
R	Gas constant	-	J/(g K)
S	Entropy	-	J/K
T	Temperature	-	K
T	Thrust	-	N
U	Internal energy	-	J
V	Volume	-	m^3
$V_m = V/n$	Molar volume	-	m^3/mol
X_i	Mole fraction of species i	-	-
Y_i	Mass fraction of species i	-	-
$c_{\{p,v\}}$	Specific heat at constant {pressure, volume}	-	J/(kg K)
k_B	Boltzmann constant	1.3806×10^{-23}	J/K
m	Mass	-	g
n	Number of moles	-	mol
p	Pressure	-	Pa
\mathbf{u}, u	Velocity	-	m/s
ρ	Density	-	g/m^3
ν_i	Stoichiometric coefficient, mole number of species i	-	-
ϕ	(fuel-oxygen/air) equivalence ratio	-	-
$\widehat{(\cdot)}$	mole-specific quantity	-	-
$(\cdot)'$	particle-specific quantity	-	-
\mathcal{E}	Total Energy	-	-
\mathcal{R}	Universal gas constant	8.314	J/(mol K)

Introduction

In this course, we will conduct a propulsion design analysis by considering three different propulsion systems, namely (i) a propeller-driven internal combustion engine, (ii) a turbojet engine, and (iii) a single-stage liquid rocket engine. Performance, efficiency, and other characteristics (emissions, fuel-utilization, and noise, etc) will be investigated in the specific context of a small four-seat private aircraft (similar to the Cirrus SR-22). The aircraft is illustrated in Fig. 1.1 and aircraft specifications are summarized in Table 1. The primary focus of this course is on the engine design analysis of gas turbines with specific consideration of turbojet and turbofan engines.



Figure 1.1: Cirrus SR22.

Performance	
Climb Rate	6.45 m/s
Max. operating altitude	5,334 m
Max. cruise speed	340 km/h
Weight Certification	
Max. takeoff mass	1542 kg
Empty mass	1021 kg
Maximum load	521 kg
Full fuel payload	307 kg
Wings	
Wing span	11.67 m
Wing area	13.5 m ²

Table 1: Specifications of Cirrus SR22.

The following specific engine design concepts are of interest for aircraft engines:

- Scenario 1: Internal combustion engine
 - Propeller-driven IC-engine;
 - Single six-cylinder four-stroke engine;
 - Example: Cessna 350 Corvalis (Fig. 1.2(a)); engine: Teledyne Continental IO-550-N.
- Scenario 2: Gas-turbine engine
 - Turbo-fan engine;
 - Two-stage compressor/turbine;

- Example: Honda HA-420 HondaJet ([Fig. 1.2\(b\)](#)); engine: GE Honda HF120.
- Scenario 3: Rocket-propelled engine
 - Single-stage rocket booster;
 - Fuels: solid, liquid, hybrid fuels;
 - Example: Messerschmitt Me 163 ([Fig. 1.2\(c\)](#)); engine: HWK 109-509.



(a) Cessna 350 Corvalis.



(b) Honda HA-420 HondaJet.



(c) Messerschmitt ME-163 Komet.

Figure 1.2: Examples of different aircraft propulsion systems: (a) propeller-driven IC-engine: Cessna 350 Corvalis, (b) turbofan engine: Honda HA-420 HondaJet, and (c) rocket-engine: Messerschmitt ME-163 Komet.

Aerodynamics and Aircraft Performance

This section provides basic theoretical understanding about the aircraft performance analysis. Using this theory will allow us to evaluate basic requirements for engine design analysis, including thrust, take-off and landing, and cruise performance. To link basic thrust requirements to the engine performance, we will then derive the thrust equation and propeller theory to determine engine performance requirements.

2.1. Aerodynamics: Drag, Lift, and Airfoil Theory

The aerodynamic analysis closely follows Secs. 5 and 6 of Anderson [3]. Here we consider an infinitely long airfoil. Forces acting on the airfoil, relevant to our analysis, include the lift and drag (see Fig. 2.1).

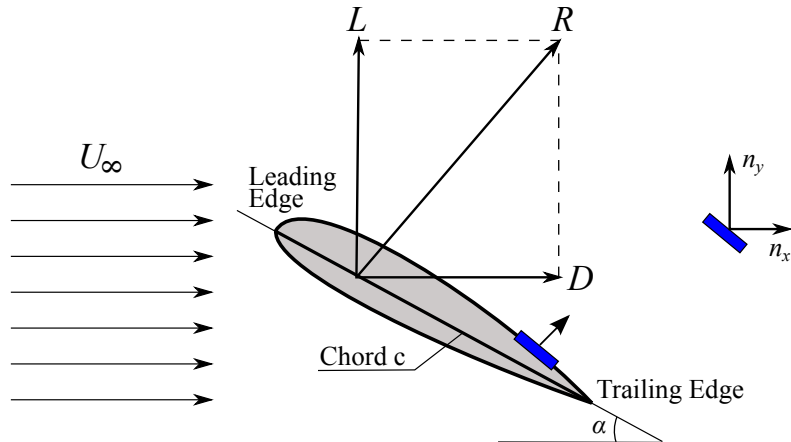


Figure 2.1: Forces on an airfoil with U_∞ : free-stream velocity; α angle of attack; L lift force; D drag force; and c : chord.

The *lift force* is defined as the force on an airfoil acting in the perpendicular direction to flight path (neglecting viscous stress contributions):

$$\begin{aligned} L &= - \oint p \mathbf{n}_y \cdot d\mathbf{A} \\ &= \int_0^c p \mathbf{n}_y \cdot d\mathbf{A} \Big|_{\text{lower side}} - \int_0^c p \mathbf{n}_y \cdot d\mathbf{A} \Big|_{\text{upper side}}. \end{aligned} \quad (2.1)$$

The *lift coefficient* is defined as

$$C_L = \frac{L}{q_\infty S}, \quad (2.2)$$

where the dynamic pressure q_∞ is defined as

$$q_\infty = \frac{1}{2} \rho_\infty U_\infty^2. \quad (2.3)$$

Similarly, we can also define the *sectional lift coefficient*

$$c_l = \frac{l}{q_\infty c}, \quad (2.4)$$

where l is the lift per unit length, and c is the chord.

Similarly, the *drag force* is the force on an airfoil acting in the parallel direction to the flight path (neglecting viscous stress contributions):

$$\begin{aligned} D &= - \oint p \mathbf{n}_x \cdot d\mathbf{A} \\ &= \int_0^c p \mathbf{n}_x \cdot d\mathbf{A} \Big|_{\text{lower side}} - \int_0^c p \mathbf{n}_x \cdot d\mathbf{A} \Big|_{\text{upper side}}. \end{aligned} \quad (2.5)$$

The *drag coefficient* and *sectional drag coefficient* are defined as:

$$C_D = \frac{D}{q_\infty S} \quad \text{and} \quad c_d = \frac{d}{q_\infty c}. \quad (2.6)$$

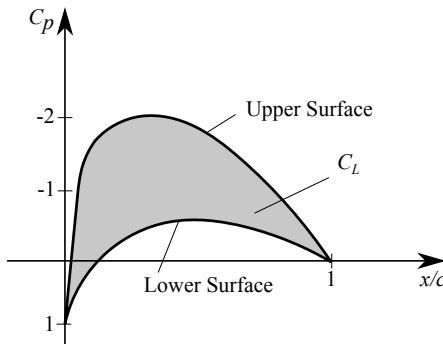


Figure 2.2: Pressure distribution over airfoil. Note that the area confined between lower and upper pressure curve is equal to C_L .

For completeness, we also introduce the *pressure coefficient* C_p :

$$C_p = \frac{p - p_\infty}{q_\infty}. \quad (2.7)$$

A typical pressure distribution over an airfoil is illustrated in Fig. 2.2. The steady Bernoulli equation, $p + q = \text{const}$ (with $q = \frac{1}{2}\rho U^2$), allows us to qualitatively rationalize the airfoil pressure distribution.

Note that lift and drag forces are functions of operating conditions and the airfoil geometry (see Fig. 2.3). This dependence can be written in terms of the following non-dimensional groups

$$L = f(\alpha, M_\infty, Re, \dots), \quad (2.8)$$

with α the angle of attack, M_∞ the free-stream Mach-number, and Re the Reynolds number (defined with respect to the chord-length).

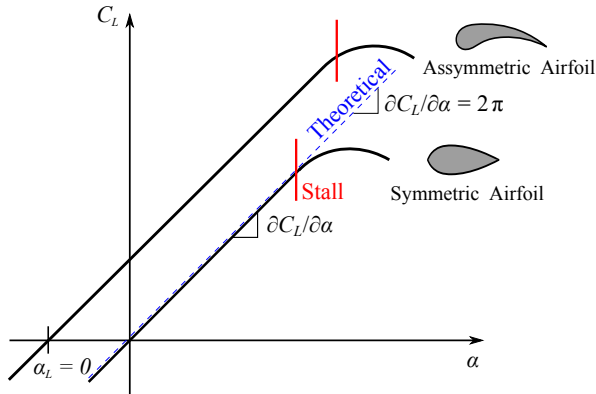


Figure 2.3: Airfoil lift curve.

From thin airfoil theory [3] with the assumptions (i) $M_\infty \ll 1$ and (ii) $Re \rightarrow \infty$ (inviscid), we can relate the lift-coefficient to the angle of attack:

$$c_l = a_0(\alpha - \alpha_0), \quad (2.9)$$

where

$$a_0 = \frac{\partial c_l}{\partial \alpha} = 2\pi. \quad (2.10)$$

Fig. 2.4 shows a thin airfoil with vortex sheet place along the camber line. The distance measured along the camber line is denoted by s . The shape of the camber line is given by $z = z(x)$. U_∞ is the free stream velocity, with the angle of attack α . $U_{\infty,n}$ and $w'(s)$ are the velocity component normal to the camber line by the free stream and the vortext sheet respectively. Assuming that the camber line is a streamline, then

$$U_{\infty,n} + w'(s) = 0 \quad (2.11)$$

at every point along the camber line.

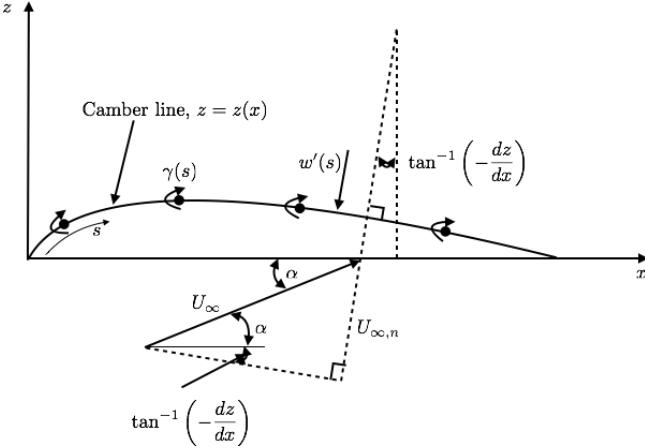


Figure 2.4: Thin airfoil and vortex sheet.

From the geometry, and assume the thin airfoil is at small angle of attack, $\tan^{-1}(-dz/dx) \approx -dz/dx$, we have

$$U_{\infty,n} = U_\infty \sin \left[\alpha + \tan^{-1} \left(-\frac{dz}{dx} \right) \right] \quad (2.12)$$

$$= U_\infty \left(\alpha - \frac{dz}{dx} \right). \quad (2.13)$$

For a thin airfoil, the camber line is close to the chord line, thus $w'(s) \approx w(x)$. The velocity dw at point x induced by the elemental vortex at point ξ is given as:

$$dw = -\frac{\gamma(\xi)d\xi}{2\pi(x-\xi)}. \quad (2.14)$$

$w(x)$ can be obtained by integrating Eq. (2.14) from the leading edge $\xi = 0$ to the trailing edge $\xi = c$, which is

$$w(x) = - \int_0^c \frac{\gamma(\xi)d\xi}{2\pi(x-\xi)}. \quad (2.15)$$

Substituting Eqs. (2.13) and (2.15) into Eq. (2.11) yields the *fundamental equation of thin airfoil theory*, which is

$$\frac{1}{2\pi} \int_0^c \frac{\gamma(\xi)d\xi}{x-\xi} = U_\infty \left(\alpha - \frac{dz}{dx} \right). \quad (2.16)$$

For a symmetric airfoil, $dz/dx = 0$, and Eq. (2.16) becomes:

$$\frac{1}{2\pi} \int_0^c \frac{\gamma(\xi)d\xi}{x-\xi} = U_\infty \alpha. \quad (2.17)$$

Introduce coordinate transformation

$$\xi = \frac{c}{2}(1 - \cos \theta). \quad (2.18)$$

Note that x is a fixed point which corresponds to a particular value θ_0 , which is

$$x = \frac{c}{2}(1 - \cos \theta_0). \quad (2.19)$$

With this, Eq. (2.17) becomes

$$\frac{1}{2\pi} \int_0^\pi \frac{\gamma(\theta) \sin \theta d\theta}{\cos \theta - \cos \theta_0} = U_\infty \alpha. \quad (2.20)$$

From the mathematical theory of integral equations,

$$\gamma(\theta) = 2\alpha U_\infty \frac{1 + \cos \theta}{\sin \theta}. \quad (2.21)$$

Note that $\gamma(\theta)$ satisfies the Kutta condition

$$\lim_{\theta \rightarrow \pi} \gamma(\theta) = 2\alpha U_\infty \frac{-\sin \pi}{\cos \pi} = 0. \quad (2.22)$$

Integrating $\gamma(\xi)$ from 0 to c yields the total circulation around the airfoil, which is

$$\Gamma = \int_0^c \gamma(\xi) d\xi \quad (2.23)$$

$$= \frac{c}{2} \int_0^\pi \gamma(\theta) \sin(\theta) d\theta \quad (2.24)$$

$$= \pi \alpha c U_\infty. \quad (2.25)$$

The lift per unit span is

$$L = \rho_\infty U_\infty \Gamma = \pi \alpha c \rho_\infty U_\infty^2. \quad (2.26)$$

The lift coefficient is then

$$c_l = \frac{L}{q_\infty c} = \frac{\pi \alpha c \rho_\infty U_\infty^2}{\frac{1}{2} \rho_\infty U_\infty^2 c} = 2\pi\alpha. \quad (2.27)$$

This yields the theoretical lift slope, which is

$$a_0 = \frac{\partial c_l}{\partial \alpha} = 2\pi. \quad (2.28)$$

The lift, drag and pressure-coefficients are typically obtained from measurements or computations of an “infinite wing span”, meaning that there are no losses due to the finite wing-span considered. To account for finite-wing effects due to the *induced drag* (i.e. pressure difference across wing tip and wing-tip vortices), we can separate the drag coefficient into two contributions:

$$\underbrace{C_D}_{\text{Total Drag}} = \underbrace{C_{D,0}}_{\text{Profile Drag}} + \underbrace{C_{D,i}}_{\text{Induced Drag}}, \quad (2.29)$$

where the *profile drag* consists of contributions from (i) skin friction, (ii) pressure drag, and (iii) flow-separation. The downwash due to tip-vortex-generation contributes to the induced drag. Another induced-drag contribution, that we typically neglect in our analysis, is the *wave drag*, which becomes relevant for transonic and supersonic flight conditions.

For the specific case of an elliptic lift distribution, we can employ Prandtl's lifting-line theory to find an analytic expression that relates $C_{D,i}$ to the lift coefficient:

$$C_{D,i} = \frac{C_L^2}{\pi e AR}, \quad (2.30)$$

where the aspect ratio AR is expressed in terms of the wing span b and wing area S as:

$$AR = \frac{b^2}{S} = \frac{b}{c}, \quad (2.31)$$

and the span efficiency factor is

$$e = \begin{cases} 1 & \text{for elliptic lift distribution} \\ < 1 & \text{for general case} \end{cases}. \quad (2.32)$$

The derivation of Eq. (2.30) is out of the scope for this course. Readers who are interested in the derivation of this relation may refer to Chapter 5.3 in book *Fundamentals of Aerodynamics* by J. Anderson for details. Upon inserting Eq. (2.30) into Eq. (2.29) we can derive the so-called *drag polar*:

$$C_D = C_{D,0} + \frac{C_L^2}{\pi e AR}, \quad (2.33)$$

which provides a relation between lift, profile drag, and total drag acting on an airfoil. A schematic of the drag polar is shown in Fig. 2.5.

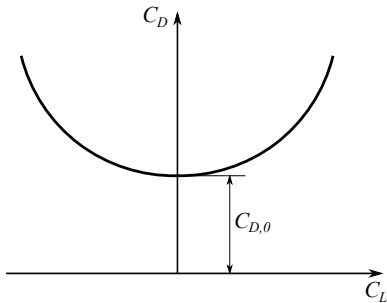


Figure 2.5: Drag polar.

2.2. Aircraft Performance

2.2.1. Extension of Lift and Drag Coefficients. This section extends the aerodynamic analysis that we performed by considering an isolated airfoil to the entire aircraft. For this, we are including additional effects and contributions due to lift and drag, arising from the airfoil, fuselage, tail flaps, landing gear, and nacelle by extending the notion of C_D and C_L . Following this spirit, we now define C_L

as the *total lift coefficient* (that includes contributions from the above-mentioned components). The drag-coefficient of the complete aircraft is then defined as

$$C_D = C_{D,0} + \frac{C_L^2}{\pi e AR} \quad (2.34)$$

where $C_{D,0}$ is the zero-lift drag coefficient of the entire aircraft (see Fig. 2.5), and e is the Oswald efficiency factor.

The resulting drag polar of the aircraft is shown in Fig. 2.6.

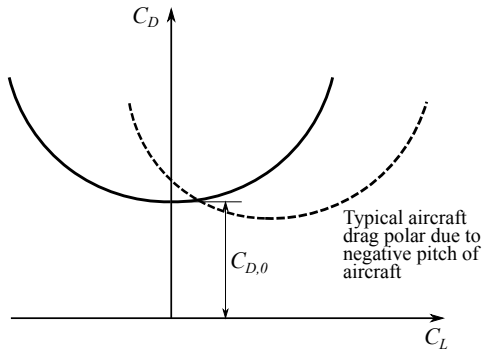


Figure 2.6: Drag polar of aircraft, defined by Eq. (2.34). Note that the minimum drag coefficient is shifted to $C_L > 0$, since the zero-lift angle, $\alpha_{L=0}$, is often negative due to the downward pitch of the aircraft (a good example for this can be seen by the titled engines on an MD-80). Although rarely considered, lift is also generated at negative C_L due to the fact that $\alpha_{L=0} < 0$.

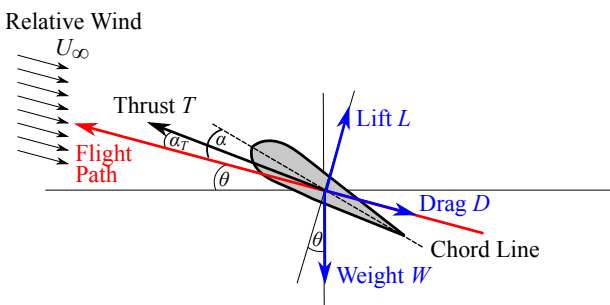


Figure 2.7: Force balance on aircraft with α : angle-of-attack; θ : inclination angle of flight path with respect to horizontal; α_T : thrust-angle; W : weight; L : lift (perpendicular to flight path); D : drag (parallel to flight path); and T : thrust.

2.2.2. Force Balance and Thrust Requirements. From the force balance on an aircraft (see Fig. 2.7) we can set up the *force balance parallel to the flight path*:

$$\sum_i F_i^{\parallel} = m \frac{dU}{dt} \Rightarrow T \cos \alpha_T - W \sin \theta - D = m \frac{dU}{dt}, \quad (2.35)$$

and the *force balance perpendicular to the flight path*:

$$\sum_i F_i^{\perp} = m \frac{U^2}{r_c} \Rightarrow L + T \sin \alpha_T - W \cos \theta = m \frac{U^2}{r_c}, \quad (2.36)$$

where r_c is the radius of the flight path (inverse of curvature of flight path).

We have some remarks and simplifications of the force balance equations:

- Note that $m = m(t)$, since we consume fuel during the flight:

$$m(t) = m_0 - \int_0^t \dot{m}_{fuel} dt; \quad (2.37)$$

- Since \dot{m}_{fuel} is typically small compared to the airframe mass for air-breathing propulsion systems, we can typically neglect these effects;
- Often we can invoke the following sequence of simplifications:
 - For the case of steady-state flight conditions, we have $d_t U = dU/dt = 0$:

$$T \cos \alpha_T - W \sin \theta - D = 0 \quad (2.38a)$$

$$L + T \sin \alpha_T - W \cos \theta = m \frac{U^2}{r_c} \quad (2.38b)$$

- (b) Thrust vector aligned with flight path ($\alpha_T = 0$)

$$T - W \sin \theta - D = 0 \quad (2.39a)$$

$$L - W \cos \theta = m \frac{U^2}{r_c} \quad (2.39b)$$

- (c) Level flight: $r_c \rightarrow \infty; \theta = 0$

$$T - D = 0 \quad (2.40a)$$

$$L - W = 0 \quad (2.40b)$$

This reduced set of force-balance equations will be the basis for the subsequent analysis. If necessary individual assumptions can be relaxed to introduce more complexity.

The thrust and lift requirements for steady-level flight are:

$$T = D = C_D q_{\infty} S \quad (2.41a)$$

$$L = W = C_L q_{\infty} S. \quad (2.41b)$$

By taking the ratio of both equations, we have an expression for the *required thrust*:

$$T^* = W \frac{D}{L} = W \frac{C_D}{C_L}, \quad (2.42)$$

and with the drag polar from Eq. (2.34), we can write:

$$T^* = \underbrace{C_{D,0}q_\infty S}_{\text{zero-lift drag}} + \underbrace{\frac{W^2}{q_\infty S \pi e A R}}_{\text{lift-induced drag}} . \quad (2.43)$$

The required thrust and thrust components vs. dynamic pressure are illustrated in Fig. 2.8.

The dependence of the thrust requirements on the angle of attack can be reconciled by introducing the expression for C_L from thin airfoil theory, $C_L = a(\alpha - \alpha_0) = 2\pi(\alpha - \alpha_0)$, into the thrust equation:

$$T^* = C_{D,0}q_\infty S + \frac{[2\pi(\alpha - \alpha_0)]^2 q_\infty S}{\pi e A R} . \quad (2.44)$$

2.2.3. Available Thrust. The thrust that is provided by the engine (propeller-driven IC-engine and gas turbine, etc.) must match or exceed the required thrust. We will see later that different propulsion systems have different thrust characteristics and limitations (see Fig. 2.9) and the maximum flight speed and cruise altitude is then determined by the available thrust of the aircraft.

Note that while gas-turbines are typically rated by thrust, the performance of IC-engines is typically specified in terms of power; required flight power and thrust are related through the following expression:

$$P^* = T^* U_\infty . \quad (2.45)$$

2.3. Propulsive Thrust Generation

Recall from previous sections that the required thrust is a function of speed U_∞ , angle of attack α , and other flight parameters. For steady flight we found

$$\text{Required Thrust: } T^* = C_{D,0}q_\infty S + \frac{W^2}{q_\infty S \pi e A R} . \quad (2.46)$$

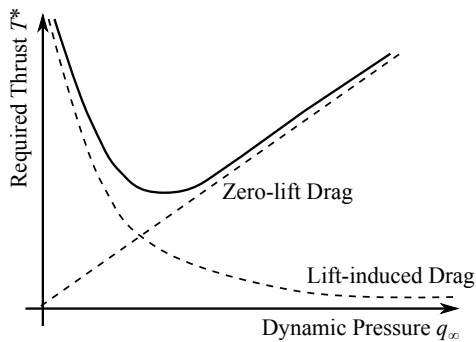


Figure 2.8: Required thrust vs. dynamic pressure.

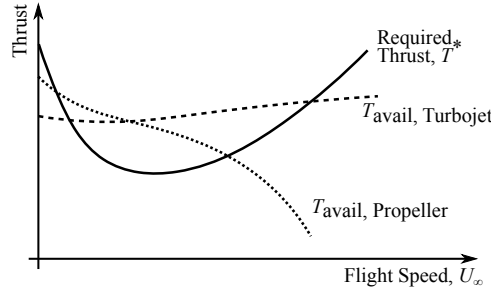


Figure 2.9: Comparison of required and available thrust for different propulsion systems.

The required thrust must be matched or exceeded by the available thrust to meet the performance requirement. The objective now is to link the required thrust to the engine thrust. For this we consider two propulsion systems, namely gas-turbine engine and propeller-driven engine (with relevance to turbofan engine).

2.3.1. Thrust Equation. A general equation for the thrust of airbreathing propulsion (and with some minor modifications also for rocket engines) can be derived from the conservation equations for mass and momentum. For this analysis we consider a control-volume in the coordinate system that is fixed to the engine (see Fig. 2.10).

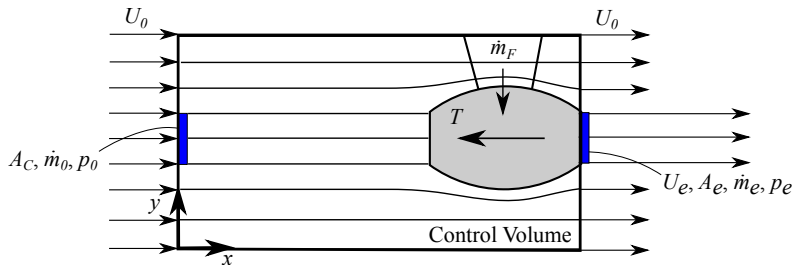


Figure 2.10: Control volume analysis for thrust equation.

Recall conservation equations

$$\text{Mass: } \underbrace{\partial_t \rho}_{\text{Rate of change}} + \underbrace{\nabla \cdot (\rho \mathbf{u})}_{\text{Flux of mass}} = 0 \quad (2.47a)$$

$$\begin{aligned} \text{Momentum: } & \underbrace{\partial_t (\rho \mathbf{u})}_{\text{Rate of change}} + \underbrace{\nabla \cdot (\rho \mathbf{u} \otimes \mathbf{u})}_{\text{Flux of momentum}} = -\underbrace{\nabla p}_{\text{Pressure force}} \\ & + \underbrace{\nabla \cdot \underline{\sigma}}_{\text{Viscous force}} + \underbrace{\mathbf{g}}_{\text{Gravity}} + \underbrace{\mathbf{f}}_{\text{Reaction force}} \end{aligned} \quad (2.47b)$$

and integrate over control-volume with ds defined to be the outward-pointing surface element

$$ds = |ds|\hat{n} = ds \hat{n}, \quad (2.48)$$

we will have the following form (by using the Gauss theorem):

$$\partial_t \int \rho dV + \oint (\rho \mathbf{u}) \cdot \hat{\mathbf{n}} ds = 0, \quad (2.49a)$$

$$\begin{aligned} \partial_t \int (\rho \mathbf{u}) dV + \oint (\rho \mathbf{u})(\mathbf{u} \cdot \hat{\mathbf{n}}) ds &= - \oint p \hat{\mathbf{n}} ds \\ &\quad + \oint \underline{\sigma} \cdot \hat{\mathbf{n}} ds + \int \mathbf{g} dV + \mathbf{F}, \end{aligned} \quad (2.49b)$$

where $\mathbf{F} = \int \mathbf{f} dV$ is the reaction force. By introducing the following assumptions:

- Steady state;
- Negligible viscous effects;
- Negligible gravitational forces (might become relevant for rocket-engines);
- Constant flow rates/properties across area cross-sections;
- Assume that thrust is aligned with x -direction,

we can obtain the steady-state conservation equations for mass and momentum:

$$\oint (\rho \mathbf{u}) \cdot \hat{\mathbf{n}} ds = 0, \quad (2.50a)$$

$$\oint (\rho u_x) \mathbf{u} \cdot \hat{\mathbf{n}} ds + \oint p dS_x = F_x = T_U, \quad (2.50b)$$

where T_U is named the uninstalled thrust. By assuming that all flow-field quantities are piece-wise constant at each area-section, we can reduce the integral equations to algebraic equations:

$$\text{Mass: } -\rho_0 U_0 A_C + \rho_e U_e A_e - \dot{m}_F = 0 \quad (2.51a)$$

$$x\text{-Momentum: } -\rho_0 U_0^2 A_C - p_0 A_e + \rho_e U_e^2 A_e + p_e A_e = F_x \quad (2.51b)$$

and with

$$\dot{m}_e = \rho_e U_e A_e, \quad (2.52)$$

$$\dot{m}_A = \rho_0 U_0 A_C, \quad (2.53)$$

where \dot{m}_A is the air mass flow, we have

$$\dot{m}_e = \dot{m}_A + \dot{m}_F = \dot{m}_A \left(1 + \frac{\dot{m}_F}{\dot{m}_A} \right), \quad (2.54a)$$

$$F_x = \dot{m}_e U_e + \dot{m}_A U_0 + A_e (p_e - p_0), \quad (2.54b)$$

and hence we obtain the thrust equation

$$F_x = T_U = \underbrace{\dot{m}_A \left[\left(1 + \frac{\dot{m}_F}{\dot{m}_A} \right) U_e - U_0 \right]}_{\text{Jet thrust}} + \underbrace{A_e (p_e - p_0)}_{\text{Pressure thrust}}. \quad (2.55)$$

We have several remarks:

- Pressure thrust is typically small (zero) for subsonic aircraft and perfect expansion nozzle ($p_e = p_0$), and requires consideration for rockets and imperfectly expanded nozzles.
- By applying the thrust equation to propeller-flows with $\dot{m}_F = 0$ and $p_e = p_0$, we have:

$$T_{\text{Prop}} = \dot{m}_A(U_e - U_0); \quad (2.56)$$

- Applied to rockets ($\dot{m}_A = 0$) we have

$$T_{\text{Rocket}} = \dot{m}_p U_e + A_e (p_e - p_0), \quad (2.57)$$

where \dot{m}_p is the mass flow rate of propellant.

- Often thrust equation derived above is referred to as *uninstalled thrust*, since it neglects the effects due to inlet drag and nozzle drag:

$$T_I = T_U - D_{\text{Inlet}} - D_{\text{Nozzle}}, \quad (2.58)$$

where T_I is the installed thrust, and the inlet and nozzle drag coefficients are defined as

$$\phi_{\text{Inlet}} = \frac{D_{\text{Inlet}}}{T_u} \sim 0.02 - 0.5, \quad (2.59)$$

$$\phi_{\text{Nozzle}} = \frac{D_{\text{Nozzle}}}{T_u} \sim 0.01, \quad (2.60)$$

and we can write

$$T_I = T_U (1 - \phi_{\text{Inlet}} - \phi_{\text{Nozzle}}). \quad (2.61)$$

- Often thrust is given in English units,

$$T = T g_c \quad \text{and} \quad g_c = \begin{cases} 1, & \text{SI metric} \\ 32.17, & \frac{\text{lbf}\cdot\text{ft}}{\text{lbf}\cdot\text{s}^2} \end{cases}, \quad (2.62)$$

where lbm is pound mass and lbf is pound force. For g_c , since $1 \text{ N} = 0.22482 \text{ lbf}$, $1 \text{ m} = 3.2808 \text{ ft}$ and $1 \text{ kg} = 2.2046 \text{ lbm}$, we have

$$g_c = \frac{\text{kg} \cdot \text{m}}{\text{s}^2 \cdot \text{N}} = 1 = \frac{(2.2046 \text{ lbm})(3.2808 \text{ ft})}{\text{s}^2(0.22482 \text{ lbf})} = 32.17 \frac{\text{lbm} \cdot \text{ft}}{\text{lbf} \cdot \text{s}^2}. \quad (2.63)$$

2.3.2. Thrust Equation for Turbofan Engines. Classic thrust equation that we derived above only considers a single stream through the engine. However, for turbofan engines, the air stream is split into two separated streams –one going through the core and the other one passing by (“bypass”) and generating thrust by airflow acceleration.

Fig. 2.11 shows the control volume and definitions of the stations in a turbofan engine. Abbreviations are LPC for low-pressure compressor, HPC for high-pressure compressor, LPT for low-pressure turbine, and HPT for high-pressure turbine. Note that stations 6 and 7 are omitted and correspond to the combustor inlet/exit of the afterburner.

The bypass ratio is defined as

$$\beta = \frac{\dot{m}_{A,B}}{\dot{m}_{A,C}}, \quad (2.64)$$

where $\dot{m}_{A,B}$ is the airflow through bypass and $\dot{m}_{A,C}$ is the airflow through core.

Assume that both streams expand to $p_e = p_0$ separately and there is no mixing among streams. Thrust equation for turbofan engine in general form is

$$T = \dot{m}_{A,C} [(1 + f)U_e + \beta U_{1e} - (1 + \beta)U_0] + A_e(p_e - p_0) + A_{1e}(p_{1e} - p_0), \quad (2.65)$$

where $f = \dot{m}_F/\dot{m}_A$, U_e is the core exit velocity, and U_{1e} is the fan exit velocity.

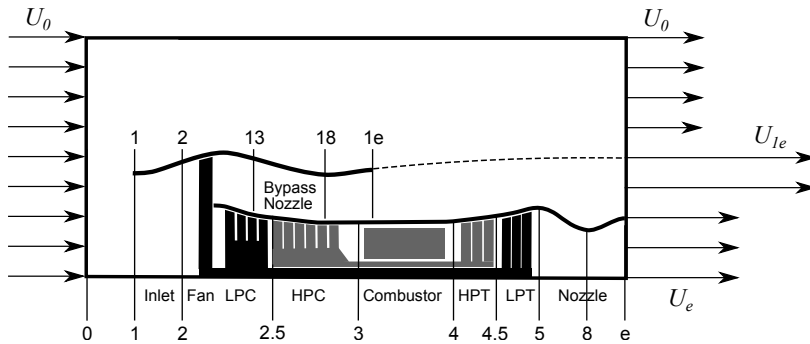


Figure 2.11: Control volume analysis for turbofan thrust equation and station numbering for a commercial twin-spool turbofan engine.

2.4. Fuel Consumption and Range Equation

The weight of the aircraft decreases during the flight as a result of the fuel consumption. The aircraft mass can be expressed as

$$m = \underbrace{m_{AF}}_{\text{Airframe mass}} + \underbrace{m_F}_{\text{Fuel mass}}, \quad (2.66)$$

where m_{AF} is fixed and

$$m_F = m_{F,0} - \int_0^t \dot{m}_F dt \quad (2.67)$$

in which \dot{m}_F is the fuel consumption rate and $m_{F,0}$ is the initial fuel mass. The rate of change of the weight of the aircraft, $W = mg$, is

$$\frac{dW}{dt} = \frac{d}{dt}(mg) = -\dot{m}_F g. \quad (2.68)$$

With the *thrust specific fuel consumption* defined as

$$\text{TSFC} = \frac{\dot{m}_F}{T} \quad (2.69)$$

where T is the thrust, we have

$$\frac{dW}{dt} = -\text{TFSC } T g . \quad (2.70)$$

For level flight, we have $T = W(C_D/C_L)$ and thus

$$\frac{dW}{W} = -\text{TSFC} \frac{C_D}{C_L} g dt . \quad (2.71)$$

With the *endurance factor* EF defined as

$$\text{EF} = \frac{C_L}{C_D} \frac{1}{\text{TSFC} g} , \quad (2.72)$$

we have

$$\frac{dW}{W} = -\frac{dt}{\text{EF}} . \quad (2.73)$$

Assume C_D/C_L is constant, we can integrate to have the weight as a function of flight time,

$$\frac{W(t)}{W_0} = \exp\left(-\frac{t}{\text{EF}}\right) = \exp\left(-\frac{C_D}{C_L} \text{TSFC} g t\right) . \quad (2.74)$$

By using $ds = U dt$ and the *range factor* RF defined as

$$\text{RF} = \frac{C_L}{C_D} \frac{U}{\text{TSFC} g} , \quad (2.75)$$

we have

$$\frac{W(s)}{W_0} = \exp\left(-\frac{s}{\text{RF}}\right) = \exp\left(-\frac{C_D}{C_L} \frac{\text{TSFC}}{U} g s\right) . \quad (2.76)$$

Equation (2.76) is referred to as the Breguet range equation. **Fig. 2.12** shows the plots of EF and RF as a function of flight Mach number and the flying altitude.

The TSFC is a function of engine, altitude and the flight Mach number. Some useful estimates for TSFC_I (the subscript I means for T_I) are

- High bypass-ratio turbofan engine:

$$\text{TSFC}_I = (0.4 + 0.45M) \sqrt{\frac{T}{T_{\text{ref}}}} ; \quad (2.77)$$

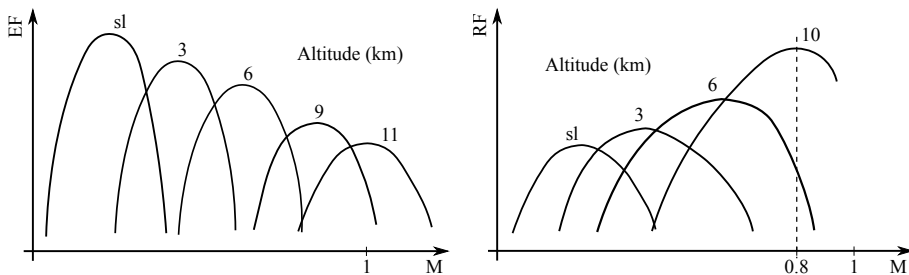


Figure 2.12: Endurance factor and range factor.

- LBR turbofan engine (military):

$$\text{TSFC}_I = (1.0 + 0.35M) \sqrt{\frac{T}{T_{\text{ref}}}} ; \quad (2.78)$$

- Turbojet (military):

$$\text{TSFC}_I = (1.3 + 0.26M) \sqrt{\frac{T}{T_{\text{ref}}}} . \quad (2.79)$$

2.5. Performance Parameters

2.5.1. Thermal Efficiency. The thermal efficiency is defined to be the net rate of power output (kinetic energy) over the available thermal energy:

$$\eta_{\text{th}} = \frac{\dot{P}_{\text{out}}}{\dot{Q}_{\text{in}}} = \frac{\text{Net power of engine}}{\text{Heat addition by combustion}} , \quad (2.80)$$

and

$$\dot{P}_{\text{out}} = \frac{1}{2} \dot{m}_F \left[\left(1 + \frac{\dot{m}_A}{\dot{m}_F} \right) U_e^2 - U_0^2 \right] , \quad (2.81)$$

which is the net rate of change of kinetic energy through the engine. The heat addition is defined as:

$$\dot{Q}_{\text{in}} = \dot{m}_F \text{LHV} , \quad (2.82)$$

where LHV is the lower heating value of fuel (which considers that the water that is formed in the combustion products remains in the vapor state). With this, the thermal efficiency can be written as:

$$\eta_{\text{th}} = \frac{1}{2 \text{LHV}} \frac{\dot{m}_A}{\dot{m}_F} \left[\left(1 + \frac{\dot{m}_A}{\dot{m}_F} \right) U_e^2 - U_0^2 \right] . \quad (2.83)$$

Fig. 2.13 shows the thermal efficiency as a function of year.

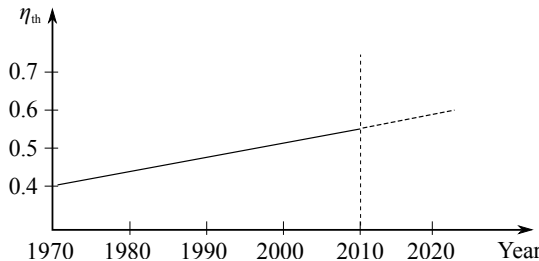


Figure 2.13: Evolution of thermal efficiency over time.

2.5.2. Propulsive Efficiency. The propulsive efficiency is a measure for how efficiently the engine power is used to power the aircraft:

$$\eta_p = \frac{\text{Propulsive power of aircraft}}{\text{Net power of engine}} = \frac{\dot{P}_p}{\dot{P}_{\text{out}}} , \quad (2.84)$$

where $P_p = T_I U_0$ (with T_I being the installed thrust) is the propulsive power. With this, the propulsive efficiency can be written as:

$$\begin{aligned} \eta_p &= \frac{T_I U_0}{\frac{1}{2} \dot{m}_A \left[\left(1 + \frac{\dot{m}_A}{\dot{m}_F} \right) U_e^2 - U_0^2 \right]} , \\ &= \frac{(1 - \phi_{\text{inlet}} - \phi_{\text{nozzle}}) U_0 \left\{ \dot{m}_A \left[\left(1 + \frac{\dot{m}_A}{\dot{m}_F} \right) U_e^2 - U_0^2 \right] + A_C(p_e - p_0) \right\}}{\frac{1}{2} \dot{m}_A \left[\left(1 + \frac{\dot{m}_A}{\dot{m}_F} \right) U_e^2 - U_0^2 \right]} . \end{aligned} \quad (2.85)$$

For the case of (i) a perfectly expanded nozzle, (ii) $\dot{m}_F/\dot{m}_A = f \rightarrow 0$, and (iii) $T_I \rightarrow T_U$ with $\phi_{\text{inlet}} = 0$ and $\phi_{\text{nozzle}} = 0$, Eq. (2.84) reduces to:

$$\eta_p = \frac{2U_0}{U_e + U_0} = \frac{2}{1 + \frac{U_e}{U_0}} . \quad (2.86)$$

Fig. 2.14 shows the propulsive as a function of U_e/U_0 . From this figure it can be seen that we require $U_e \rightarrow U_0$ to achieve a maximum propulsive efficiency of unity. However, at this condition, no thrust is generated. Conditions with $U_e/U_0 < 1$ correspond to a wind generator in which we extract work from the air to generate power, and a windmill is a typical example for this.

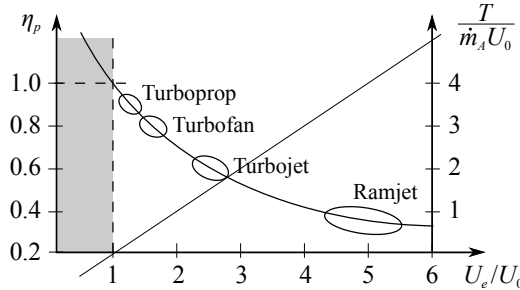


Figure 2.14: Propulsive efficiency.

2.5.3. Overall Efficiency. The overall efficiency is defined as:

$$\begin{aligned} \eta_o &= \frac{\text{Propulsive power}}{\text{Thermal power}} \\ &= \eta_{\text{th}} \eta_p \\ &= \frac{\dot{P}_p}{\dot{Q}_{\text{in}}} = \frac{T_I U_0}{\dot{Q}_{\text{in}}} = \frac{T_I U_0}{\dot{m}_F \text{LHV}} . \end{aligned} \quad (2.87)$$

By introducing the definition for the installed thrust-specific fuel consumption $\text{TSFC}_I = \dot{m}_F/T_I$, this can be write as:

$$\eta_o = \frac{U_0}{\text{TSFC}_I \text{ LHV}}. \quad (2.88)$$

Fig. 2.15 shows the overall efficiency as a function of both η_{th} and η_p .

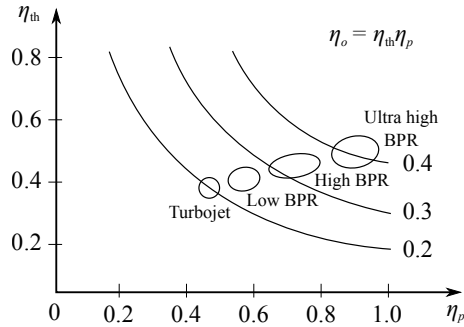


Figure 2.15: Overall efficiency.

2.6. Altitude Effects

The thermodynamic state of the atmosphere changes with altitude, thereby affecting the aircraft performance (thrust and lift, etc).

The temperature in the atmosphere follows a complicated function (see Fig. 2.16), in which different physical processes become important (such as buoyancy and radiation, etc) in controlling the ambient state at different altitude.

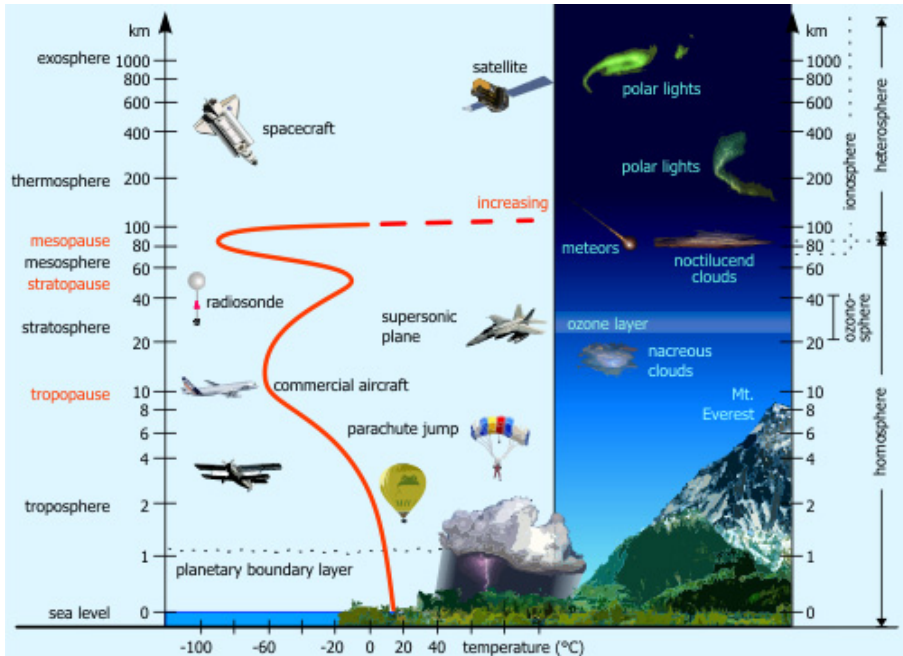


Figure 2.16: Earth atmosphere (source: www.theozonehole.com).

Since the flight altitude of airbreathing vehicles is limited by constraints on the required lift (density), available oxygen concentration, and environmental impact and emissions, we restrict our analysis to the troposphere ($h \leq 12$ km). To good accuracy, this layer can be characterized by an isotropic process, and from a force balance between buoyancy and pressure forces acting on a differential control volume, we can derive the following altitude-dependent state relation for temperature $T(z)$, density $\rho(z)$, and pressure $p(z)$:

$$\frac{T(z)}{T_s} = \left[1 - \frac{\gamma - 1}{\gamma} \left(\frac{z}{\bar{z}} \right) \right] \quad (2.89a)$$

$$\frac{\rho(z)}{\rho_s} = \left[1 - \frac{\gamma - 1}{\gamma} \left(\frac{z}{\bar{z}} \right) \right]^{\frac{1}{\gamma-1}} \quad (2.89b)$$

$$\frac{p(z)}{p_s} = \left[1 - \frac{\gamma - 1}{\gamma} \left(\frac{z}{\bar{z}} \right) \right]^{\frac{\gamma}{\gamma-1}} \quad (2.89c)$$

where

$$\tilde{z} = \frac{p_s}{\rho_s g}, \quad (2.90)$$

and $p_s = 101,325$ Pa, $\rho_s = 1.23$ kg/m³, and $T_s = 288$ K.

A comparison of the isentropic model with the International Standard Atmosphere (ISA) is shown in Fig. 2.17. The ISA model is created by presuming a temperature profile (piece-wise linear for the altitudes shown), and computing the pressure and density from the hydrostatic pressure distribution and ideal gas law. That is,

$$\begin{aligned} \frac{dp}{dz} &= -\rho g, \\ \rho &= \frac{p}{RT(z)}. \end{aligned} \quad (2.91)$$

Combining and integrating, one obtains

$$\frac{p(\hat{z})}{p_s} = \exp \left(- \int_0^{\hat{z}} \frac{T_s}{T(\hat{z}')} d\hat{z}' \right), \quad (2.92)$$

where $\hat{z} = z/\tilde{z}$ is used for brevity.

As shown in the figure, the two models follow rather closely for the density and pressure but not the temperature. MATLAB contains the function "atmosisa", which gives the ISA model's thermodynamic conditions as a function of altitude. It is recommended that this function be used in the homework .

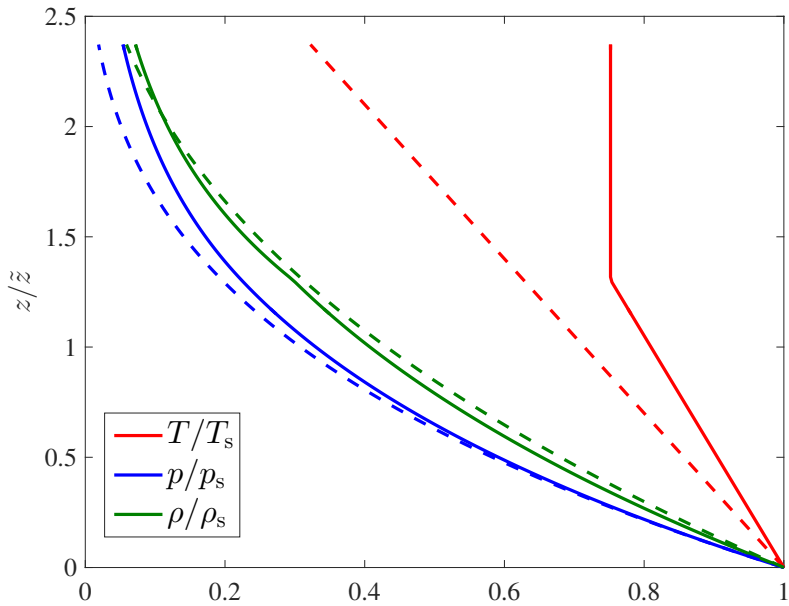


Figure 2.17: The ISA model (—) compared against the isentropic model (---).

Thermodynamics

In the previous sections, we already used basic concepts of gas dynamics to derive the thrust equation. Here, we review all essential gas-dynamic and thermodynamic concepts that we need for the gas turbine cycle analysis.

3.1. Conservation Equations

Recall the general form of a conservation equation of any quantity

$$\phi = \{\text{mass, momentum, energy}\}$$

is

$$\text{accumulation}(\phi) + \text{outflow}(\phi) - \text{inflow}(\phi) = \text{production}(\phi). \quad (3.1)$$

For the following analysis, we will consider a control volume analysis, which is illustrated in Fig. 3.1.

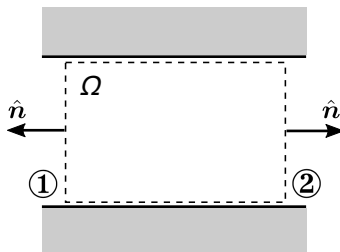


Figure 3.1: Control volume.

3.1.1. Mass Conservation. The governing equation describing conservation of mass can be written in the following form:

$$\frac{dm}{dt} = \dot{m}_{\text{in}} - \dot{m}_{\text{out}} = - \oint \rho \mathbf{u} \cdot \hat{\mathbf{n}} dA, \quad (3.2)$$

where $\dot{m} = \int \rho u_{\perp} dA$, in which u_{\perp} is the velocity component normal to the area A . For stationary flows, $dm/dt = 0$, and hence we have $\dot{m}_{\text{in}} = \dot{m}_{\text{out}}$, or

$$\rho_1 u_{\perp 1} A_1 = \rho_2 u_{\perp 2} A_2, \quad (3.3)$$

which is called the one-dimensional mass-flow equation.

3.1.2. Momentum Conservation. The governing equation describing conservation of momentum conservation takes the following form:

$$\begin{aligned} \frac{d(\rho\mathbf{u})}{dt} &= \frac{d}{dt} \int \rho u dV = \dot{M}_{\text{in}} - \dot{M}_{\text{out}} + \sum_i \mathbf{F}_i \\ &= - \oint (\rho\mathbf{u})(\mathbf{u} \cdot \hat{\mathbf{n}}) dA + \sum_i \mathbf{F}_i, \end{aligned} \quad (3.4)$$

which is a vector equation for each velocity component $\mathbf{u} = (u_1, u_2, \dots)^T \in \mathbb{R}^{N_d}$ (with N_d being the spatial dimension). The force terms on the right-hand side are:

- Pressure force: $\mathbf{F}_p = - \int \nabla p dV$;
- Viscous force: $\mathbf{F}_v = - \oint \hat{\mathbf{n}} \cdot \underline{\underline{\sigma}} dA$;
- Gravitational force: $\mathbf{F}_g = \int \rho g dV$.

Under the assumption of steady-state, the momentum conservation equation reduces to:

$$\dot{M}_{\text{in}} - \dot{M}_{\text{out}} = - \sum_i \mathbf{F}_i, \quad (3.5)$$

or for one-dimensional flows:

$$(\rho_2 u_{\perp 2} A_2) u_{\perp 2} - (\rho_1 u_{\perp 1} A_1) u_{\perp 1} = p_1 A_1 - p_2 A_2 - F_D, \quad (3.6)$$

where F_D is the drag force, as shown in Fig. 3.2.

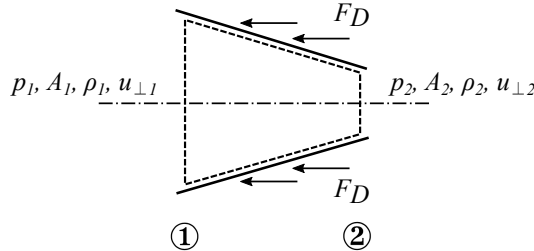


Figure 3.2: Momentum balance on control volume.

3.1.3. Energy Conservation. We define the total energy as $H_T = H + \frac{1}{2}m\mathbf{u}^2 + mgz$ or in mass-specific form

$$h_T = h + \frac{1}{2}u^2 + gz = h_0 + gz. \quad (3.7)$$

The conservation equation is

$$\frac{d}{dt} \int \rho h_T dV + \oint \rho h_T (\mathbf{u} \cdot \hat{\mathbf{n}}) dA = \underbrace{\int \dot{Q} dV}_{\text{Heat transfer rate}} + \underbrace{\frac{d}{dt} \int pdV}_{\text{Technical work}} + \underbrace{\int F_\sigma dV}_{\text{Viscous force}}, \quad (3.8)$$

where \dot{q} is the heat transfer rate (per unit time and unit volume). Using Fourier's law, \dot{q} can be written as $\dot{q} = \nabla \cdot (\lambda \nabla T)$, and $F_\sigma = \nabla \cdot (\underline{\underline{\sigma}} \cdot \mathbf{u})$ is the viscous dissipation.

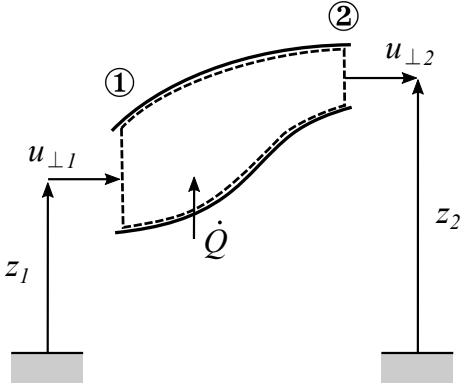


Figure 3.3: Control volume balance for energy equation.

3.1.4. Summary of Governing Equations. In the following, we summarize the set of working equations in differential form that we will use for the subsequent analysis:

- Mass conservation:

$$\partial_t \rho + \nabla \cdot (\rho \mathbf{u}) = 0; \quad (3.9)$$

- Momentum conservation:

$$\partial_t (\rho \mathbf{u}) + \nabla \cdot (\rho \mathbf{u} \otimes \mathbf{u}) = -\nabla p + \nabla \cdot \underline{\underline{\sigma}}; \quad (3.10)$$

- Energy conservation:

$$\partial_t (\rho h_T) + \nabla \cdot (\rho \mathbf{u} h_T) = \partial_t p + \nabla \cdot \dot{\mathbf{q}} + \nabla \cdot (\underline{\underline{\sigma}} \cdot \mathbf{u}), \quad (3.11)$$

where

$$\underline{\underline{\sigma}} = \mu(\nabla \mathbf{u} + (\nabla \mathbf{u})^T) - \frac{2}{3}\mu(\nabla \cdot \mathbf{u})I. \quad (3.12)$$

3.2. Thermodynamics of Gases

3.2.1. First Law of Thermodynamics. For a closed system (control volume), the first law of thermodynamics takes the following form:

$$de = \delta q - \delta w_m, \quad (3.13)$$

where the mechanical work (moving-boundary work) is written as $\delta w_m = pdv$. The corresponding energy equation for an open thermodynamic system is;

$$dh = \delta q - \delta w_t, \quad (3.14)$$

where the technical work (compressor/turbine work) is $\delta w_t = -vdp = \frac{1}{\rho}dp$.

3.2.2. Second Law of Thermodynamics. The second law of thermodynamics provides a relation about the directionality of a thermodynamic process, by introducing entropy as a measure for the reversibility of a thermodynamic process. In general, entropy is a measure for information content, and, in the context of thermodynamics, we associate entropy as direct link between micro- and macro-states. This link can be established through statistical thermodynamics.

The change in entropy provides information about a reversible process. Consider states (1) and (2): if $dS = S_2 - S_1 = 0$ then the process is reversible. For a system that is not in equilibrium, $dS \geq 0$. To quantify irreversible contributions, we extend the second law by formally introducing an irreversible contribution ΔS_{irr} . With this, we can write the second law in a general form as:

$$dS = \frac{\delta Q}{T} + \Delta S_{\text{irr}} \geq 0. \quad (3.15)$$

Typical sources of irreversibilities are:

- Shocks
- Combustion
- Friction
- Separation
- Mixing
- Phase transition

For practical applications, irreversibilities reduce the thermodynamic efficiency since heat and work is required to overcome ΔS_{irr} .

3.2.3. Equation of State. From gas dynamic theory, we are able to relate the macroscopic pressure to the mean particle speed \bar{c} (see [17]):

$$p = \frac{1}{3} \rho \bar{c}^2. \quad (3.16)$$

Since \bar{c} is a function of temperature, we can directly relate pressure to temperature and density:

$$p = f(\rho, T), \quad (3.17)$$

providing a formal description for a general state-relation. A specific form of the state-equation (3.17) is the *ideal gas law*:

$$p = \rho R T \quad (3.18)$$

where the gas constant R is introduced as proportionality constant. We can express the ideal gas law in the following different, but equivalent, forms:

- *Mole-specific* quantities:

$$pV = nRT;$$

- *Mass-specific* quantities:

$$pV = mRT \quad \Leftrightarrow \quad p = \rho RT;$$

- *Particle-specific* quantities:

$$pV = Nk_B T$$

with $k_B = \mathcal{R}/N_A$ and $N_A n = N$.

The ideal gas law (IGL) is only one but rather powerful example of a state-equation. In general, we define a *state equation* as a constitutive relation between two or more thermodynamic variables.

The IGL is very accurate as long as the intermolecular spacing between particles is sufficiently large (“Knudsen limit”). However, when the pressure p gets large enough and/or the temperature is low (cryogenic) the intermolecular forces become increasingly important, and the IGL becomes invalid. Such high-pressure conditions require the consideration of so-called real-fluid effects, and can be accommodated by extending the state relation in the following form:

$$p = Z\rho RT \quad (3.19)$$

where Z is the compressibility factor, with

$$Z = \begin{cases} = 1: & \text{for ideal gas} \\ \neq 1: & \text{real fluid and extension to super/sub-critical fluid mixtures} \end{cases} \quad (3.20)$$

Real fluid effects are often described by *cubic state equations*. The general form of a cubic state relation can be written in the form:

$$p = \frac{\mathcal{R}T}{V_m - b} - \frac{\Theta(V_m - \eta)}{(V_m - b)(V_m^2 + \delta V + \varepsilon)} \quad (3.21)$$

where $V_m = M/\rho = V/n$ is the molar volume, and the parameters $\Theta, b, \eta, \varepsilon, \delta$ depend on temperature, mixture and critical conditions. Examples of commonly employed cubic state relations are equations due to

- Peng-Robinson (PR);
- Redlich-Kwong (RK);
- Soave-Redlich-Kwong (SRK).

The consideration of real fluid effects is relevant if either pressure or temperature of the gas exceeds the critical point (see Fig. 3.4). Relevant applications are rocket-engines and combustion in high-pressure aviation gas-turbines in which the combustion chamber pressure exceeds the critical pressure. Values for critical pressure and temperature conditions that are relevant for our lecture are summarized in Table 1.

	T_c [K]	p_c [bar]
H ₂	33.2	13.0
O ₂	154.6	50.5
N ₂	126.3	33.9
CH ₄	190.9	46.4

Table 1: Critical conditions for selected gases.

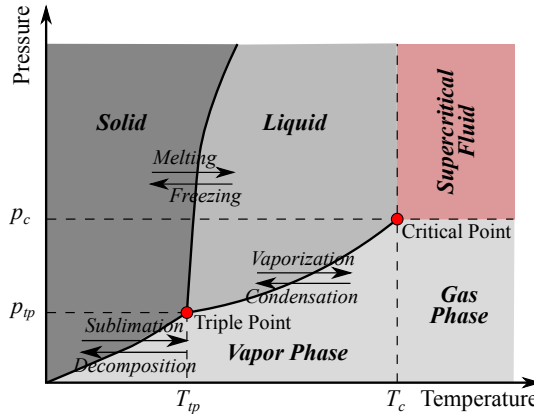


Figure 3.4: Phase diagram.

3.2.4. Constitutive Relations. For a thermally perfect gas, the sensible internal energy and enthalpy are only dependent on temperature:

$$e = e(T) \quad \text{and} \quad h = h(T) . \quad (3.22)$$

The *specific heat capacities* are defined as

$$c_p = \left. \frac{dh}{dT} \right|_p \quad \text{and} \quad c_v = \left. \frac{de}{dT} \right|_v . \quad (3.23)$$

The *ratio of specific heat capacities* is then defined as

$$\gamma = \frac{c_p}{c_v} \quad \text{and} \quad R = c_p - c_v . \quad (3.24)$$

Remarks:

- For our thermodynamic analysis, we frequently make use of the calorically perfect gas assumption, stating that c_p and c_v are constant and independent of temperature. This reduces the mathematical complexity, since it allows to directly evaluate enthalpy and internal energy in terms of algebraic relations of temperature.
- In general, the specific heat capacities of a gas mixture are dependent on species composition and temperature

$$c_p = c_p(\mathbf{Y}, T) \quad \text{with} \quad c_p = \sum_{i=1}^{N_s} Y_i c_{p,i} . \quad (3.25)$$

- For practical applications, the species-specific heat capacities at constant pressure are commonly tabulated in terms of higher-order polynomial expressions:

$$\frac{c_p}{R} = \sum_{i=-2}^4 a_i T^i .$$

Coefficients of these polynomials are tabulated in the form of NASA polynomial tables [18].

3.2.5. Isentropic Relation. The entropy relation takes the following form

$$ds = \frac{dh}{T} - \frac{dp}{\rho T} \quad (3.26)$$

for a reversible process and with $dh = c_p dT$, $c_p = \frac{\gamma}{\gamma-1} R$, and $\rho T = p/R$, we have two other forms of the entropy relation:

$$ds = \frac{\gamma}{\gamma-1} R \frac{dT}{T} - R \frac{dp}{p}, \quad (3.27)$$

and

$$ds = \frac{1}{\gamma-1} R \frac{dT}{T} - R \frac{d\rho}{\rho}. \quad (3.28)$$

These equations are commonly referred to as Gibbs' equations or as Gibbs-Duhem equation for multicomponent mixtures.

The speed of sound is defined by:

$$a^2 \equiv \left(\frac{\partial p}{\partial \rho} \right)_s, \quad (3.29)$$

where the subscript 's' indicates that the partial derivative is evaluated at constant entropy. It is useful to write Eq. (3.29) as the sum of constant energy and constant density processes, giving:

$$a^2 = \left(\frac{\partial p}{\partial \rho} \right)_e + \frac{p}{\rho^2} \left(\frac{\partial \rho}{\partial e} \right). \quad (3.30)$$

By introducing the calorically-perfect gas approximation, and rewriting the internal energy as:

$$e = c_v T = \frac{1}{\gamma-1} RT = \frac{1}{(\gamma-1)} \frac{p}{\rho} \quad \Rightarrow \quad p = (\gamma-1) \rho e \quad (3.31)$$

(setting the reference condition to zero). We can write the following useful expressions for the speed of sound:

$$\begin{aligned} a^2 &= (\gamma-1)e + \frac{p}{\rho^2}(\gamma-1)\rho \\ &= (\gamma-1) \left(e + \frac{p}{\rho} \right) \\ &= (\gamma-1)h \\ &= (\gamma-1)c_p T \\ &= \gamma RT \\ &= \frac{\gamma p}{\rho}. \end{aligned} \quad (3.32)$$

3.2.6. Stagnation Conditions. For gas turbine analysis, it is convenient to perform the analysis in terms of stagnation conditions. For this, we define the total enthalpy (or stagnation enthalpy) as:

$$h_0 = h + \frac{1}{2}u^2. \quad (3.33)$$

combining sensible enthalpy and mass-specific kinetic energy. For a calorically perfect gas, we write:

$$h = c_p(T - T_{\text{ref}}), \quad (3.34)$$

so that Eq. (3.33) can be written as:

$$T_0 = T + \frac{u^2}{2c_p}, \quad (3.35)$$

with $c_p = \frac{\gamma}{\gamma-1}R$, $\gamma RT = a^2$ and the Mach number as $M = u/a$, it follows:

$$\frac{T_0}{T} = 1 + \left(\frac{\gamma-1}{2}\right) M^2. \quad (3.36)$$

With isentropic state relations:

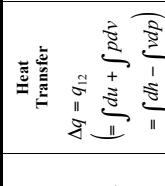
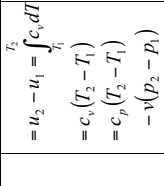
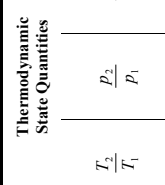
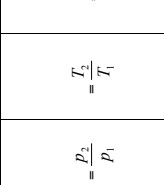
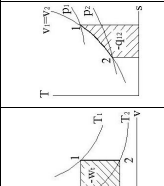
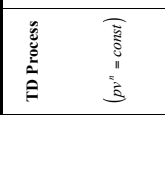
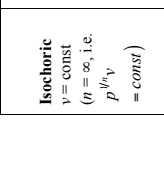
$$\frac{p_0}{p} = \left(\frac{T_0}{T}\right)^{\frac{\gamma}{\gamma-1}} \quad \text{and} \quad \frac{\rho_0}{\rho} = \left(\frac{p_0}{p}\right)^{\frac{1}{\gamma}}, \quad (3.37)$$

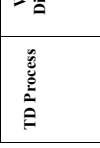
we obtain relation for stagnation pressure and stagnation temperature:

$$\frac{p_0}{p} = \left[1 + \left(\frac{\gamma-1}{2}\right) M^2\right]^{\frac{\gamma}{\gamma-1}}, \quad (3.38)$$

$$\frac{\rho_0}{\rho} = \left[1 + \left(\frac{\gamma-1}{2}\right) M^2\right]^{\frac{1}{\gamma-1}}. \quad (3.39)$$

Thermodynamic Processes
(All Equations are Mass-Specific, Simplifications for Perfect Gas, Reversible Process)

ID Process	Work-Diagram	Heat-Diagram	Thermodynamic State Quantities	Heat Transfer	Mechanical Work (Expansion Work (Closed System))	Technical Work (Open System)	Change in Entropy
$(\rho v^n = \text{const})$	pV -diagram	T_s -diagram	$\frac{T_2}{T_1}$ $\frac{p_2}{p_1}$ $\frac{v_2}{v_1}$	$\Delta Q = q_{12}$ $= \int du + \int pdv - \int vdP$	$W_{m12} = \int_{T_1}^{T_2} p dV$	$\Delta s_{12} = s_2 - s_1$ $= \int_T^2 \frac{dq}{T}$	$du = c_v dT$
Isochoric $v = \text{const}$ $(n = \infty, \text{i.e. } P^{\frac{1}{n-1}} V = \text{const})$			$= u_2 - u_1 = \int_{T_1}^{T_2} c_v dT$ $= c_v (T_2 - T_1)$ $= c_p (T_2 - T_1)$ $- v(p_2 - p_1)$	$= 0$	$= -v(p_2 - p_1)$	$= c_v \ln \frac{T_2}{T_1}$ $= c_v \ln \frac{P_2}{P_1}$	$du = c_v dT$ $\Delta u = c_v (T_2 - T_1)$
Isobaric $P = \text{const}$ $(n = 0)$			$= \frac{v_2}{v_1}$ $= 1$ $= \frac{T_2}{T_1}$	$= h_2 - h_1$ $= c_p (T_2 - T_1)$ $= c_v (T_2 - T_1)$ $+ p(v_2 - v_1)$	$= p(v_2 - v_1)$ $= R(T_2 - T_1)$	$= 0$ $= -R$	$= c_p \ln \frac{T_2}{T_1}$ $= c_p \ln \frac{V_2}{V_1}$
Isothermal $T = \text{const}$ $(n = 1)$			$= \frac{v_1}{v_2}$ $= 1$ $= \frac{P_1}{P_2}$	$= w_{12}$ $= RT \ln \frac{P_1}{P_2}$ $= RT \ln \frac{V_2}{V_1}$ $(RT = p_1 V_1 = p_2 V_2)$	$= q_{12}$ $= RT \ln \frac{P_1}{P_2}$ $= RT \ln \frac{V_2}{V_1}$ $(RT = p_1 V_1 = p_2 V_2)$	$= -w_{12}$ $= -R \ln \frac{P_2}{P_1}$ $\left(= -R \ln \frac{V_2}{V_1} \right)$	$= R \ln \frac{V_2}{V_1}$ $= R \ln \frac{P_1}{P_2}$ $\Delta u = 0$
Ientropic $s = \text{const}$ $ds = 0$ $(n = \gamma)$			$= \left(\frac{v_1}{v_2}\right)^{\gamma-1}$ $= \left(\frac{p_1}{p_2}\right)^{\frac{1}{\gamma-1}}$	$= \left(\frac{T_1}{T_2}\right)^{\frac{1}{\gamma-1}}$ $= \left(\frac{p_1}{p_2}\right)^{\frac{1}{\gamma-1}}$	$= -(h_2 - h_1)$ $= -v' w_{12}$ $= -v' c_v (T_2 - T_1)$ $= -c_p (T_2 - T_1)$	$= 0$	$du = c_v dT$ $= -w_{12}$ $= c_v (T_2 - T_1)$ $= \frac{R}{\gamma-1} (T_2 - T_1)$

TD Process $(pv^n = \text{const})$	Work-Diagram pV -diagram	Heat-Diagram T_s -diagram	Thermodynamic State Quantities	Heat Transfer $\Delta q = q_{12}$ $(= \int de + \int pdv)$ $= \int dh - \int dp$	Mechanical Work (Closed System) $w_{12} = \int_1^2 pdv$	Mechanical Work (Open System) $w'_{12} = - \int_1^2 pdp$	Change in Entropy $\Delta s_{12} = s_2 - s_1$	Change in Internal Energy $du = c_v dT$
Polytropic $(n = n;$ typically $1 < n < \gamma)$			$\frac{T_2}{T_1}, \frac{p_2}{p_1}, \frac{v_2}{v_1}$	$\Delta q = c_v \frac{n-\gamma}{n-1} (T_2 - T_1) = c_v \frac{n-\gamma}{n-1} (T_2 - T_1)$ Identical to isentropic process, replace γ by n .	$w_{12} = \frac{p_1 v_1}{n-1} \left[\left(\frac{T_2}{T_1} \right)^{\frac{1}{n}} - 1 \right]$	$w'_{12} = \frac{p_1 v_1}{n-1} \left[\left(\frac{p_2}{p_1} \right)^{\frac{1}{n}} - 1 \right]$ $(p_1 v_1 = RT_1)$	$\Delta s_{12} = \frac{c_v}{n-1} \ln \frac{T_2}{T_1} = \frac{c_v}{n-1} \ln \frac{p_2}{p_1}$	$du = c_v \frac{T_2}{T_1} + R \ln \frac{v_2}{v_1}$ $\Delta u = c_v (T_2 - T_1)$
Closed System:					$du = \delta q - \delta w = \delta q - pdv; w_{12} = \int_1^2 pdv$	$w'_{12} = - \int_1^2 pdp$	1st Law of Thermodynamics:	
Open System:					$dh = \delta q - \delta w_i = \delta q + vdP; w'_{12} = - \int_1^2 vdP$			

Aircraft Jet Engines

4.1. General Gas Turbine Engine Concepts

4.1.1. Engine Design. Fig. 4.1 shows functional relations between TSFC and Mach number for different types of jet engines. The objective of the engine design is to maximize the thrust. Since $T \sim \dot{m}_A(U_e - U_0)$, this is similar to maximizing the air flow rate and U_0 . This is best accomplished with continuous flow engines, compared to cyclic engine concepts, such as IC/reciprocating engines.

At low-speed conditions, propellers are best suited to handle the airflows and piston engines are more efficient at low power setting. However, propellers become inefficient $M > 0.5$. Reason for this is that propeller-tip speed becomes supersonic, which results in substantial losses and noise generation.

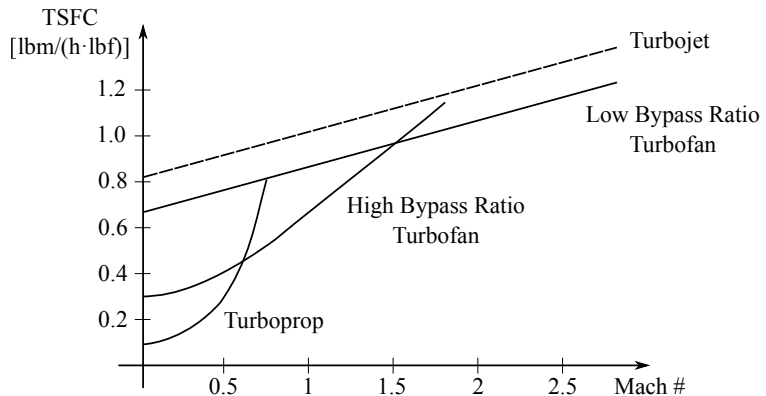


Figure 4.1: Relation between TSFC and Mach number for different jet engines.

4.1.2. Categories of Gas Turbine Engines. In the following discussion, we provide graphic illustrations of relevant gas-turbine engine concepts.

- Basic gas generator (Fig. 4.2)
- Turbojet (Fig. 4.3)
- Turbofan (Fig. 4.4)
- Multi-spool turbofan (Fig. 4.5)
- Open rotor turboprop (Fig. 4.6)

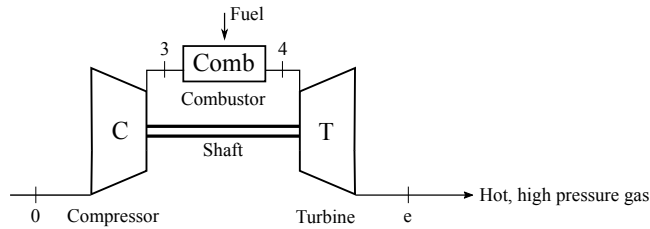


Figure 4.2: Basic gas generator.

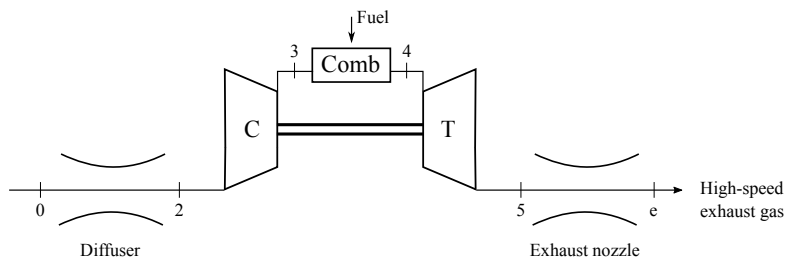


Figure 4.3: Turbojet engine.

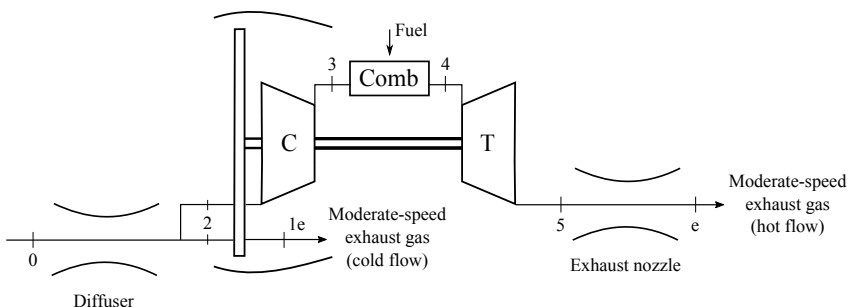


Figure 4.4: Turbofan engine.

- Low bypass-ratio turbofan with afterburner (Fig. 4.7)

4.1.3. Objectives of Engine Analysis. The objectives of engine analysis includes:

- Estimate the best possible engine performance as a function of principle design parameters:
 - Maximum engine temperature
 - Pressure ratio
 - Flight speed

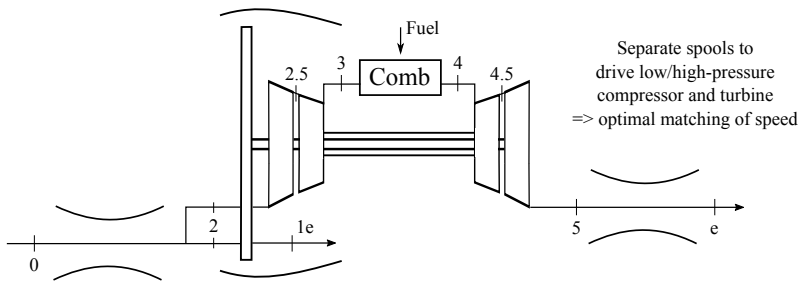


Figure 4.5: Multi-spool turbofan engine.

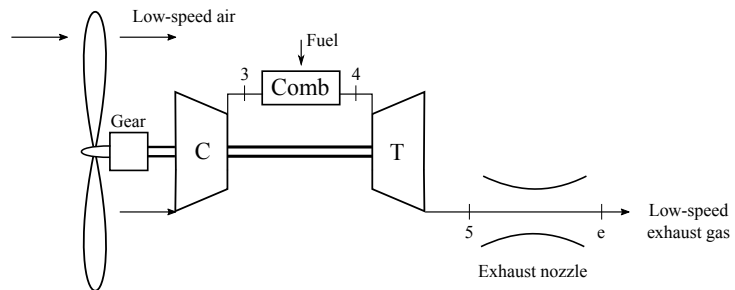


Figure 4.6: Turboprop engine.

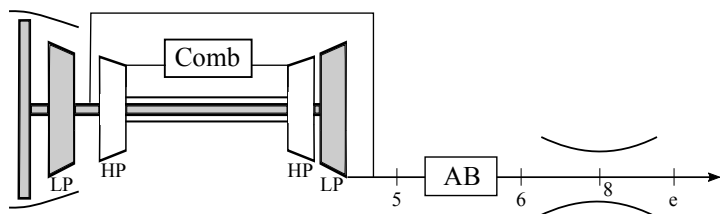


Figure 4.7: Low bypass-ratio turbofan with afterburner (AB).

- Ambient conditions
- Evaluate effects of departure from ideality in engine components:
 - Compressor
 - Turbine
 - Nozzle
- Establish methods to enable the assessment of strategies for future performance increase.

- Design components to match the engine performance (compressor and turbine).
- Evaluate effects of engine performance on aircraft performances.

The input for the engine design analysis includes:

- Flight conditions: M_0, T_0, p_0, c_p
- Design parameters: T_{04} (combustor exit temperature)
- Component performances: $A_C, \eta_C, \eta_{\text{comb}}, \eta_T$

and the output or the design choices are $A_C, U_e, T, \dot{m}_F, f$.

4.2. Analysis of Turbojet Engines

Here we perform a basic analysis of turbojet engines. A schematic of this engine is shown in Fig. 4.8. The flow through this engine is described by the

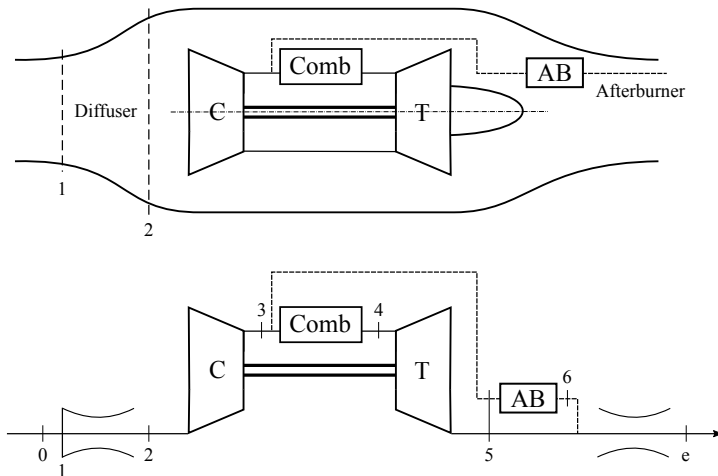


Figure 4.8: Schematic of a turbojet engine.

following processes:

- $0 \rightarrow 1$: Air at freestream/flight condition is brought to intake condition (typically involving acceleration or deceleration of the flow-velocity)
- $1 \rightarrow 2$: Decrease in air velocity as air passes through diffuser
- $2 \rightarrow 3$: Compression of air in compressor
- $3 \rightarrow 4$: “Heating” of air by mixing and burning with fuel
- $4 \rightarrow 5$: Expansion of air through turbine to extract technical work to drive compressor
- $(5 \rightarrow 6)$: Further heating of air by combustion in afterburner
- $5 \rightarrow e$: Acceleration of air through exhaust nozzle

Some remarks on the afterburner:

- The bypass flow is utilized for cooling and for providing excess air for combustion in the afterburner
- The bypass flow is about 30–40% or “low bypass ratio”.

4.2.1. Ideal Brayton Cycle Analysis. To illustrate the analysis of an ideal Brayton cycle, we consider the flight conditions at $z = 7500$ m, $T_0 = 214.5$ K, $p_0 = 36.1$ kPa, $\gamma = 1.4$, and $M = 0.85$. The overall pressure ratio for the compressor $p_{03}/p_{02} = 25$. For the combustor, we consider a heating value of $Q_R = \text{LHV} = 45000$ kJ/kg_{Fuel}, and the combustor exit temperature is $T_{04} = 1500$ K.

The T - s diagram for the Ideal Brayton cycle is shown in Fig. 4.9.

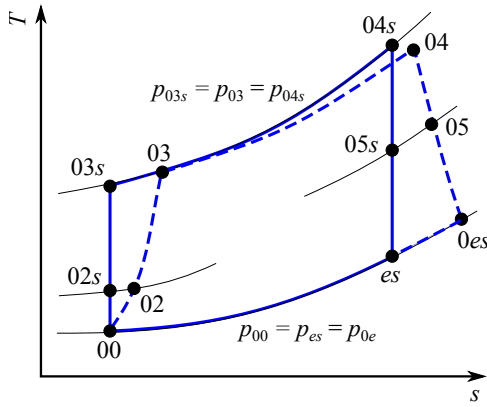


Figure 4.9: T - s diagram of ideal and real Brayton cycle. Solid blue line for ideal Brayton cycle and dashed blue line for real Brayton cycle.

4.2.2. Real Brayton Cycle Analysis. For practical turbojets, we need to consider non-idealities that arise from irreversibility due to:

- Friction
- Mixing
- Pressure drop
- Flow separation

To account for such effects we introduce the *adiabatic efficiency* η :

- Diffuser:

$$\eta_D = \frac{h_{02s} - h_0}{h_{02} - h_0}; \quad (4.1)$$

- Compressor:

$$\eta_C = \frac{h_{03s} - h_{02}}{h_{03} - h_{02}}; \quad (4.2)$$

- Turbine:

$$\eta_T = \frac{h_{04} - h_{05}}{h_{04} - h_{05s}}; \quad (4.3)$$

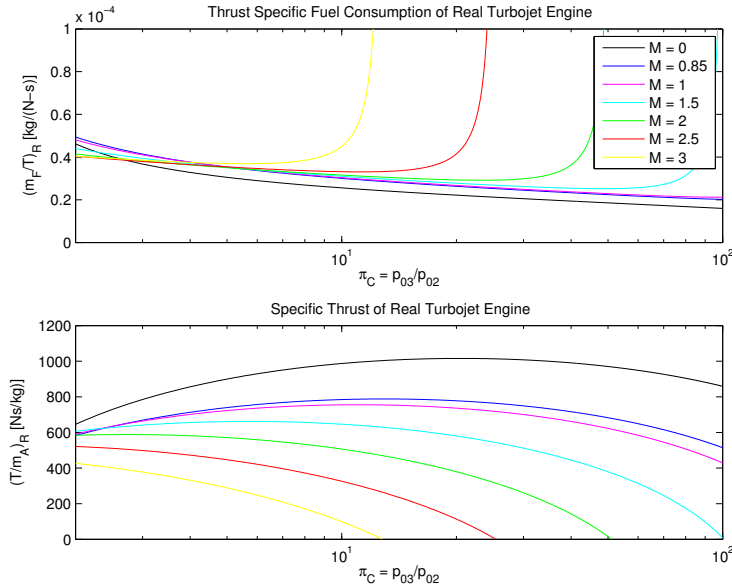


Figure 4.10: Thrust specific fuel consumption and specific thrust as a function of Mach number and π_C .

- Nozzle:

$$\eta_N = \frac{h_{05} - h_{0e}}{h_{05} - h_{es}}. \quad (4.4)$$

Typical values for the adiabatic efficiencies are $\eta_D = 0.7 - 0.9$, $\eta_C = 0.85 - 0.9$, $\eta_{\text{comb}} = 0.9 - 0.95$, $\eta_T = 0.97 - 0.99$, and $\eta_N = 0.95 - 0.98$.

To include these efficiencies in our analysis, we consider the following numerical values:

- Diffuser: $\eta_D = 0.95$
- Compressor: $\eta_C = 0.87$
- Combustor: $\eta_{\text{comb}} = 1.0$
- Turbine: $\eta_T = 0.91$
- Nozzle: $\eta_N = 0.98$

The pressure drop $p_{04}/p_{03} = 0.96 = \pi_{\text{comb}}$. With this, we can perform the engine analysis. For this, we proceed successively through the engine, and consider each component.

- Compressor inlet condition:

$$T_{02} = T_0 \left(1 + \frac{\gamma_D - 1}{2} M_0^2 \right). \quad (4.5)$$

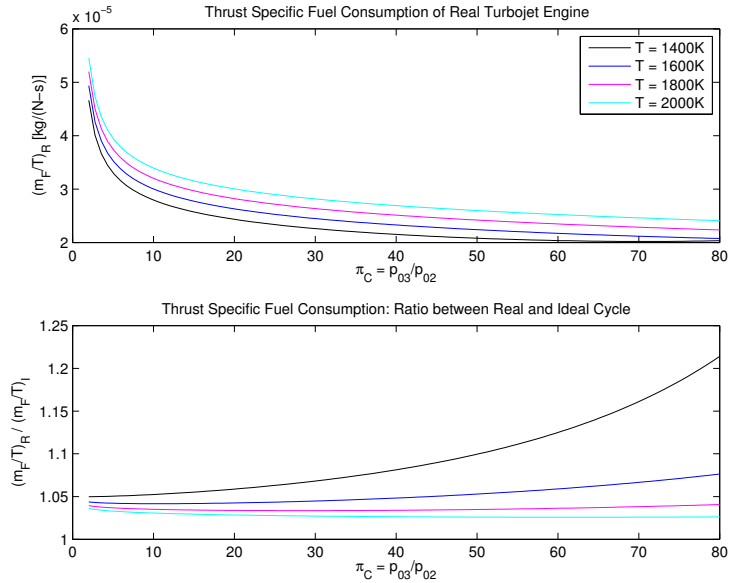


Figure 4.11: Thrust specific fuel consumption as a function of temperature and π_C .

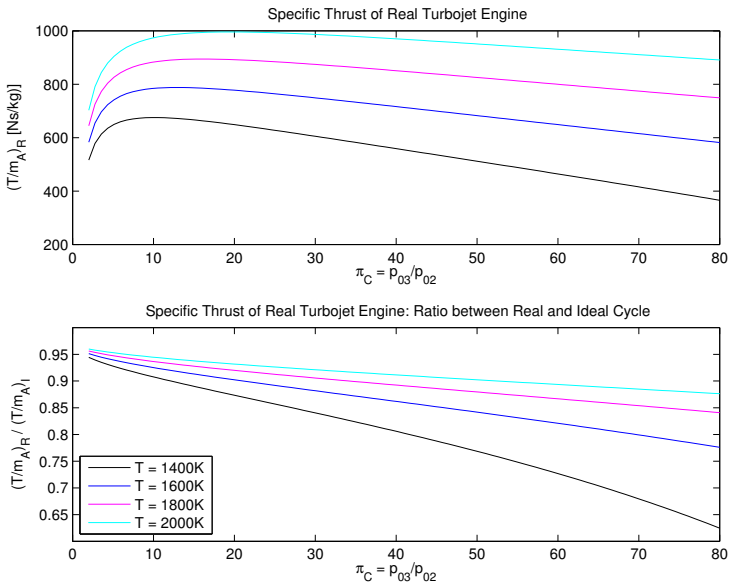


Figure 4.12: Specific thrust as a function of temperature and π_C .

From

$$\eta_D = \frac{h_{02s} - h_0}{h_{02} - h_0} = \frac{T_{02s} - T_0}{T_{02} - T_0}, \quad (4.6)$$

and rearrange to solve for the isentropic stagnation temperature at stage 2

$$\frac{T_{02s}}{T_0} = 1 + \eta_D \left(\frac{T_{02}}{T_0} - 1 \right). \quad (4.7)$$

Since $p_{02} = p_{02s}$,

$$\frac{p_{02s}}{p_0} = \frac{p_{02}}{p_0} = \left(\frac{T_{02s}}{T_0} \right)^{\frac{\gamma_D}{\gamma_D - 1}} = \left[1 + \eta_D \left(\frac{T_{02}}{T_0} - 1 \right) \right]^{\frac{\gamma_D}{\gamma_D - 1}}, \quad (4.8)$$

where γ_D is the specific heat ratio in the diffuser.

- Compressor outlet condition:

$$p_{03} = p_{02}\pi_C. \quad (4.9)$$

From

$$\eta_C = \frac{T_{03s} - T_{02}}{T_{03} - T_{02}} \quad \text{and} \quad \frac{T_{03s}}{T_{02}} = \left(\frac{p_{03}}{p_{02}} \right)^{\frac{\gamma_C - 1}{\gamma_C}}, \quad (4.10)$$

we have

$$\frac{T_{03}}{T_{02}} = 1 + \frac{1}{\eta_C} \left(\pi_C^{\frac{\gamma_C - 1}{\gamma_C}} - 1 \right), \quad (4.11)$$

$$\frac{p_{03}}{p_{02}} = \pi_C \quad (4.12)$$

- Combustor (fuel/air ratio): Typically T_{04} is specified and determined by material properties of the turbine. From the overall conservation: $dh|_3^4 = \Delta \dot{Q}$, we have (here we assume that the fuel has the same temperature as the air at the combustor inlet):

$$(\dot{m}_A + \dot{m}_F)h_{04} - (\dot{m}_A + \dot{m}_F)h_{03} = \dot{m}_F \text{LHV}, \quad (4.13)$$

$$(1 + f)(h_{04} - h_{03}) = f \text{LHV}, \quad (4.14)$$

where $h_{03} = c_p(T_{03} - T_{\text{ref}})$ and $h_{04} = c_p(T_{04} - T_{\text{ref}})$. Solving for the fuel-air ratio f :

$$f = \frac{\frac{T_{04}}{T_{03}} - 1}{\frac{\text{LHV}}{c_p T_{03}} - \left(\frac{T_{04}}{T_{03}} - 1 \right)}, \quad (4.15)$$

$$p_{04} = p_{03}\pi_{\text{comb}}. \quad (4.16)$$

- Turbine exit condition: The work extracted from the turbine is used to drive the compressor. For an adiabatic system: $dh = -\delta w_t$,

$$(\dot{m}_A + \dot{m}_F)c_p(T_{05} - T_{04}) = -\dot{m}_A c_p(T_{03} - T_{02}), \quad (4.17)$$

$$T_{05} = T_{04} - \frac{c_p^C(T_{03} - T_{02})}{(1 + f)c_p^T}, \quad (4.18)$$

$$T_{05} = T_{04} - (T_{03} - T_{02}), \quad (4.19)$$

for $f \sim 0$ and $c_p^T = c_p^C$. With the adiabatic efficiency

$$\eta_T = \frac{h_{04} - h_{05}}{h_{04} - h_{05s}} = \frac{\frac{T_{05}}{T_{04}} - 1}{\frac{T_{05s}}{T_{04}} - 1}, \quad (4.20)$$

we have

$$\frac{T_{05s}}{T_{04}} = 1 + \frac{1}{\eta_T} \left(\frac{T_{05}}{T_{04}} - 1 \right), \quad (4.21)$$

$$\frac{p_{05}}{p_{04}} = \left(\frac{T_{05s}}{T_{04}} \right)^{\frac{\gamma^T}{\gamma^T - 1}} = \left[1 + \frac{1}{\eta_T} \left(\frac{T_{05}}{T_{04}} - 1 \right) \right]^{\frac{\gamma^T}{\gamma^T - 1}}. \quad (4.22)$$

- Nozzle exit condition: From enthalpy conservation

$$\frac{1}{2} u_e^2 = h_{05} - h_e = \eta_p (h_{05} - h_{es}), \quad (4.23)$$

$$\frac{1}{2} u_e^2 = \eta_p c_p T_{05} \left(1 - \frac{T_{es}}{T_{05}} \right), \quad (4.24)$$

and solving for u_e

$$u_e = \sqrt{2\eta_N c_p T_{05} \left[1 - \left(\frac{p_{es}}{p_{05}} \right)^{\frac{\gamma_N - 1}{\gamma_N}} \right]} \quad (4.25)$$

for an unchoked nozzle flow.

For the performance analysis, we are mostly interested in the following two parameters:

- Specific thrust:

$$\frac{T}{\dot{m}_A} = [(1 + f)U_e - U_0]; \quad (4.26)$$

- Specific fuel consumption:

$$\frac{\dot{m}_F}{T} = \frac{f}{[(1 + f)U_e - U_0]}. \quad (4.27)$$

Performing the real-Brayton-cycle analysis for a range of pressure ratios and Mach-numbers provides information about the engine performance. These results are schematically illustrated in Figs. 4.10 to 4.11:

- For given M and T_{04} , π_C for the minimum fuel consumption and the maximum thrust do not coincide. Both \dot{m}_F and T_{04} require consideration for selecting best compressor pressure ratio.
- Increasing T_{04} substantially improves thrust, maximum thrust $T_{\max} \sim 1700$ K is well below adiabatic flame temperature. Blade cooling and high-temperature alloys are required to facilitate thermal stability at these high combustor exit temperatures.
- Increase T_{04} can affect \dot{m}_F/T .
- π_C for supersonic flight is much less than that for subsonic condition (limit of ramjet).

4.3. Analysis of Turbofan Engines

From the general performance analysis (see Eq. (2.86)), we found that the overall efficiency is related to the propulsive and thermal efficiency, $\eta_o = \eta_p \eta_{th}$, with

$$\eta_p = \frac{2}{1 + \frac{U_e}{U_0}}.$$

Therefore, for a fixed η_{th} , we can maximize η_p and η_o by letting $U_e \rightarrow U_0$. For a turbojet engine, U_e is defined by the exit enthalpy and nozzle design. Considering different engine-design concepts, the relation between η_p and U_0 is shown in Fig. 4.13.

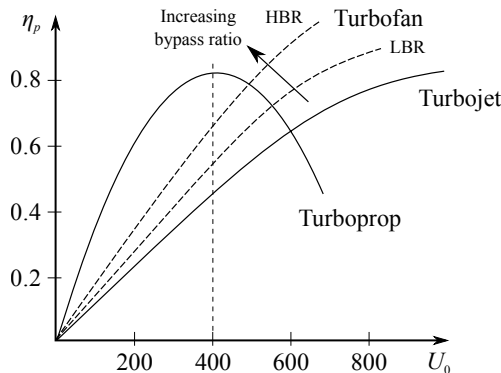


Figure 4.13: Relation between η_p and U_0 for different types of engines.

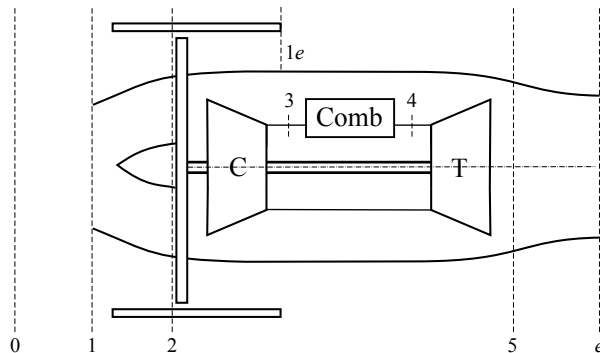


Figure 4.14: Schematic of the turbofan engine.

For a turboprop engine or unducted fan-engine, we obtain the highest bypass ratio since $\beta \rightarrow \infty$. However, these engines are limited by the flight Mach number

to less than 0.5 (so that the blade tip-speed doesn't exceed supersonic condition). For $M > 0.5$, the engine will become noisy and we will have supersonic tip velocity, shock waves and flow separation.

Recall the thrust equation for a turbofan engine (Fig. 4.14)

$$T = \dot{m}_{A,C} [(1+f)U_e + \beta U_{1e} - (1+\beta)U_0]. \quad (4.28)$$

We have

$$\text{TSFC} = \frac{\dot{m}_F}{T} = \frac{f}{(1+f)U_e + \beta U_{1e} - (1+\beta)U_0}. \quad (4.29)$$

The analysis of a turbofan engine follows that of the turbojet engine with some additional component analysis:

- Fan inlet condition: Air is supplied from the diffusor, so that pressure and temperature are identical to that of the core flow

$$T_{012} = T_{02}, \quad (4.30)$$

$$p_{012} = p_{02}. \quad (4.31)$$

- Fan outlet condition: Define fan pressure rate $\pi_F = \frac{p_{013}}{p_{02}}$ and fan adiabatic efficiency $\eta_F = \frac{h_{013s} - h_{012}}{h_{013} - h_{012}}$, we have

$$p_{013} = p_{02}\pi_F, \quad (4.32)$$

$$T_{013} = T_{02} \left[1 + \frac{1}{\eta_F} \left(\pi_F^{\frac{\gamma_F-1}{\gamma_F}} - 1 \right) \right]. \quad (4.33)$$

- Fan nozzle exit condition: The evaluation of the fan-nozzle exit velocity directly follows from the enthalpy conservation:

$$u_{1e} = \sqrt{2\eta_{NF} c_p T_{013} \left[1 - \left(\frac{p_0}{p_{013}} \right)^{\frac{\gamma_F-1}{\gamma_F}} \right]}. \quad (4.34)$$

- Turbine exit condition: Considering work-balance between compressor and turbine provides a relation to evaluate the turbine work that is required to drive the compressor and fan:

$$(\dot{m}_{A,C} + \dot{m}_F)c_p^T(T_{05} - T_{04}) = -\dot{m}_{A,C}c_p^C(T_{03} - T_{02}) - \dot{m}_{A,B}c_p^F(T_{013} - T_{02}). \quad (4.35)$$

With $\beta = \dot{m}_{A,B}/\dot{m}_{A,C}$, we can simplify:

$$(1+f)c_p^T(T_{05} - T_{04}) = -c_p^C(T_{03} - T_{02}) - \beta c_p^F(T_{013} - T_{02}), \quad (4.36)$$

$$T_{05} = T_{04} - \frac{c_p^C(T_{03} - T_{02}) + \beta c_p^F(T_{013} - T_{02})}{(1+f)c_p^T}, \quad (4.37)$$

with $f \sim 0$ and $c_p = c_p^T = c_p^C$, we have

$$T_{05} = T_{04} - (T_{03} - T_{02}) - \beta(T_{013} - T_{02}). \quad (4.38)$$

The pressure at the turbine exit can be obtained using the same expression as shown in Eq. (4.22) for the turbojet.

- Nozzle exit condition:

$$u_e = \sqrt{2\eta_N c_p^N T_{05} \left[1 - \left(\frac{p_{es}}{p_{05}} \right)^{\frac{\gamma_N - 1}{\gamma_N}} \right]},$$

where $p_{es} = p_0$.

Some remarks are in order:

- The main benefit of higher bypass ratios is achieved at take-off condition
- The benefit of the higher bypass ratio reduces with increasing flight Mach number and altitude
- No benefits of bypass ratio at trans/supersonic conditions; losses due to the increase engine cross-section and shock losses exceed the gain that is achieved by the bypass ratio
- For aircraft operating at sub/supersonic conditions, it is essential to optimize the design of the bypass ratio
- Criteria for limitation on bypass ratio:
 - Speed mismatch between fan and turbine
 - Weight consideration
 - Aerodynamic drag
 - Gear box design.

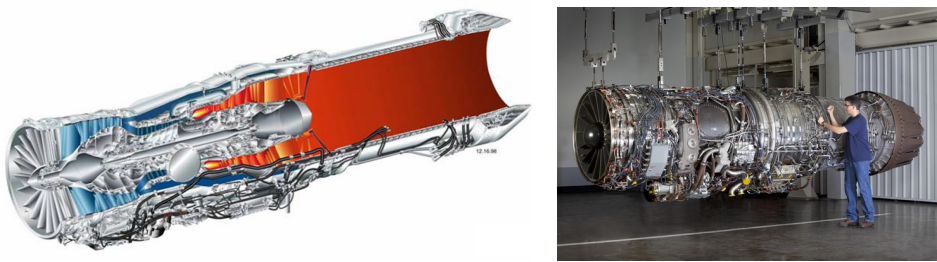
4.4. Examples of Turbofan Engines

This section provides a summary of relevant turbofan engines that are currently employed as propulsion systems for military and civil aircraft.

4.4.1. Military Aircraft Engines.

Pratt & Whitney F135: The Pratt & Whitney F135 propulsion system, shown in Fig. 4.15, is the engine of choice for the advanced, single-engine tactical fighter F-35 (Joint Strike Fighter, JSF), which has been developed by Lockheed Martin. The F-35 has unique capabilities for land-based conventional takeoff and landing (CTOL), carrier-variant takeoff and landing (CVTOL) and short takeoff and vertical landing (STOVL). The F135 propulsion system has already proved that it can meet these diverse requirements. As planned, the new F-35 JSF aircraft will replace the F-16 Fighting Falcon, A-10 Thunderbolt II, AV-8B Harrier, and F/A-18 Hornet.

The F135 is an evolution of the F119-PW-100, a technologically advanced turbofan that powers the Air Force's F/A-22 Raptor. It integrates the proven F119 core (see Paragraph 4.4.1.1), a high-performance six-stage compressor and single-stage turbine unit with a new low-pressure spool. In addition, the propulsion system features advanced prognostic and on-condition management systems that provide maintenance awareness, autonomic logistic support, and automatic field data and test systems. All line-replaceable components (LRCs) can be removed and replaced with a set of six common hand tools. The first production propulsion system for operational service was scheduled for delivery in 2007.



(a) Engine schematic.

(b) Engine assembly.

Figure 4.15: Schematic and image of Pratt & Whitney's F135 engine (source: www.pw.utc.com).

Engine Characteristics:

- *Thrust*: 43,000 lbf (191.35 kN).
 - *Intake*: Ring of 21 fixed radial guide vanes, with hinged trailing flaps, which carry front LP bearing.
 - *Fan (LP Compressor)*: Three integrally bladed rotors, derived from F119 but with new features giving greater mass flow with higher pressure ratio, improved stability, maximum resistance to bird and other impact damage, and minimum signature. Rotors 2 and 3 are made of flank-milled titanium alloy.
 - *HP Compressor*: Six-stage compressor derived from F119, rotating in opposition to LP spool. Split forward case in titanium alloy housing two stages of asymmetric variable-incidence guide vanes (stators). Cast nickel-alloy rear stators grouped in segments in titanium-alloy ring casing of high creep strength. All stators integrally bladed, either flat-milled like the fan or high-speed milled.
 - *Combustor*: Short annular diffuser/combustor, derived from F119. Outer casing about 762 mm in both diameter and length, weighing 91 kg including HPT nozzle ring (lighter and less costly than in previous P&W fighter engines), handling airflow at 4,150 kPa at 649°C, and containing air-conditioning connections. The combustion chamber is 510 mm in diameter and 230 mm long, weighting 32 kg. Liner with impingement and film cooling containing Floatwall ceramic-coated nickel-based cast segments, each containing “thousands of holes”, which “float” from their anchored location. Intense combustion with fuel/air ratio 20 per cent higher than in F100 engine to give near-record gas temperature exceeding 2,200°C (4,000F).
 - *HP Turbine*: High-pressure single stage turbine based on F119, with advanced airfoil coating and cooling derived from F119, but with cooling airflow doubled. Impingement cooling augmented by closing down rear stator angles. Nozzle ring c120 organic-matrix vanes with wall thickness 0.5 mm. The rotor comprises a main disk, miniature disk and cover

plates, all incorporating the same high-strength powder-metallurgy (sintered) high-rotor blades of second-generation single-crystal Ni-based alloy, with advanced outer air seals. Unit diameter 914 mm, length 356 mm, weight 183 kg. The HPT rotates at speeds exceeding 15,000 rpm, generating 47,725 kW from gas at just over 1,649°C, cooled by air supplied at 538°C from the HPC. To minimize pressure loss the rotor blades are cooled by Tangential On-Board Injection (TOBI), each blade being a complex casting with multiple cooling passages. Growth in blade-tip diameter is controlled by a unique slow-responding thermally isolated support ring in materials selected for their low thermal expansion, giving passive clearance control through the normal engine-operating range.

- *LP Turbine:* Two-stage design giving significantly greater shaft power than the single-stage LPT of the F119. Rotates in opposition to the HP turbine. Typical of the simplified design of the F135 are the main shaft bearings, (see note under HP compressor), and it is possible that the full production F135 may have a corrosion-resistant ceramic (silicon nitride) bearing.
- *Afterburner:* Advanced flame-holder system. Fully variable convergence-divergence nozzle, with 15 hydraulically driven hinged flaps, controlling propulsive jet at 621 kPa at up to 1,927°C. In the F135-PW-600 the complete nozzle can vector through 95° in 2.5 s to give 80.34 kN lift force for STOVL, driven by a Smiths Aerospace actuation system.

Variants	F135-PW-100: F-35A Conventional take-off and landing F135-PW-400: F-35C Carrier variant F135-PW-600: F-35B Short take-off vertical landing
Dimensions	F135-PW-100/400: Length 5,588 mm, diameter 1,295 mm F135-PW-600: Length 9,373 mm, diameter 1,295 mm
Maximum thrust	43,000 lbf (191.35 kN)
TSFC	0.886 lb/(lbf-h), 25 mg/(N-s) (without afterburner)
Thrust-to-weight ratio	11.5
Implementation	F-35

Table 1: Engine specification for F135.

4.4.1.1. *Pratt & Whitney F119:* Pratt & Whitney's F119 turbofan engine, the world's most technologically advanced aircraft engine in production, meets the need for greater speed and lower weight for new military weapon systems. In the 35,000 pound thrust class, the engine is a dual spool, counter-rotating turbofan that enables aircraft operation at supersonic speeds for extended periods without thrust augmentation.

The F119 is equipped with a number of advanced technologies: Its three-stage fan has shroudless titanium fan blades and is powered by a single-stage

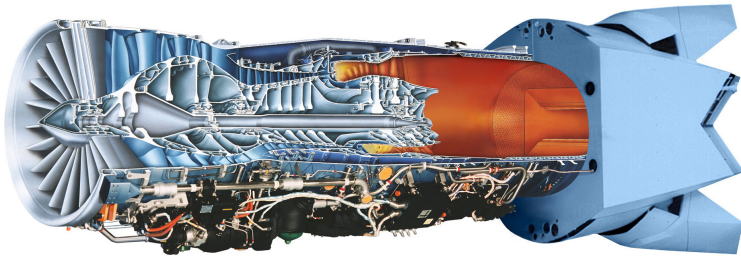


Figure 4.16: Schematic of Pratt & Whitney's F119 engine (source: www.pw.utc.com).

low-pressure turbine. The engine's core has an aerodynamically efficient six-stage compressor driven by a single-stage high-pressure turbine featuring the next generation of single-crystal super-alloy blades with improved cooling management. The robust, but compact, high-pressure compressor features integrally bladed rotor disks for improved durability. The engine delivers unparalleled aircraft maneuverability with its unique two-dimensional thrust vectoring exhaust nozzle. This convergent/divergent nozzle vectors thrust 20° either up or down. Nozzle position management is automatically controlled by the full-authority digital electronic control (FADEC), which controls hundreds of other engine and aircraft operating parameters. The FADEC also features advanced diagnostic and on-condition management systems for maintenance awareness, autonomic logistics support, and automatic field data and test systems.

Engine Type	Twin-Spool, augmented turbofan
Thrust	35,000 lb Thrust class
Compressor	Twin-spool/Counter-rotating/Axial flow
Combustor	Annular
Turbine	Axial flow/Counter-rotating
Nozzle	Two Dimensional Vectoring Convergent/Divergent
Implementation	F/A-22 Raptor

Table 2: Specification of F119 engine.

4.4.1.2. *Pratt & Whitney F100:* Pratt & Whitney's family of F100 engines is the mainstay of air forces worldwide. With more than 6,900 engines produced and over 16 million flight hours, the F100 is the safest and most reliable fighter engine in the world. It is the only Increased Performance Engine (IPE) operationally matured in both the F-15E and F-16 Block 52 aircraft. Using technology developed from the F119 and F135 engine programs for the F/A-22 Raptor and F-35 Joint Strike Fighter, the current production PW-229 incorporates modern turbine materials, cooling management techniques, compressor aerodynamics and electronic controls.

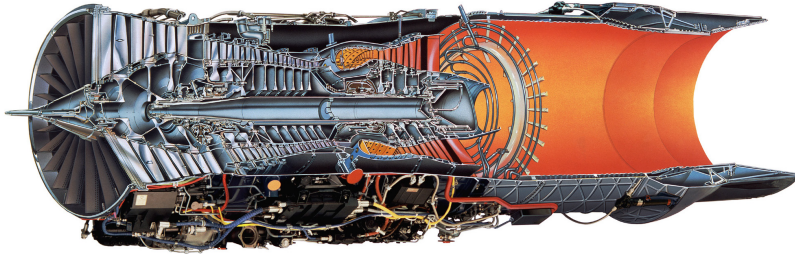


Figure 4.17: Schematic of Pratt & Whitney's F100 engine (source: www.pw.utc.com).

Engine Thrust	23,770–29,160 lb
Dimensions	Weight: 3,740 lb, length: 191 in, diameter: 46.5 in
Bypass Ratio	0.36
Overall Pressure Ratio	25–32
Implementation	F-15, F-16

Table 3: Specification of F100 engine.

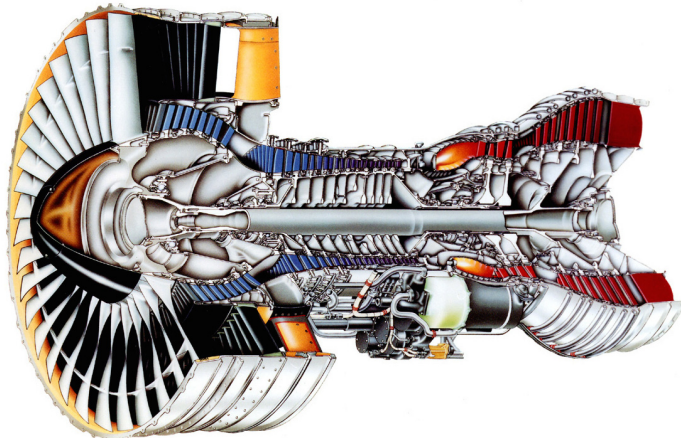
4.4.2. Civil Aircraft Engines.

4.4.2.1. *Pratt & Whitney JT9D*: These engines opened a new era in commercial aviation: the high-bypass-ratio engine to power wide-bodied aircraft. Although production ended in 1990, Pratt & Whitney continues to support the JT9D family. Upgrade programs are in place to enable operators to improve durability, increase thrust and reduce noise.

Dimensions	Fan tip diameter: 93.4 in, Length: 132.7 in
Takeoff thrust	48,000–56,000 lb
Bypass ratio	0.36
Overall pressure ratio	26.7
Fan pressure ratio	1.67
Implementation	Boeing {747,767}, Airbus {A300,A310}, McDonnell Douglas DC-10

Table 4: Engine characteristics of PW-JT9D engine.

4.4.2.2. *Pratt & Whitney PW4000*: Today's PW4000 meets all current and anticipated emissions and noise regulations with margin. For a further reduction in emissions – especially NO_x – TALON (Technology for Advanced Low NO_x) combustor technology is now available as an option. Derived from the 112-inch fan model, TALON has segmented, replaceable liner panels for easy maintainability and air blast fuel nozzles for excellent fuel atomization and mixing.

Figure 4.18: Cutaway of PW 4000 (source: www.pw.utc.com).

Thrust range	52,000–62,000 lb
Dimensions	Fan diameter: 94 in, Length: 132.7 in
Bypass ratio	4.8–5.1
Overall pressure ratio	27.5–32.3
Fan pressure ratio	1.65–1.80
Implementation	Boeing {747-400,767-200/300}, Airbus {A300-600,A310-300}, McDonnell Douglas MD-11

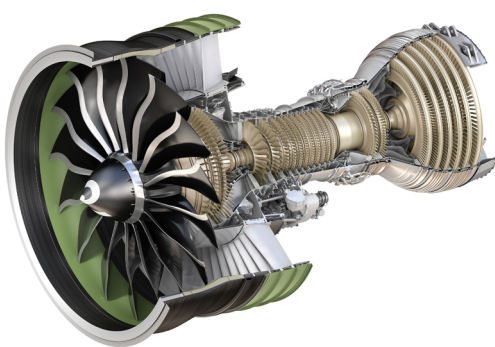
Table 5: Engine characteristics of PW 4000 engine.

4.4.2.3. General Electric GE90: The GE90 represents GE's investment in the future of wide-body aircraft. Over the past two decades, GE's CF6 and CFM56¹ engines have been chosen to power more than 50 percent of all new aircraft ordered with a capacity of 100 passengers or more. The GE90 combines the best proven technology from these engine programs, NASA and military programs with advanced technology to provide a highly reliable, fuel-efficient powerplant for the next generation of wide-body aircraft.

Originally certified in 1995 at 84,700 pounds of thrust, today's GE90 engines power newer, more advanced Boeing 777 aircraft capable of flying farther, faster and more efficiently than their predecessors. The most recent derivative of the GE90, the GE90-115B, is the sole powerplant for Boeing's longer-range 777-300ER and 777-200LR aircraft. The GE90-115B is certified at 115,000 lbs of thrust and has broken a number of aviation records. The Guinness Book of World Records recognized the engine as the "World's Most Powerful Commercial Jet Engine" in

¹CFM56 engines are produced by CFM International, a 50/50 joint company between Snecma Moteurs and General Electric Company

2001 after it recorded an amazing 123,000 lbs of steady-state thrust while undergoing initial ground testing. In late 2002, the engine shattered its original record by reaching 127,900 lbs of thrust during required certification testing.



(a) Engine schematic.



(b) Engine assembly.

Figure 4.19: Schematic and image of GE90-115B engine (source: www.geaviation.com).

The GE90-115B engine was designed, initially for 511.6 kN (115,000 lbs). The most obvious change is an even larger fan, with so-called ‘swept’ blades. This is driven by an upgraded LP turbine, via a mid-shaft of improved material. By July 2000, testing of the nine-stage HPC, with Stage-4 variable stator vane (VSV) removed, was essentially complete, with VSV schedule optimized. The first new fan mid-shaft was finish-machined at IHI in Japan in March 2000. At that time the planned number of test cycles was 14,400, following 17,876 on the original GE90-76B/85B engines. Of course, the larger GE90-110B and GE90-115B engines require an enormous redesigned nacelle, hung on considerably modified struts, but this counts as airframe. It was first attached to GE’s 747 testbed, which completed its testing in 48 flights (217 h) over a 152-day period ending in April 2003. By that time a prolonged maturation program had begun, in which three engines have been put through 30,000 cycles of simulated operation by GE, Snecma and IHI. Of these, 13,000 cycles were logged by the first maturation engine (906-001), which was to be put through five shop visits (a surprisingly modest average of 2,600 cycles per visit). The second maturation engine, 906-003, was scheduled to make two 3,000-h ETOPS (Extended range Twin Operations) demonstrations. The third engine, 906-006, will run three operating blocks of 3,000, 3,500 and 4,000 cycles, mainly in studying the hot section. This program ended in 2006. Flight testing of the first two B777-300 aircraft confirmed that air miles per unit fuel burn are about one per cent better than predicted. A record set during these tests was a single-engine ETOPS of 6 h 29 min. The engine and 777-300ER aircraft were finally certificated (jointly by the FAA and the newly formed EASA) on 15 March 2004. First aircraft delivery (to ILFC, for lease to Air France) was achieved in late April,

entering service on 10 May. By autumn 2005, two customers, Air France and the 12 new Icelandic carrier Avion, had taken delivery of the first B777 freight aircraft powered by the GE90-110B1 engine. Like earlier GE90 engines, the GE90-115B engines are assembled at Durham, North Carolina.

Thrust range	115,300 lb
Dimensions	Fan diameter: 128 in, Length: 216 in
Fan/Compressor	1F/4LPC/9HPC
Stages	
HPT/LPT	2/6
Bypass ratio	9
Overall pressure ratio	42
Implementation	Boeing 777-200/300

Table 6: GE90 engine specifications.

4.4.2.4. General Electric GEnx: The GEnx-engine (GE Next Generation) family is a derivation of the GE90-engine, and has been developed for the Boeing 787 Dreamliner. The GEnx will feature an advanced TAPS (twin annular premixed swirl) combustor that will produce a lower temperatures and more uniform gas stream temperature profile. The GEnx represents a giant leap forward in propulsion technology. The engine will use the latest generation materials and design processes to reduce weight, improve performance and lower maintenance. The GEnx will deliver 15 % better specific fuel consumption than the engines it replaces. It is designed to stay on wing 30 % longer, while using 30 % fewer parts, greatly reducing maintenance. The GEnx's emissions will be as much as 95 % below current regulatory limits, ensuring clean compliance for years to come, and it will be the quietest, most passenger-friendly commercial engine ever produced. All of the these improvements are thanks to the incorporation of advanced and proven technologies from other engine families and on-going R&D programs. Like lightweight, durable composite materials and specialized coatings. An innovative, clean-burning combustor, a counter-rotating architecture, and a fan module that's virtually maintenance free.

4.4.2.5. Rolls-Royce AE 3007: The Rolls-Royce AE 3007 is a high-bypass turbofan engine produced by Rolls-Royce North America, sharing a common core with the Rolls-Royce T406 (AE 1107) and AE 2100. The AE 3007 is a direct drive turbofan engine with a single stage fan, a 14-stage axial compressor with 6 stages of variable vanes including inlet guide vanes, an annular combustor, a two-stage high pressure turbine and a 3-stage low pressure turbine. The accessory gearbox is mounted at its bottom and two single channel FADEC units are mounted in the aircraft. It has fore and aft mounting provisions for underwing pylon or aft fuselage installation.

Dimensions	Fan tip diameter: 38.5 in, Length: 115.08 in
Takeoff thrust	6,442–7,042 lb (AE 3007C) 7,580–9,440 lb (AE 3007A)
Bypass ratio	5
Overall pressure ratio	23
Implementation	Cessna Citation X, Embraer ERJ 145 family, RQ-4 Global Hawk/MQ-4C Triton

Table 7: Engine characteristics of AE 3007 engine.

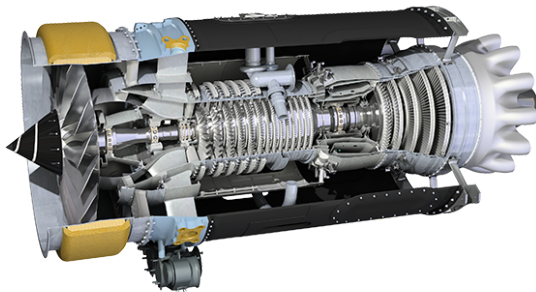


Figure 4.20: Cutaway of AE 3007 (source: www.rolls-royce.com).

CHAPTER 5

Gas Turbine Engine Components

5.1. Combustion and Combustor

5.1.1. Combustion Fundamentals. Combustion is the process of converting chemical bond energy into thermal energy. Combustion processes are characterized by chemical reactions and here we will only consider overall/global reactions.

Global reactions or overall reactions represent stoichiometric relations among major species which are a result of (systematic) reduction of a detailed (complex) kinetics mechanism to a simpler reaction sequence, involving a small number of reactions and species. Contribution of intermediate and other species is ignored.

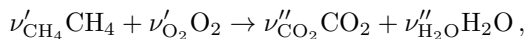
Consider a global reaction:

$$\sum_i \nu'_i A_i \xrightarrow{k_g} \sum_i \nu''_i A_i, \quad (5.1)$$

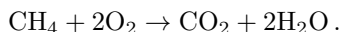
with A_i : chemical species i ; ν'_i, ν''_i : stoichiometric coefficients or mole-number of species i for reactants and products; and k_g : rate coefficient.

The definition of *stoichiometric condition* is: a fuel-to-oxidizer ratio at which the reactants burn completely to form stable products only (CO_2 , H_2O , for hydrocarbon fuels). In other words, under stoichiometric conditions neither fuel nor oxygen is present in excess in the product mixture (equivalent to chemically correct, 100% theoretical air, 0% excess air). This is thermodynamically the most economic reaction.

To find the stoichiometric coefficients, ν'_i, ν''_i , we need to enforce atomic balance, that is the number of atoms of reactants is equal to the number of atoms of the products. Consider the following reaction:



we have three equations for the four stoichiometric coefficients from the balance of atoms C, H, and O. The results from the elemental mass balance are given in **Table 1**. The resulting system is undetermined, since we have 3 equations in 4 unknowns. To overcome this, we are normalizing the equation with respect to the fuel by setting $\nu'_{\text{CH}_4} = 1$. With this, we can solve for: $\nu'_{\text{O}_2} = 2$, $\nu''_{\text{CO}_2} = 1$, and $\nu''_{\text{H}_2\text{O}} = 2$, resulting in the following stoichiometric reaction:



element i	Balance ν'	Balance ν''
O	$2\nu'_{\text{O}_2}$	$2\nu''_{\text{CO}_2} + \nu''_{\text{H}_2\text{O}}$
H	$4\nu'_{\text{CH}_4}$	$2\nu''_{\text{H}_2\text{O}}$
C	ν'_{CH_4}	ν''_{CO_2}

Table 1: Elemental balance.

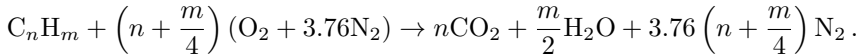
Generally, stoichiometry is characterized through the *equivalence ratio* ϕ :

$$\phi = \frac{\dot{m}_{\text{Fuel}}/\dot{m}_{\text{Air}}}{(\dot{m}_{\text{Fuel}}/\dot{m}_{\text{Air}})_{\text{st}}} = \frac{f}{f_{\text{st}}}. \quad (5.2)$$

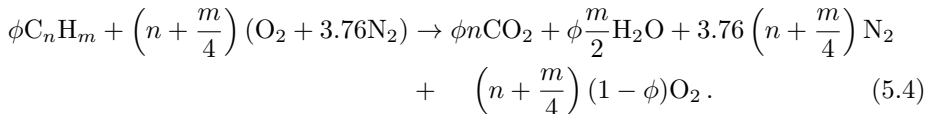
where f is the fuel/air ratio. Depending on the numerical value of ϕ , we distinguish between the following conditions:

$$\phi = \begin{cases} < 1: & \text{fuel-lean condition} \\ = 1: & \text{stoichiometric} \\ > 1: & \text{fuel-rich condition} \end{cases}. \quad (5.3)$$

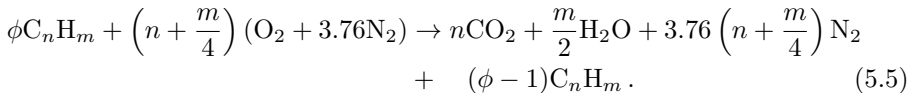
Consider combustion of hydrocarbon fuel with air. Air consists of 21% O_2 and 79% N_2 (by volume). Expressed in terms of mole-fraction ratio, this is $X_{\text{N}_2}/X_{\text{O}_2} = 0.79/0.21 = 3.76$, meaning that for each mole of air we have 3.76 mole of N_2 . Therefore, for stoichiometric combustion ($\phi = 1$):



For fuel-lean combustion ($\phi < 1$):



For fuel-rich combustion ($\phi > 1$):



5.1.1.1. Heat/Enthalpy of Reaction/Combustion. Recall the thermal efficiency of an ideal Brayton cycle: $\eta_{\text{th}} = 1 - T_4/T_2$. Combustor exit temperature is directly related to the thermal efficiency of the Brayton cycle. The question we want to answer is how to compute the combustor exit temperature.

To answer this question, we consider an energy balance between chemical bond energy and sensible energy. Recall that we introduced the sensible enthalpy as a measure for storing internal energy (no bond breaking). The sensible energy, however, doesn't account for the energy that is stored in the molecular bonds. A measure for the chemical-bond energy is the chemical energy or *heat of formation*: h_f^0 where the superscript “0” refers to the reference state, and the subscript “f” indicates that this is the formation enthalpy.

The heat of formation is measured with respect to a reference state (consisting of a set of reference species, reference temperature and pressure). In the following, we define the references state as:

$$T_{\text{ref}} = 298.15 \text{ K} \quad \text{and} \quad p_{\text{ref}} = 1 \text{ bar},$$

and the reference species correspond to all elements in their stable form; that is H_2 , O_2 , N_2 , etc. For these species, the formation enthalpy is by definition zero:

$$h_{f,\text{O}_2}^0 = 0, \quad h_{f,\text{N}_2}^0 = 0, \quad h_{f,\text{H}_2}^0 = 0.$$

The physical meaning of the formation enthalpy is: the amount of energy that is required to form a compound (molecule) from its elemental components (reference species) at the reference state:

$$h_f^0 = h_f^0(\text{Compound}) - \sum_i a_i h_f^0(\text{Element})$$

where a_i is the number of atoms of element i contained in the compound. A list of formation enthalpies is given in [Table 2](#).

The heat of reaction H_r^0 corresponds to the change in the heat of formation, h_f^0 , resulting from chemical transformation of reactants into products:

$$\begin{aligned} H_r^0 &= \left(\sum_i^{N_s} \nu_i'' h_{f,i}^0 \right)_{\text{Products}} - \left(\sum_i^{N_s} \nu_i' h_{f,i}^0 \right)_{\text{Reactants}} \\ &= \sum_i^{N_s} (\nu_i'' - \nu_i') h_{f,i}^0 \end{aligned} \quad (5.6)$$

in which the summation i is over all species participating in the reaction and

$$H_r^0 = \begin{cases} < 0: & \text{exothermic} \\ > 0: & \text{endothermic} \end{cases}. \quad (5.7)$$

In the combustion community often the notion of heating value (HV) is used, which is defined as:

$$HV = -H_r^0. \quad (5.8)$$

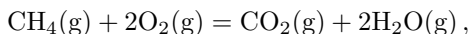
Water is a major reaction product and is typically contained in gaseous form $\text{H}_2\text{O}(g)$ in the product stream. In this case, not all enthalpy of the water is liberated as heat, so that this state is referred to as lower heating value (LHV). If, however, the water is present in liquid form, $\text{H}_2\text{O}(l)$, more heat is release, which comes from the transition from the gaseous to the liquid state. This is referred to as higher heating value (HHV). The difference between LHV and HHV is the latent heat of vaporization, corresponding to the heat that is required for the condensation/vaporization of the water.

Substance	Formula (state)	$\bar{h}_f^o(T)$ kcal/mol	Substance	Formula (state)	$\bar{h}_f^o(T)$ kcal/mol
Aluminum Oxide	$\text{Al}_2\text{O}_3(s)$	-400.5	Hydrogen Cyanide	$\text{HCN}(g)$	32.3
Diborane	$\text{B}_2\text{H}_6(g)$	8.5	Formaldehyde	$\text{CH}_2\text{O}(g)$	-26.0
Boron Oxide	$\text{B}_2\text{O}_3(s)$	-304.4	Formic Acid	$\text{CH}_2\text{O}_2(l)$	-101.6
Bromine Atom	$\text{Br}(g)$	26.7	Nitromethane	$\text{CH}_3\text{NO}_2(g)$	-17.9
Bromine	$\text{Br}_2(g)$	7.4	Methylnitrate	$\text{CH}_3\text{NO}_3(g)$	-29.8
Hydrogen Bromide	$\text{HBr}(g)$	-8.7	Methane	$\text{CH}_4(g)$	-17.8
Calcium Carbonate	CaCO_3	-288.5	Methanol	$\text{CH}_3\text{O}(l)$	-57.1
Calcium Oxide	$\text{CaO}(s)$	-151.7	Carbon Monoxide	$\text{CO}(g)$	-26.4
Chlorine Atom	$\text{Cl}(g)$	29.0	Carbon Dioxide	$\text{CO}_2(g)$	-94.0
Hydrogen Chloride	$\text{HCl}(g)$	-22.1	Acetylene	$\text{C}_2\text{H}_2(g)$	54.5
Fluorine Atom	$\text{F}(g)$	19.0	Ethylene	$\text{C}_2\text{H}_4(g)$	12.5
Hydrogen Fluoride	$\text{HF}(g)$	-65.3	Acetaldehyde	$\text{C}_2\text{H}_4\text{O}(g)$	-39.7
Iron Oxide	Fe_3O_4	-267.3	Ethylene Oxide	$\text{C}_2\text{H}_4\text{O}_2(g)$	-12.6
Hydrogen Atom	$\text{H}(g)$	52.1	Acetic Acid	$\text{C}_2\text{H}_4\text{O}_2(l)$	-115.8
Iodine Atom	$\text{I}(g)$	25.5	Ethane	$\text{C}_2\text{H}_6(g)$	-20.2
Hydrogen Iodide	$\text{HI}(g)$	6.3	Ethanol	$\text{C}_2\text{H}_6\text{O}(l)$	-66.4
Iodine	$\text{I}_2(g)$	14.9	Dimethyl Ether	$\text{C}_2\text{H}_6\text{O}(g)$	-44.0
Magnesium Oxide	$\text{MgO}(s)$	-143.8	Cyanogen	$\text{C}_2\text{N}_2(g)$	73.3
Nitrogen Atom	$\text{N}(g)$	113.0	Allene	$\text{C}_2\text{H}_4(g)$	45.5
Ammonia	$\text{NH}_3(g)$	-11.0	Propyne	$\text{C}_3\text{H}_4(g)$	44.2
Nitric Oxide	$\text{NO}(g)$	21.6	Propene	$\text{C}_3\text{H}_6(g)$	4.8
Nitrogen Dioxide	$\text{NO}_2(g)$	7.9	Cyclopropane	$\text{C}_3\text{H}_6(g)$	12.7
Hydroazaine	$\text{N}_2\text{H}_4(g)$	22.8	Acetone	$\text{C}_3\text{H}_6\text{O}(g)$	-51.9
Nitrous Oxide	$\text{N}_2\text{O}(g)$	19.6	Propylene Oxide	$\text{C}_3\text{H}_6\text{O}(g)$	-22.6
Oxygen Atom	$\text{O}(g)$	59.6	Propane	$\text{C}_3\text{H}_8(g)$	-25.0
Hydroxyl	$\text{OH}(g)$	9.3	1,2-Butadiene	$\text{C}_4\text{H}_6(g)$	38.8
Water	$\text{H}_2\text{O}(g)$	-57.8	1,3-Butadiene	$\text{C}_4\text{H}_6(g)$	26.3
Hydrogen Peroxide	$\text{H}_2\text{O}_2(g)$	-32.6	<i>n</i> -Butane	$\text{C}_4\text{H}_{10}(g)$	-30.0
Ozone	$\text{O}_3(g)$	34.1	iso-Butane	$\text{C}_4\text{H}_{10}(g)$	-32.1
Disilane	$\text{Si}_2\text{H}_6(g)$	19.2	Diethyl Ether	$\text{C}_4\text{H}_{10}\text{O}(g)$	-60.3
Silane	$\text{SiH}_4(g)$	8.2	<i>n</i> -Pentane	$\text{C}_5\text{H}_{12}(g)$	-35.1
Silicon Dioxide	$\text{SiO}_2(s)$	-217.7	iso-Pentane	$\text{C}_5\text{H}_{12}(g)$	-36.7
Sulfur Dioxide	$\text{SO}_2(g)$	-70.9	Benzene	$\text{C}_6\text{H}_6(g)$	19.8
Sulfur Trioxide	$\text{SO}_3(g)$	-94.6	Cyclohexane	$\text{C}_6\text{H}_{12}(g)$	-29.5
Titanium Oxide	$\text{TiO}_2(s)$	-225.6	<i>n</i> -Hexane	$\text{C}_6\text{H}_{14}(g)$	-39.9
Graphite	$\text{C}(s)$	0.0	Toluene	$\text{C}_7\text{H}_8(g)$	12.0
Carbon	$\text{C}(g)$	171.3	<i>n</i> -Heptane	$\text{C}_7\text{H}_{16}(g)$	-44.9
Carbon Tetrachloride	$\text{CCl}_4(g)$	-22.9	<i>o</i> -Xylene	$\text{C}_8\text{H}_{10}(g)$	4.6
Trichloromethane	$\text{CHCl}_3(g)$	-24.8	<i>n</i> -Octane	$\text{C}_8\text{H}_{18}(g)$	-49.9
Dichloromethane	$\text{CH}_2\text{Cl}_2(g)$	-22.9	iso-Octane	$\text{C}_8\text{H}_{18}(g)$	-53.5
Chloromethane	$\text{CH}_3\text{Cl}(g)$	-19.6	<i>n</i> -Hexadecane	$\text{C}_{16}\text{H}_{34}(g)$	-89.6

Table 2: Heat of formation at reference conditions: $p_{\text{ref}} = 1 \text{ atm}$ and $T_{\text{ref}} = 298.15 \text{ K}$ [19].

Example: Consider the stoichiometric oxidation of methane, compute the heat of combustion H_r^0 .

Solution: To answer this question, we start by writing the stoichiometric reaction:



and the heat of combustion is computed as

$$\Delta H_r^0 = (\nu''_{\text{CO}_2} h_f^0 + \nu''_{\text{H}_2\text{O}} h_f^0) - (\nu'_{\text{CH}_4} h_f^0 + \nu'_{\text{O}_2} h_f^0), \quad (5.9)$$

and with values from [Table 2](#):

$$\begin{aligned} h_{f,\text{CO}_2}^0 &= -94 \text{ kcal/mol} \\ h_{f,\text{H}_2\text{O}}^0 &= -57.8 \text{ kcal/mol} \\ h_{f,\text{O}_2}^0 &= 0 \quad (\text{Reference Species}) \\ h_{f,\text{CH}_4}^0 &= -17.8 \text{ kcal/mol} \end{aligned}$$

resulting in

$$H_r^0 = -191.8 \text{ kcal}. \quad (5.10)$$

That means that we liberate 802.5 kJ of energy when combusting 1 mole of methane with oxygen at stoichiometric conditions.

5.1.1.2. Adiabatic Flame Temperature. The adiabatic flame temperature T_{ad} corresponds to the temperature that is obtained when a homogeneous mixture at given initial temperature T_i reaches a chemical equilibrium through an adiabatic, isobaric process (“HP” – constant enthalpy, pressure). Since we are hereby only interested in the initial and final states of the combustion process, the adiabatic flame temperature is a thermodynamic concept and path-independent. Information about the adiabatic flame temperature is relevant for

- Selecting material and assessing thermal resistance;
- Determining the thermal efficiency;
- Combustion stability and knock-resistance;
- Analyzing pollutant emissions: NO_x and soot.

The adiabatic flame temperature can be evaluated from the first law of thermodynamics. For this we consider an open thermodynamic system without extraction of any work ($\delta W_t = 0$):

$$\delta Q = dH \quad \text{and} \quad dH = C_p(T)dT + H_f^0 \quad (5.11)$$

where $C_p = mc_p = \sum_i m_i c_{p,i}$.

Upon integration from state 1 (reactants) to state 2 (products) (see [Fig. 5.1](#) for graphical representation of the integration pathway) we obtain:

$$\begin{aligned} Q_{12} &= \int_1^2 dQ = \int_1^2 dH \\ &= \left. \int_{T_1=T_i}^{T_{1'}=T_0} C_p(T)dT \right|_{\text{Reactants}} + \underbrace{\int_{1'}^{2'} dH}_{H_r^0} + \left. \int_{T_2'=T_0}^{T_2=T_{ad}} C_p(T)dT \right|_{\text{Products}} \end{aligned} \quad (5.12)$$

where T_0 is the reference state at which we evaluate the formation enthalpy. Since we are considering an adiabatic process, $Q_{12} = 0$, the above equation can be solved by recognizing that $T_1 = T_i$, $T_{1'} = T_0$ (reference state), and $T_2 = T_{ad}$.

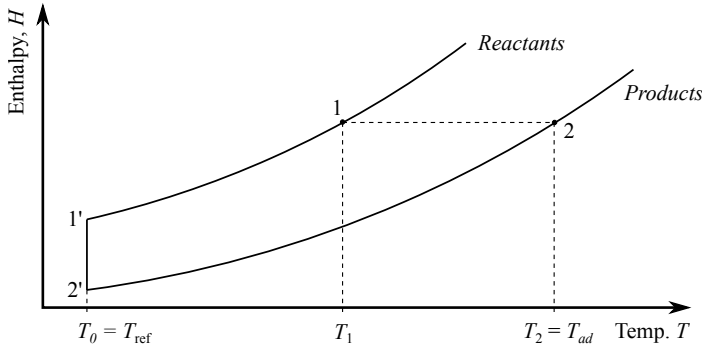
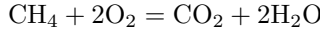


Figure 5.1: H - T diagram for evaluation of adiabatic flame temperature.

Adiabatic Flame Temperature of Methane Oxidation: Consider the combustion of a stoichiometric methane/oxygen mixture at a constant pressure of $p_0 = 1$ bar and initial temperature $T_i = 500$ K. Assume that only major products are formed, the gas is calorically perfect with $\gamma = 1.1$, and the system is adiabatic. Compute the adiabatic flame temperature T_{ad} ?

Solution: The global reaction for the methane/oxygen combustion is



and the enthalpy differential from the first law is

$$Q_{12} = 0 = \int_{T_1=T_i}^{T_{1'}=T_0} C_p(T) dT \Big|_{\text{Reactants}} + H_r^0 + \int_{T_{2'}=T_0}^{T_2=T_{ad}} C_p(T) dT \Big|_{\text{Products}} .$$

Note that this expression is formulated in units of energy, and we are not working with mass- or mole-specific quantities. Recall the following expressions for specific heat capacity, mass, and gas constant of species i :

$$C_{p,i} = m_i c_{p,i} , \quad c_{p,i} = \frac{\gamma}{\gamma - 1} R_i , \quad m_i = \nu_i M_i , \quad R_i = \frac{\mathcal{R}}{M_i} .$$

From Eq. (5.10) we found that the heat of combustion for this global reaction is $H_r^0 = -191.8$ kcal.

Upon integrating the energy equation, we obtain the following algebraic expression:

$$C_{p,\text{Reactants}}(T_0 - T_1) + H_r^0 + C_{p,\text{Product}}(T_{ad} - T_0) = 0 ,$$

and solving for T_{ad} gives:

$$\begin{aligned} T_{ad} &= T_0 - \frac{(T_0 - T_1) \sum_i \nu'_i + \frac{(\gamma-1)H_r^0}{\gamma \mathcal{R}}}{\sum_i \nu''_i} \\ &= 3425 \text{ K.} \end{aligned}$$

Note that an iterative approach is required to solve for T_{ad} for the case that the specific heat capacities are temperature-dependent.

Finally, we have some remarks on the specific heat capacity. We consider the mass-specific heat capacity of species “*i*”

$$c_{p,i} = \sum_{j=-2}^N a_j T^j \quad \left[\frac{\text{J}}{\text{kg} \cdot \text{K}} \right]$$

which is here written in polynomial form using NASA’s expressions. To compute the specific heat capacity of a mixture of *M* gases, we can weight each contribution on a mass-specific basis. This can be written as

$$m_{\text{mix}} c_{p,\text{mix}} = \sum_{j=1}^N m_j c_{p,j} ,$$

where $m_{\text{mix}} = \sum_{j=1}^N m_j$ is the total mass of the mixture, $m_j = M_j \nu_j$ is the mass of each species “*j*” (M_j : molecular weight, ν_j : mole number), $c_{p,\text{mix}}$ is the specific heat capacity of the mixture, and $c_{p,j}$ is the specific heat capacity of species “*j*”. By introducing the mass fraction of species “*j*” as

$$Y_j = \frac{m_j}{m_{\text{mix}}} = \frac{m_j}{\sum_i m_i} ,$$

we can write

$$c_{p,\text{mix}} = \sum_{j=1}^M Y_j c_{p,j} .$$

5.1.2. Combustor Requirements and Types. The requirements of the combustor include:

- Combustor efficiency (fuel conversion to convert all chemically bond energy into heat);
- Reliability, smooth ignition:
 - at ground;
 - at high altitude after flame-out;
- Wide stability limit (stable flame over range of pressures and fuel/air ratio);
- Low pressure losses;
- homogeneous combustor exit temperature profile (pattern factor) to maximize life of turbine blades and nozzle guide vanes;
- Low emissions of soot (smoke) and pollutants;
- No combustion instabilities;
- Reduce size and shape;
- Cost and ease of manufacturing;
- Maintainability;
- Durability;
- Multifuel capability.

Three main combustor types are (see Fig. 5.2):

- Tubular (can):

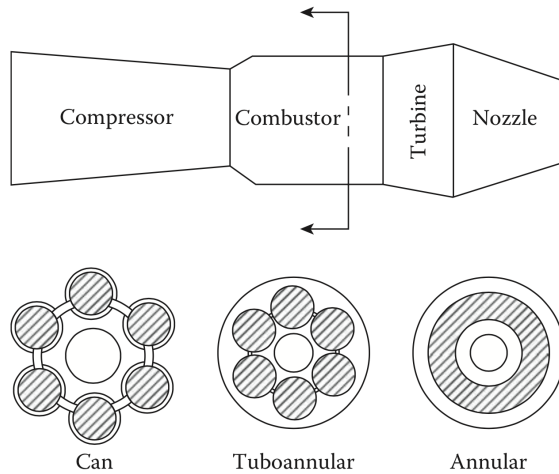


Figure 5.2: Three main combustor types [8].

- Cylindrical liner in cylindrical casing;
- Early engine designs (Whittle W2B, Juno 004);
- Advantages: inexpensive in design;
- Disadvantages: excessive length and weight (main application to industrial application for power generation).
- Tubo-annular (can-annular):
 - 6–10 tabular liners;
 - Inside single annular casing;
 - Compact design of annular chamber and mechanical stability of tubular combustor;
 - Need for interconnectors (cross-fire tubes);
 - GE J79, Olympus (Concorde).
- Annular:
 - Annular liner inside annular casing;
 - Compact design and low pressure-losses;
 - Issue: dynamic strength (buckling) integrated engine tests are expensive since it requires entire annular test;
 - GE90 and PW6000, etc.

Components of a typical rich-quench-lean combustor are illustrated in Fig. 5.3. Pattern Factor. We would like to achieve homogeneous/constant temperature at the combustor exit to reduce thermal stresses on turbine blades and to achieve

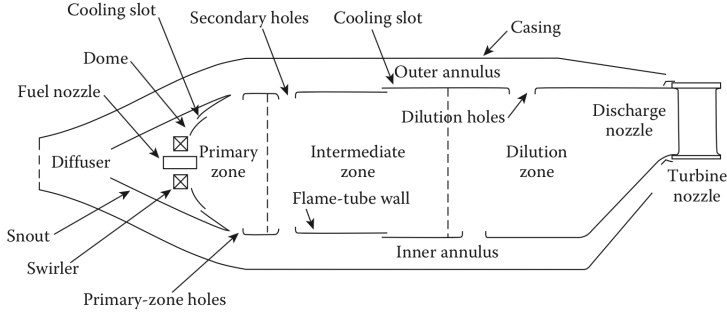


Figure 5.3: Main components of a conventional combustor [8].

homogeneous emission/temperature field. To characterize the temperature distribution, we introduce the *pattern factor* as (see Fig. 5.4):

$$\text{PF} = \frac{T_{4,\text{max}} - \bar{T}_4}{\bar{T}_4 - \bar{T}_3}. \quad (5.13)$$

For practical design considerations, we consider a pattern factor of $\text{PF} < 0.1$ as desirable.

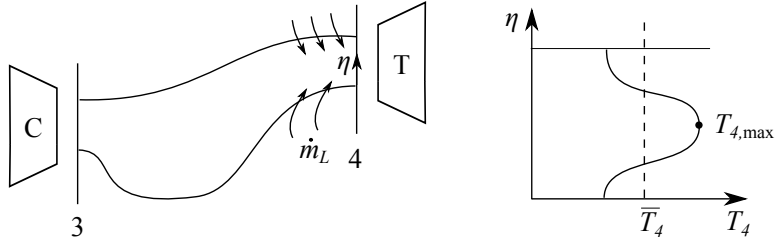


Figure 5.4: Definition of pattern factor.

General correlation for the pattern factor is $\text{PF} = f(\dot{m}_L, \Delta p)$, where Δp is the liner pressure-loss factor. A typical form is

$$\text{PF} \sim 1 - \exp \left(\frac{L_L}{D_L} \frac{\Delta p}{q_\infty} \right)^{-1}, \quad (5.14)$$

where L_L is the total liner length, D_L is the liner height, Δp is the pressure loss across the liner, and q_∞ is the dynamic pressure.

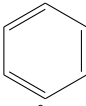
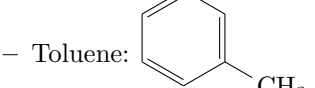
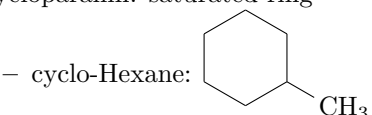
5.1.3. Aviation Fuels. Gas turbine combustors are relatively fuel-independent. Today's daily fuel consumption for aviation fuel is approximately 100 million gallons. However, kerosene was not always used as aviation fuel. For instance, the Wright brothers used standard oil motor gasolines. The Whittle engine used

kerosene instead of Diesel because of the lower freezing point of the kerosene. Von Ohain first considered hydrogen for engine demonstration and later switched to Avgas as aviation fuel.

The specification of aviation fuel is classified in the norm ASTM D1655, and includes conditions on: freezing point (relevant for high altitude operation); fuel volatility/vapor pressure (high altitude relight). To improve operability and stability of aviation fuels, additives are added to achieve certain properties, such as:

- Corrosion inhibitor;
- Fuel lubricants;
- Icing inhibitor: fuel system icing inhibitor;
- Inhibitor of growth of micro-organisms;
- Static dissipator additives to increase electric conductivity (reduce electro static discharge in flammable fuels): static dissipator additives;
- antioxidants to prevent formation of gums and peroxides;
- Thermal stability to enable regenerative cooling.

Typically, an aviation fuels considers of a large number of compounds. These compounds can be categorized into different classes:

- Normal paraffin: straight/linear alkane
 - n-Heptane: $\begin{array}{ccccccccc} & | & | & | & | & | & | \\ -C & - \\ | & | & | & | & | & | & | \end{array}$
- iso-Paraffin: branched alkane
 - iso-Octane: $\begin{array}{ccccc} & | & & | & \\ -C & - & C & - & \\ | & & | & & \\ -C & -C & -C & -C & - \\ | & | & | & | & \\ -C & & & & \end{array}$
- Olefine: double bond (reactive due to the double bond)
 - 1-Pentene: $\begin{array}{cccccc} & | & & | & & | \\ C & = & C & - & C & - C & - C \\ | & & | & & | & & | \end{array}$
- Aromatics:
 - Benzene: 
 - Toluene: 
- Cycloparaffin: saturated ring
 - cyclo-Hexane: 

Some of the most common aviation fuels are:

- Jet-A: standard commercial aviation fuel (similar to military JP-8);

- JP-4: USAF military fuel prior to JP-8 (replaced by JP-8);
- JP-5: NAVY-fuel, replaced by F-76 Diesel fuel;
- JP-7: USAF supersonic aircraft,
 - High flash point, thermal stability;
 - Poor relight capability;
 - SR-71;
- JP-8: main USAF fuel (Jet A + additives);
- JP-10: Missile-fuel.

The specifications and components of Jet A/A-1 and JP-8 fuels are listed in [Table 3](#).

Approximate formula	C ₁₁ H ₂₁
Boiling range	165°C – 265°C
Freeze point	-51°C – -45°C
Flash point	53°C
Critical temperature/pressure	410°C/23 atm
Average composition	Volume percent
Aromatics	18%
Naphtalenes	35%
Paraffins	45%
Olefins	2%

Table 3: Specifications and compositions of Jet A/A-1 and JP-8.

5.1.3.1. Non-petroleum and Alternative Fuels.

Synthetic fuel is the fuel made of CO + H₂ through the Fischer-Tropsch process. The merits of this fuel are clean burning, no sulfur and higher thermal stability. The disadvantages includes poor lubrication properties, lower volumetric heat content, lack of aromatics (reduces seal swell) and high energy consumption for production.

Biofuels are fuels made from biomass sources such as corn, grain, palm oil and algae. Though beneficial in replacing fossil fuel sources for hydrocarbon fuels, biofuels generally have disadvantages of low freeze point, poor high-temperature thermal stability and being supplied (mostly) from food production sources. Two widespread classes of biofuels used, bioethanol and biodiesel, are discussed here.

Bioethanol (also known as ethyl alcohol, with the chemical formula C₂H₆O) is produced from the yeast fermentation of food crops or other biomass sources – for example, cellulosic sources such as native grasses trees, sawdust, and waste paper. See [Fig. 5.5](#) for example schematics of bioethanol production concepts. Bioethanol is currently widely-used as an additive in gasolines, due to its advantage of increased octane number (108, versus the 88-100 that is typical of pure gasoline) as well as emissions reduction potential in vehicles. With current standards and regulations, any gasoline-powered U.S. engine can use E10 gasoline (with

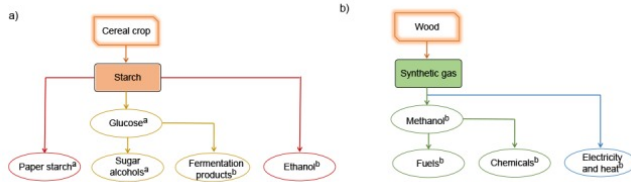


Figure 5.5: Examples of biorefinery concepts, for a) bottom-up and b) top-down designs. Superscript a refers to traditional products, and b refers to new products [20].

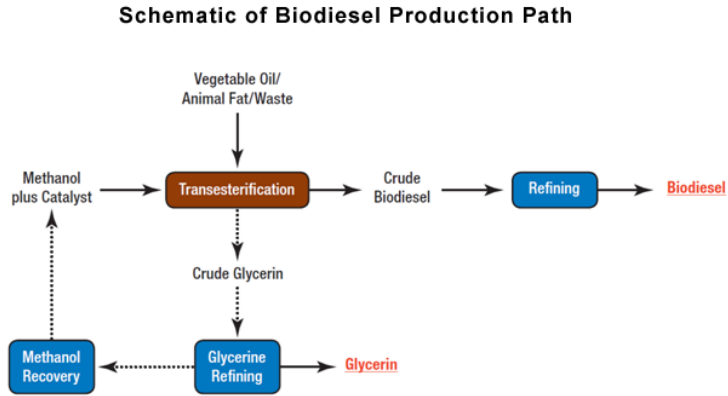


Figure 5.6: Example schematic for biodiesel production [21].

10% bioethanol), and cars and light trucks with model year 2007 and later are certified to use E15 (with 15% bioethanol). Higher bioethanol levels are limited to regional uses and require specially-certified engines (so-called flexible fuel vehicles). Bioethanol suffers from a number of downsides. Its hygroscopicity makes it corrosive to engine components. Pure ethanol is less-readily vaporizable than gasoline and thus can lead to engine startup problems in cold ambient temperatures. At lower ethanol concentrations in gasoline-ethanol mixes, higher evaporative emissions can be observed if proper processing is not done; these increased emissions contribute to the formation of ground-level ozone and smog. Ethanol also has different tribological behavior from gasoline, which thus affects engine component performance and wear. For further information on bioethanol, the reader is referred to [22].

A second class of biofuels is biodiesel, which is typically manufactured from vegetable oils, animal fats, or recycled cooking grease. See Fig. 5.6 for an example schematic of a biodiesel production concept. Note that the terms “renewable diesel” or “green diesel” refer to a renewable fuel that is also derived from the

same biomass sources as biodiesel but that is processed via hydrotreating and that chemically meets the ASTM D975 specification for petroleum diesel. Similarly to the E naming system for bioethanol fuels, biodiesel is named using BX, where X is the percentage of biodiesel, such that B100 refers to pure biodiesel. Biodiesel has a number of advantages over traditional petroleum diesels. Carbon life cycle analyses suggest that using B100 would reduce carbon dioxide emissions by 74% compared with petroleum diesel. Biodiesel has an improved cetane number and improved fuel lubricity (thus increasing engine performance and lifetimes), and its higher flashpoint makes it safer to human health and the environment. However, biodiesel suffers from a number of downsides; it experiences solidification/aggregation at low temperatures, it is usually significantly more expensive than traditional diesel, and (like ethanol) it introduces issues of engine component corrosion due to hygroscopicity. For further information on biodiesel, the reader is referred to [23].

The current fuel strategy is to use petroleum-based fuels such as Jet-A and JP-8. Near-term goals are the consideration of drop-in fuels with synthetic fuel. Mid-term solutions include the blend of synthetic and processed bio-fuels, requiring moderate changes in the engine configuration. Potential long-term goals are the consideration of hydrocarbon-free fuel sources.

5.1.4. Liquid Fuel Injection, Preparation and Combustion of Fuel. A main requirement in the combustor design is the fuel injection and fuel-preparation process. Several injector configurations for achieving rapid fuel break-up have been considered. These include (see Fig. 5.7):

- Simplex/duplex pressure atomizer;
- Air blast;
- Rotary (slinger);
- Simplex swirlers.

The processes of injection, preparation and combustion of the liquid fuel includes the following steps (see Fig. 5.8):

- Primary breakup of liquid fuel into liquid fragments and ligaments;
- Secondary breakup of liquid fragments into droplets;
- Vaporization of droplets;
- Mixing of gaseous fuel with air;
- Combustion of fuel/air mixtures;
- Post combustion and Pollutant formation.

General requirements for atomizers are:

- Provide good atomization over range of fuel flow rates;
- Rapid response to flow rate;
- No instabilities;
- Low power requirements, cost, weight, and maintenance;
- Uniform fuel distribution.

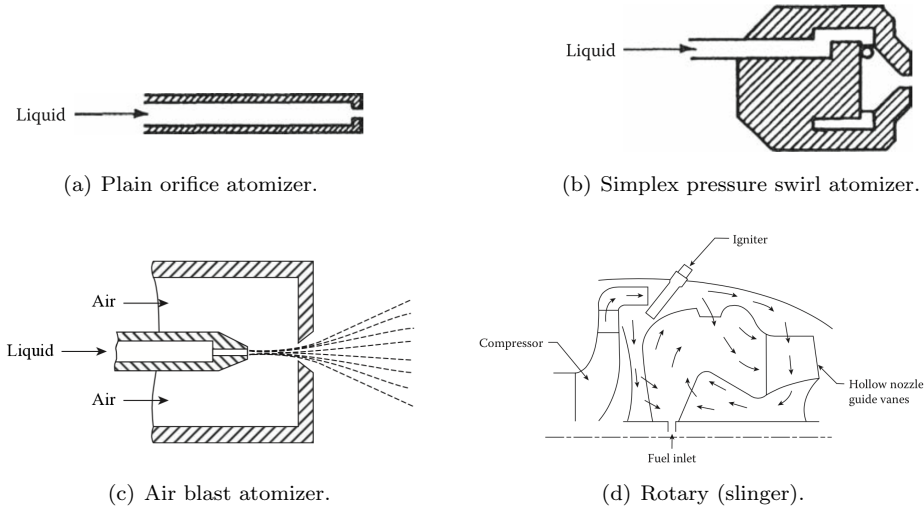


Figure 5.7: Examples of fuel injectors [8].

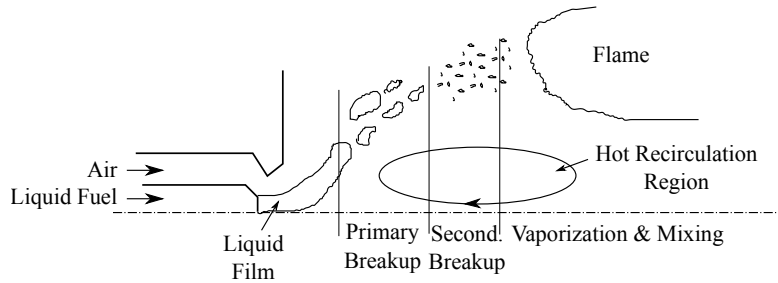


Figure 5.8: Air flow pattern in combustor.

5.1.4.1. Liquid Fuel Breakup and Droplet Formation. Characteristic parameter for droplet breakup is the Weber number (We, comparing inertia and surface tension forces). Consider force balance between the aerodynamic drag and the surface tension force as shown in Fig. 5.9, we have

$$F_D = F_\sigma,$$

with the drag force defined from the drag coefficient.

$$C_D = \frac{F_D}{\frac{1}{2} \rho_A U_A^2 S}$$

and the surface tension force follows from:

$$\sigma = \frac{F}{L} = \frac{F}{\pi D}.$$

With this, we can rewrite the force balance as:

$$\frac{1}{2} C_D \rho_A U_A^2 \frac{\pi}{4} D^2 = \pi D \sigma ,$$

which gives:

$$We_{\text{crit}} = \left(\frac{\rho_A U_A^2 D}{\sigma} \right)_{\text{crit}} = \frac{8}{C_D} . \quad (5.15)$$

Typical values for We_{crit} for low-viscosity fuels range from 1 to 12 in turbulent flows. With the critical Webber number, we can evaluate the maximum droplet size to be

$$D_{\max} = \frac{We_{\text{crit}} \sigma}{\rho_A U_A^2} . \quad (5.16)$$

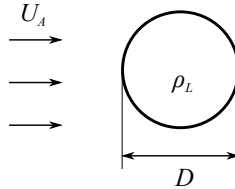


Figure 5.9: Droplet force balance.

5.1.4.2. Droplet Size Distribution. The breakup of the liquid fuel film results in a wide droplet distribution, consisting of droplets with different diameters. Fig. 5.10 schematically shows the droplet size distributions with different fuel line

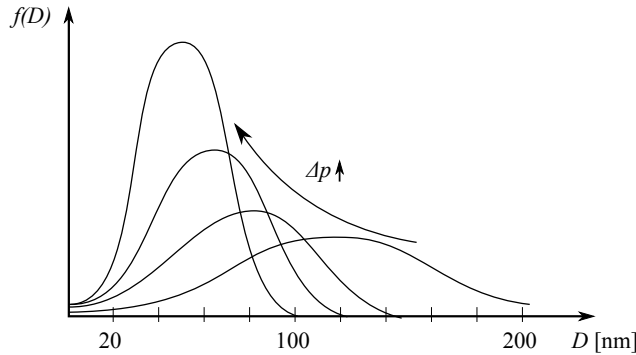


Figure 5.10: Droplet distribution of a pressure swirl atomizer.

pressure for a pressure swirl atomizer. This figure shows that with increasing fuel line pressure the droplet size reduces which is a favorable effect on emissions.

A model for the representation of the droplet distribution, $f(D)$, is the Rosin-Rammler distribution:

$$f(D) = 1 - \exp \left[- \left(\frac{D}{D_\sigma} \right)^\alpha \right], \quad (5.17)$$

where α is a distribution parameter and D_σ is the droplet size constant.

Another common parameter for the characterization of the spray distribution is the Sauter mean diameter (SMD). This quantity is the equivalent diameter equal to that of the volume-to-surface ratio of the entire spray relevant for vaporization and fuel conversion:

$$\text{SMD} \equiv D_{32} = 6 \frac{V_p}{A_p}. \quad (5.18)$$

with

$$A_p \simeq \pi D_s^2,$$

$$V_p \simeq \frac{\pi}{6} D_v^3,$$

where D_s and D_v are the equivalent surface and volume diameters, respectively. A commonly employed correlations for SMD is

$$\frac{D_{32}}{D} = C \text{Re}^\alpha \text{We}^{-\beta} \left(\frac{\mu_l}{\mu_g} \right)^\gamma \left(\frac{\rho_l}{\rho_g} \right)^\delta, \quad (5.19)$$

where $C, \alpha, \beta, \gamma, \delta$ are the fitting parameters.

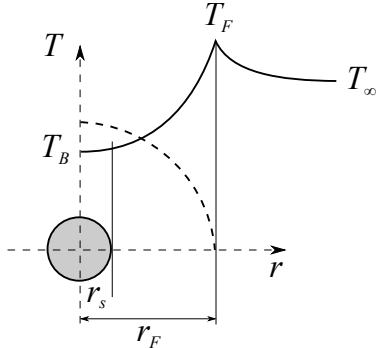


Figure 5.11: Droplet evaporation theory.

5.1.4.3. Drop Evaporation Theory. From the energy balance, the heat conduction from the gas to the droplet is equal to the energy of vaporization (see Fig. 5.11),

$$(4\pi r_s^2) \lambda_g \left. \frac{dT}{dr} \right|_{r=r_s} = \dot{m}_{\text{evap}} h_v, \quad (5.20)$$

where λ_g is the thermal conductivity of the gas, $4\pi r_s^2 = A_p$ is the droplet surface area, \dot{m}_{evap} is the mass flow rate of evaporated fuel, h_v is the heat of vaporization,

T_B is the boiling temperature of liquid fuel ($\simeq 170^\circ\text{C}$ for Jet-A), T_F is the flame temperature and T_∞ is the temperature of the surrounding air ($\simeq 700^\circ\text{C}$). We approximate the derivative of the temperature at the droplet surface as:

$$\left. \frac{dT}{dr} \right|_{r=r_s} \simeq \frac{T_F - T_B}{r_F},$$

where $r_F \simeq C_1 r_s$, and evaluate the evaporation mass flow rate as:

$$\dot{m}_{\text{evap}} = \frac{4\pi r_s \lambda_g}{C_1 c_p} \mathcal{B},$$

with $\mathcal{B} \equiv c_p(T_F - T_B)/h_v$. With

$$\dot{m}_{\text{evap}} = -\frac{dm_{\text{evap}}}{dt},$$

and $m_{\text{evap}} = \rho_L \frac{4}{3}\pi r_s^3$, we can integrate the equation in the following form

$$\int_{D_0/2}^0 r_s dr_s = - \int_0^{\tau_{\text{evap}}} \frac{\lambda_g}{c_p \rho_L C_1} \mathcal{B} dt,$$

hence we have

$$\frac{1}{8} D_0^2 = \frac{\lambda_g}{c_p \rho_L C_1} \mathcal{B} \tau_{\text{evap}},$$

and finally

$$\tau_{\text{evap}} = \frac{D_0^2}{\beta}, \quad \text{with} \quad \beta = \frac{8\lambda_g}{c_p \rho_L C_1} \frac{c_p(T_F - T_B)}{h_v} \quad (5.21)$$

where β defines the evaporation time coefficient, and D_0 is the initial droplet diameter.

By considering typical gas-turbine operating conditions with air as oxidizer and kerosene as fuel: $\lambda_g = 0.024 \text{ W}/(\text{m K})$, $\rho_L = 700 \text{ kg}/(\text{m}^3)$, $T_F = 2500 \text{ K}$, $T_B = 430 \text{ K}$, $C_1 \simeq 1$, $h_v = 251 \text{ kJ/kg}$, and $D_0 = 50\mu\text{m}$. Inserting these values into Eq. (5.21) results in an evaporation time of $\tau_{\text{evap}} \simeq 1 \text{ ms}$.

Note that this model assumes that combustion takes place in the so-called isolated droplet regime, meaning that each droplet is surrounded by a flame. This is typically only observed for droplets with large diameters, and the most common combustion regime observed in gas turbine combustors is the group combustion regime. The different regimes are a function of droplet density (number of droplets per area), droplet distribution, evaporation time, and surrounding environment.

5.1.4.4. Fuel and Air Mixing Theory. Shear layer instabilities cause the entrainment of air into the vaporized fuel and the liquid jet spreads due to the centrifugal forces that are introduced due to the initial swirl motion (see Fig. 5.12). Here we develop a model for the fuel/air jet mixing length using the following assumptions:

- At the end of the jet, the mixture becomes stoichiometric;
- $L_{\text{mix}} \simeq$ distance for mixing into stoichiometry;
- Assume that the entrainment velocity U_e (see Fig. 5.12(b)) is constant across the jet.

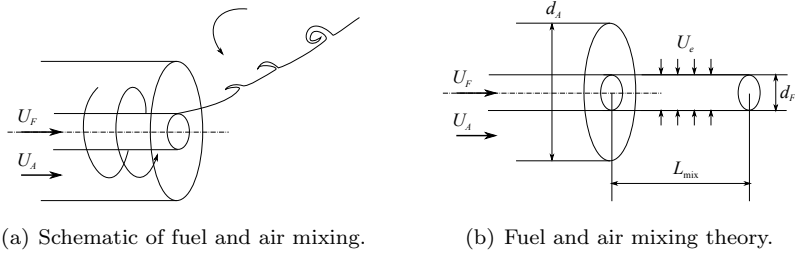


Figure 5.12: Problem description to describe the fuel/air mixing process.

The fuel/air ratio at stoichiometry is $f_{st} = \dot{m}_F/\dot{m}_A$. With $\dot{m} = \rho U A$, we can rewrite this ratio as:

$$\frac{\dot{m}_F}{\dot{m}_A} = \frac{\rho_F U_F \frac{\pi}{4} d_F^2}{\rho_A U_e \pi d_F L_{mix}}.$$

The entrainment velocity can be expressed using the empirical correlation

$$U_e = C_2 U_A \left(\frac{\rho_F}{\rho_A} \right)^{\frac{1}{2}} [1 + C_1 S_N]^{-1}, \quad (5.22)$$

where $S_N \simeq 0.7$ is the swirl number, which is the ratio of angular momentum flux to axial momentum flux. With this expression, we can estimate the mixing length as:

$$\frac{L_{mix}}{d_F} = \frac{1}{4C_2 f_{st}} \frac{1}{U_A} \left(\frac{\rho_F}{\rho_A} \right)^{\frac{1}{2}} [1 + C_1 S_N]^{-1} \frac{U_F}{U_A}, \quad (5.23)$$

showing that L_{mix} is dependent on swirl number and air velocity. Increasing the swirl number and/or surround air velocity reduces the mixing length, and thereby allows for a smaller combustor section.

5.1.4.5. Pressure-Swirl Atomization. Among the most common fuel injection devices in gas turbine engines is the pressure-swirl atomizer, also known as the simplex atomizer, shown in Fig 5.13. This design works by injecting liquid tangentially from a set of entry ports of diameter D_p into a cylindrical cavity of base diameter D_s , which reduces in diameter axially to the orifice of diameter d_o . Crucially, the liquid is introduced into the cavity with sufficient tangential velocity v so as to remain bound to the walls of the cylindrical cavity, resulting in the formation of a gaseous core of diameter d_c along the centerline of the atomizer. The liquid travels up the atomizer at axial velocity u and undergoes tangential acceleration due to the reduction in area with axial distance. The liquid exits the orifice as a thin liquid sheet which spreads into a cone of angle α , also known as the spreading angle, which then rapidly undergoes instability-driven breakup and disintegrates into droplets. Critical performance characteristics of this atomizer type are first discussed, after which the breakup of the liquid sheet and the associated droplet dynamics are introduced.

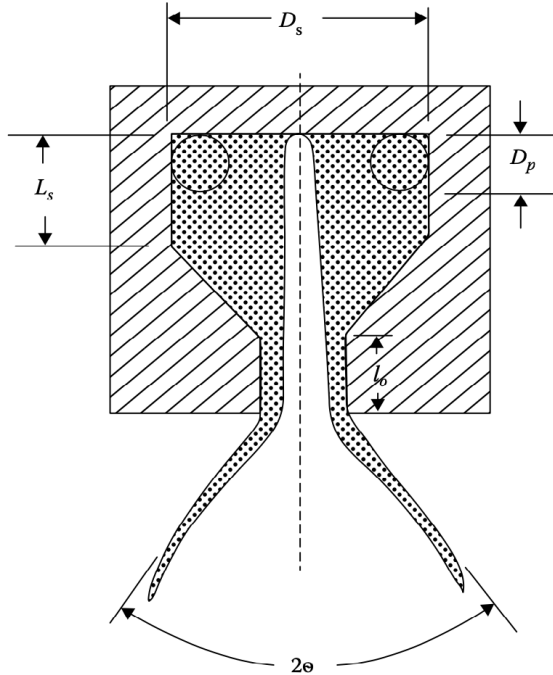


Figure 5.13: Detailed cross-section of a pressure swirl (simplex) atomizer [8]. The dotted area is the liquid, and the hatched area is the atomizer body.

Discharge Coefficient. The discharge coefficient C_D of a pressure-swirl atomizer is derived analytically in this section. This is a quantity of great significance in combustor design using any atomizer type, as it relates the desired liquid mass flow rate through the atomizer \dot{m}_F with the pressure differential across the atomizer required to achieve it $\Delta p_F = p_F - p_3$, where p_F is the pressure in the fuel manifold. The following derivation relies upon the assumption that the liquid is inviscid and invokes elements of perfect fluid theory. It is based on the original work of Taylor [24] and the subsequent refinement by Giffen and Muraszew [25].

Define the discharge coefficient C_D as [8]

$$C_D = \frac{\dot{m}_F}{A_o \sqrt{2\rho_F \Delta p_F}} \quad (5.24)$$

where $A_o = \frac{\pi}{4}d_o^2$ is the area of the discharge orifice. Invoking perfect fluid theory, we can describe the motion of the liquid inside the atomizer as that of a free vortex with a superimposed axial motion. Since the flow is inviscid, its tangential velocity is describable as $vr = v_p D_s / 2 = \text{const}$, where $v_p = Q/A_p$, Q is the flow rate into the atomizer and $A_p = \pi D_p^2 / 4$. Hence we have $v = \frac{Q D_s}{2 A_p r}$, from which it is immediately clear that there must be an ‘air core’ at the center of the nozzle, since otherwise as $r \rightarrow 0$ it would imply the tangential velocity of the liquid $v \rightarrow \infty$.

We consider now the Bernoulli equation for streamlines at any point within the liquid inside the atomizer's orifice section. It is important to consider the orifice, since in this section the diameter remains constant, resulting in no tangential acceleration and furthermore resulting in a radial velocity component $w = 0$. Noting that all fluid energy inside the atomizer must stem from the inlet pressure head, we obtain at any point in the liquid in this section

$$\frac{\Delta p}{\rho_F} + \frac{1}{2}u^2 + \frac{1}{2}v^2 = \text{const} = \frac{\Delta p_F}{\rho_F}, \quad (5.25)$$

where $\Delta p = p - p_3$ and p is the liquid pressure at the point considered. However, considering alone the motion of the free vortex inside the orifice, the fluid has no axial velocity component u , and hence satisfies $\frac{\Delta p}{\rho_F} + \frac{1}{2}v^2 = \text{const}$. From this it is deduced that within the liquid layer in the orifice, the axial velocity is constant: p and v will vary with distance from the centerline within the liquid, but u is constant. It follows that, for the liquid in the orifice,

$$u = Q/(A_0 - a_0), \quad (5.26)$$

where $a_0 = \pi d_{0,a}^2$ is the area of the air core in the orifice, and $d_{0,a}$ is the diameter of the air core in the orifice.

Now we consider again the Bernoulli equation in the liquid within the orifice section, but directly at the free surface where the liquid meets the air core. Neglecting surface tension effects, at this location the liquid pressure $p = p_3$ and hence

$$\frac{1}{2}u^2 + \frac{1}{2}v^2 = \frac{\Delta p_F}{\rho_F}. \quad (5.27)$$

Substituting for u and v from above,

$$\frac{1}{2} \left(\frac{Q}{\pi(d_0^2 - d_{0,a}^2)/4} \right)^2 + \frac{1}{2} \left(\frac{Q D_s}{A_p d_{0,a}} \right)^2 = \frac{\Delta p_F}{\rho_F}. \quad (5.28)$$

Noting that the discharge coefficient can be rewritten as $C_D = \frac{Q}{\frac{\pi}{4}d_0^2 \sqrt{2\Delta p_F/\rho_F}}$, with some rearrangement we obtain

$$\frac{1}{C_D^2} = \frac{1}{(1-X)^2} + \frac{1}{K^2 X^2}, \quad (5.29)$$

where $X = (d_{0,a}/d_0)^2$ and $K = D_p^2/(D_s d_0)$. It is clear that K is purely a function of the atomizer geometry, but X remains unclosed. Here, we invoke the perfect fluid analogy to the choked nozzle flow condition, which states that the size of the air core in the orifice will be such that the liquid flow rate is a maximum i.e. $1/C_D^2$ is minimized. For details, see the discussion in [24]. We enforce this condition as

$$\frac{d(1/C_D^2)}{dX} = \frac{2}{(1-X)^3} - \frac{1}{K^2 X^2} = 0, \quad (5.30)$$

which yields a quite unwieldly analytical solution, but is easily solved numerically to obtain K as a function of X , where evidently $0 \leq X \leq 1$. From this, C_D is obtained purely as a function of atomizer geometry through K , and this has been

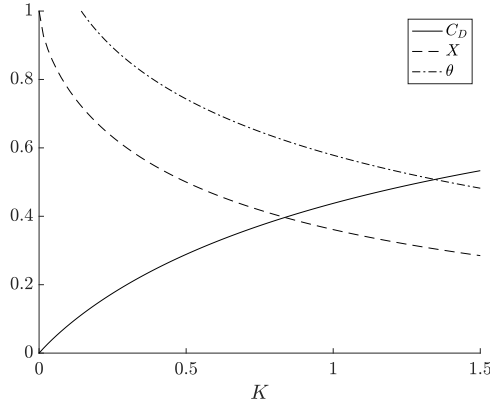


Figure 5.14: Variation of X , C_D and θ (in radians) with the geometric parameter K for pressure swirl atomizers.

plotted in Fig. 5.14. The figure shows that there is a diminishing rate of return in geometry modifications to achieve an improved discharge coefficient. Furthermore, there is a significantly detrimental effect in attempting to reduce d_0 to improve C_D . This is evident if it is considered that, from Fig. 5.14, $C_D \propto K^a$, $0 < a < 1$ and $K \propto d_0^{-1}$. Hence, from the definition of C_D , in order to maintain a constant flow rate Q , the pressure differential required to achieve that flow rate scales as

$$\Delta p_F \propto d_0^{2a-4}, \quad (5.31)$$

and $2a - 4 < 0$. Thus, although some improvement in discharge coefficient may be achieved in reducing orifice area, it still has an adverse effect of the necessary fuel pressure to achieve a given flow rate. This is of course a physically intuitive result: a more restricted orifice requires a greater pressure for the same flow rate.

Cone Angle. It was established above that the total fluid energy at any point in the liquid is equal to that imparted by the inflow pressure head. We may express this in terms of a velocity head $U = \sqrt{2\Delta p_F/\rho_F}$. Since inviscid flow is considered, the velocity magnitude of any fluid parcel exiting the atomizer is U . The task thus becomes finding one of the velocity components at the atomizer exit plane. We will assume that the back pressure remaining in the liquid at the exit plane is transferred entirely to the axial component of motion, and hence the estimated cone angle will be a theoretical minimum. Considering the tangential velocity and recalling that it was previously established that within the orifice u was constant at all radii in the liquid, we note that the mass flow rate through a ring-shaped fluid element of radial extent dr at a distance r from the centerline in the liquid within the orifice section is $2\pi r \rho_F u dr$. From above, the tangential velocity is $v = \frac{Q D_s}{2 A_p r}$, and hence the momentum flow through the ring per unit time is $\frac{\pi \rho_F u Q D_s dr}{A_p}$. Integrating this expression from the air core to the orifice wall gives the orifice total tangential momentum flow rate $\frac{\pi \rho_F u Q D_s (d_0 - d_{0,a})}{2 A_p}$. The

mass flow rate in the orifice is $\pi\rho_F u(d_0^2 - d_{0,a}^2)/4$, and the volumetric flow rate can be expressed as $Q = \pi C_D d_0^2 U/4$. Normalizing the orifice total tangential momentum flow rate by the mass flow rate gives, after some rearrangement, the mean tangential velocity as

$$\frac{\bar{v}}{U} = \frac{2C_D}{K(1 + \sqrt{X})}, \quad (5.32)$$

where X was shown to be expressed uniquely a function of the geometric parameter K above. Hence, the mean cone angle 2θ is

$$2\theta = 2 \arcsin(\bar{v}/U), \quad (5.33)$$

and is shown in Fig. 5.14 as a function of the geometry parameter K . The figure shows the important result that with all other parameters being equal, a reduction in the orifice diameter results in a reduction in the spray cone angle. It is important to note that the mean angle was considered here, but that the theory shows that there will in fact be a range of angles covered by the ejected spray as a result of the tangential velocity scaling with radius as $v \sim r^{-1}$.

Break-up Length. The Linear Instability Sheet Atomization [26] (LISA) model estimates the length scale of the primary atomization region. This is done by relating the length scale of the primary break-up to a characteristic velocity and time scale:

$$L_{\text{PBU}} = U_{\text{PBU}} \tau_{\text{PBU}} \quad (5.34)$$

The characteristic velocity, U_{PBU} , is taken to be the speed of the liquid sheet far downstream of the swirl:

$$U_{\text{PBU}}^2 = U_F^2 + U_r^2, \quad (5.35)$$

where U_F and U_r are the axial and radial velocities. Due to the conservation of angular momentum, the swirl velocity U_θ decreases quickly for large swirl angles, $\theta = \arctan(U_r/U_F)$, and hence, is not included in the definition of the characteristic velocity U_{PBU} . The characteristic velocity is found by assuming the that the pressure drop across the injector scales with the kinetic energy:

$$\begin{aligned} \frac{1}{2}\rho_F U_{\text{PBU}}^2 &= k_v \Delta p, \\ \Rightarrow U_{\text{PBU}} &= \sqrt{\frac{2k_v \Delta p}{\rho_F}} \end{aligned} \quad (5.36)$$

where k_v is an empirical constant determined to be approximately 0.7, but does depend on the injector geometry in general. The pressure drop across an injector is known from the reservoir pressure of the fuel and the pressure in the combustor, p_{04} .

The time scale, τ_{PBU} , is found by assuming a linear growth in an initial disturbance, η_0 , in the liquid sheet:

$$\begin{aligned} \frac{d\eta}{dt} &= \Omega\eta , \\ \implies \eta &= \eta_0 \exp(\Omega t) , \\ \implies \tau_{\text{PBU}} &= \frac{\log(\eta_{\text{PBU}}/\eta_0)}{\Omega} , \end{aligned} \quad (5.37)$$

where η_{PBU} is a postulated disturbance magnitude, which leads to the break up of the liquid sheet. The log ratio of the break up disturbance to the initial disturbance is set to be $\log(\eta_{\text{PBU}}/\eta_0) = 12$. The maximum growth rate, Ω , is determined from a linear instability analysis on the thin film sheet. The details of this analysis are beyond the scope of this text but may be found in Senecal *et al.* [27]. The key result is the dispersion relation relating the disturbance wavenumber of the liquid sheet, k , to the growth rate, ω :

$$\omega = -2\nu_F k^2 + \sqrt{4\nu_F^2 k^4 + \frac{\rho_A}{\rho_F} U_{\text{PBU}}^2 k^2 - \frac{\sigma k^3}{\rho_F}}, \quad (5.38)$$

where ν_F is the kinematic viscosity of the fuel, and σ is the surface tension. Furthermore, the maximum growth rate is found by maximizing Eq. (5.38) (i.e., $\Omega = \max_k \omega(k; \nu_F, \rho_A, \rho_F, U_{\text{PBU}}, \sigma)$). Hence, the length scale of the primary break up region may be estimated with known pressure drops, empirical constants, and fuel properties.

5.1.4.6. Secondary Break up: The Taylor Analogy Break up Model. Subsequent to the primary atomization, individual droplets are formed which oscillate equatorially. The magnitude of this oscillation is proposed to be the means for which a secondary break up occurs. The dynamics are described according to the Taylor Analogy Break up Model (TAB) [28], where a forced-spring-mass-damper system is used:

$$F = m\ddot{x} + b\dot{x} + kx \quad (5.39)$$

In accordance to the Taylor analogy, the applied force, F , is taken to be the drag on the particle given by:

$$\frac{F}{m} = C_F \frac{\rho_A U_{\text{rel}}^2}{\rho_F r_0} \quad (5.40)$$

where x is the displacement of the equatorial extent of the droplet from the initial radius, r_0 , and U_{rel} is the relative velocity between the gas and the particle. The drag coefficient $C_F = 1/3$ is found by matching the critical Weber number found in experiment.

For the oscillating droplet, the damping coefficient is related to the viscosity of the droplet:

$$\frac{b}{m} = C_b \frac{\nu_F}{r_0^2}, \quad (5.41)$$

where $C_b = 5$ is the damping coefficient and is found in a similar manner to C_F .

Finally in this system, the surface tension within the droplet acts as the restorative force:

$$\frac{k}{m} = C_k \frac{\sigma}{\rho_F r_0^3}, \quad (5.42)$$

where $C_k = 8$. Furthermore for the fundamental mode of the droplet, the amplitude of the polar oscillation is twice that of the equatorial oscillation. Hence,

$$x_{\text{crit}} = \frac{r_0}{2}, \quad (5.43)$$

where x_{crit} is the critical equatorial displacement at which break up occurs. Now the dynamics of secondary break-up are fully described.

5.1.5. Length of Combustor. By combining the characteristics properties that describe evaporation, mixing and combustion, we can estimate a characteristic length of the combustor:

$$L_{\text{comb}} = L_{\text{evap}} + L_{\text{mix}} + L_{\text{dilute}}, \quad (5.44)$$

where L_{comb} is the combustor length, L_{evap} is the length to evaporate all droplets, L_{mix} is the length to mix the fuel and air and L_{dilute} is the length to dilute and reduce the temperature. Each individual length can be estimated using the corresponding characteristic time scale:

$$L_{\text{evap}} \simeq \bar{U} \tau_{\text{evap}},$$

$$L_{\text{mix}} \simeq \bar{U} \tau_{\text{mix}},$$

$$L_{\text{dilute}} \simeq \bar{U} \tau_{\text{dilute}}.$$

5.1.6. Emissions of Pollutant, Noise and Soot. Environmental concerns of emissions by gas turbines are listed in [Table 4](#). Reaction products of H_2O , CO_2 are not considered pollutants since they are a natural consequence of complete combustion. However, they do contribute to global warming as greenhouse gases (GHGs).

Pollutants	Impact
Carbon Monoxide (CO)	Toxic
Unburned Hydrocarbons	Toxic (photochemical smog)
Particulate Matter (Soot)	Visible (radiation)
Oxides of Nitrogen (NO_x)	Toxic, precursor of chemical smog, none depletion in stratosphere, acid rain
Oxides of Sulfur (SO_x)	Toxic, corrosive

Table 4: Principle emissions from gas turbines.

5.1.6.1. Aircraft Regulations.

Aircraft regulations are regulations by the International Civil Aviation Organization (ICAO). Emission regulations are commonly specified for a LTO-cycle, which includes the landing and take-off; these regulations are specific for engine type and thrust level, and are given in the form:

$$\text{Emission} = \frac{\text{Emission Index}}{[\text{g}/\text{kN}]} \times \frac{\text{Engine SFC}}{[\text{g}/\text{kg}_{\text{Fuel}}]} \times \frac{\text{Time in mode}}{[\text{kg}_{\text{Fuel}}/(\text{hr kN})]} \quad (5.45)$$

The ICAO standards for the turbofan/jet engines with take-off thrust with $T > 26.7 \text{ kN}$ are listed in [Table 5](#).

Emissions	Subsonic [g/kN]	Supersonic [g/kN]
UHC	19.6	$140(0.92)^{\pi_{00}}$
CO	118	$4550\pi_{00}^{-1.03}$
NO _x	$32+1.6\pi_{00}$	$36+2.42\pi_{00}$

Table 5: ICAO emission regulation [g/kN] for takeoff thrust $> 26.7 \text{ kN}$.

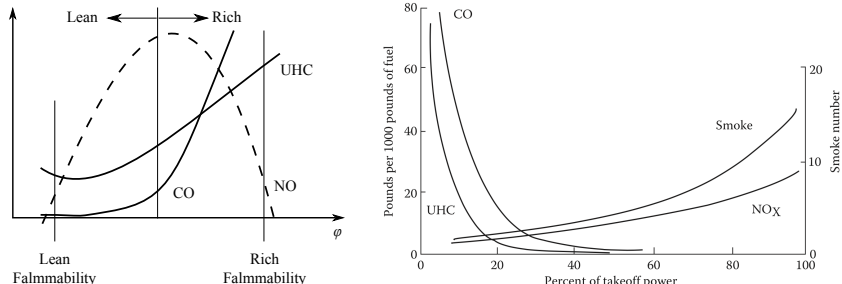
The NO_x emission index (EINO_x) is defined as

$$\text{EINO}_x = \frac{\dot{m}_{\text{NO}_x}}{\dot{m}_F} = \frac{\text{g/s NO}_x}{\text{kg/s Fuel}}. \quad (5.46)$$

The (thrust) specific NO_x level (SPNO_x) is defined as

$$\text{SPNO}_x = \frac{\dot{m}_{\text{NO}_x}}{T} = \frac{\text{g/s NO}_x}{kN}. \quad (5.47)$$

5.1.6.2. *Mechanisms for Pollutant Formation.* Emission formation is dependent on i) the equivalence ratio, and ii) the pressure (take off-power), which are depicted in [Fig. 5.15](#).



(a) Dependence of emission on equivalence ratio.
(b) Dependence of emission on take-off power level.

Figure 5.15: Emissions characteristics of gas turbine [8].

CO-Emissions. Fuel rich combustion leads to the formation of CO due to the lack of oxygen and incomplete combustion. At high temperature condition CO_2 dissociates into CO. At these conditions, emissions of CO exceed the equilibrium predictions, and sources of CO due to incomplete fuel combustion include:

- Inadequate burning rates due to insufficient residence time;
- Incomplete mixing;
- Quenching of flame.

The two main reaction for the oxidation of CO are:



and effects of the equivalence ratio and pressure on the CO-emission are shown in Fig. 5.16.

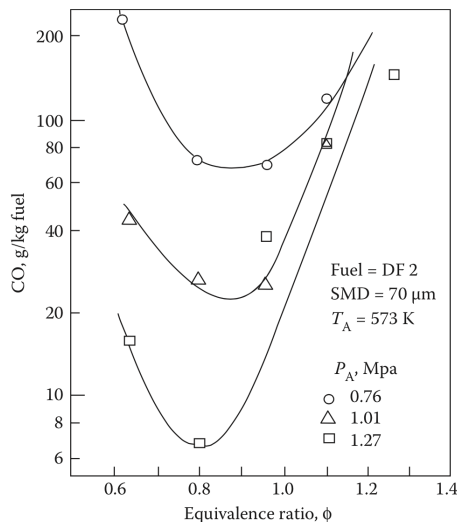


Figure 5.16: Influence of equivalence ratio and pressure on CO [8].

Common for gas-turbine combustor design is to work with correlations that provide a first-order estimate of the emission to essential operating conditions and geometric combustor dimensions. One of such correlation for the CO-formation in the primary combustion zone is given as:

$$\text{CO[g/kg}_{\text{Fuel}]\text{ = }} \frac{86\dot{m}_A T_{\text{st}} \exp\{-0.00345T_{\text{st}}\}}{(V_c - V_e) \left(\frac{\Delta p_c}{p_c}\right)^{0.5} p_c^{1.5}}, \quad (5.48)$$

where p_c is the pressure in combustor, Δp_c is the pressure drop (typically $\mathcal{O}(5)\%$), V_c is the combustor volume, T_{st} is the stoichiometric temperature, \dot{m}_A is the mass flow rate of air, and $V_e \sim D_p^3$, with D_p being the droplet diameter.

Note that correlations of the form of Eq. (5.48) are often specific to certain engine designs and manufacturers. While they provide useful estimates to capture essential emission trends, they exhibit limitations in applications to new engine concepts and the description of fundamental physical processes.

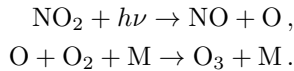
Unburned Hydrocarbons (UHC). Unburned hydrocarbons refer to unburned fuel (fuel vapor, drops, spray) or partially dissociated fuel products due to poor fuel atomization and inadequate burning rate.

Smoke/Soot. Soot production path way:

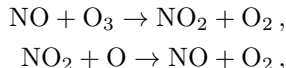
- Fuel → Dissociation, pyrolysis, oxidation
- Formation of precursor species
- Particle inception
- Surface growth and particle agglomeration
- Particle oxidation .

Due to the fuel-rich environment in RQL-combustors, soot is primarily formed in the primary reaction zone, and subsequently oxidized as it passes through the fuel-lean secondary zone.

Oxides of Nitrogen. Less than 3% of the global NO_x-emission arise from aircrafts. However, while small these emissions are particular harmful since they are main contributors to the ground-level ozone production (for < 12 km) via photochemical smoke:



Responsible for the stratosphere ozone depletion (supersonic flight, > 12 km) is the reaction pathway:

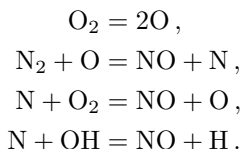


where NO produced in the second reaction step is recycled and acts as a reactant in the first reaction so that the overall reaction is: O₃ + O = 2O₂.

Other relevant NO-formation mechanisms include:

- Thermal NO (most relevant);
- Prompt NO;
- Nitrous Oxide mechanism;
- Fuel NO.

The thermal NO (or Zeldovich) mechanisms is described by the following reaction sequence:

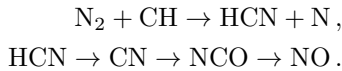


For thermal NO, no peak formation at the fuel-lean side occurs due to competition between fuel and nitrogen for available oxygen. However, the thermal NO-mechanism exhibits an exponential dependence on flame temperature as a result of the exothermic reaction of the O₂-oxidation. Key points for thermal NO formation:

- Thermal NO formation controlled by flame temperature;
- No significant NO formation below $T = 1850$ K;
- NO emission increases linearly with time, the characteristic time-scale is estimated as:

$$t \simeq \frac{1}{k[\text{O}_2]} \quad \text{from QSS.} \quad (5.49)$$

Relevant reactions for prompt NO:



The accurate description of NO-emissions requires detailed simulations, which remain computationally expensive. For practical applications, we often rely on empirical correlations that are written in general form:

$$\text{NO[g/kg}_{\text{Fuel}}] \sim C_1 p_c^\alpha V_c^\beta \exp\{C_2 T_{\text{st}}\} \dot{m}_A^\gamma T_{\text{st}}, \quad (5.50)$$

where α , β , γ , C_1 , and C_2 are fitting coefficients (specific to certain engine). An example of a specific correlation for NO-formation is:

$$\text{NO[g/kg}_{\text{Fuel}}] = 9 \times 10^{-8} p_c^{1.24} V_c \exp\{0.01 T_{\text{st}}\} \frac{1}{\dot{m}_A T_{\text{st}}}. \quad (5.51)$$

which has been developed for GE J79 and F101 engines.

Note that correlations (Eqs. (5.48), (5.50) and (5.51)) are specific to certain engine types, and this method is not predictive for new combustion concepts.

5.1.7. Advanced Combustor Technology. Design improvements of conventional combustor systems are to

- Improve emission;
- Increase combustion/flame stability;
- Increase mixture homogeneity;
- Reduce combustor size.

Temperature-controlled combustion. Temperature plays a primary role in the emission formation. Conventional combustors exhibit a wide range of temperature conditions between 1000 and 2500 K at low and high-power conditions. Effects of temperature on the emissions are illustrated in Fig. 5.17. Currently, the primary objectives are to reduce emissions by operating over a narrow temperature range (~ 1700 K – 1900 K) to reduce emissions below 5 ppmv CO and 15 ppmv NO_x; to maintain combustion zones within narrow temperature-range over the entire engine power range.

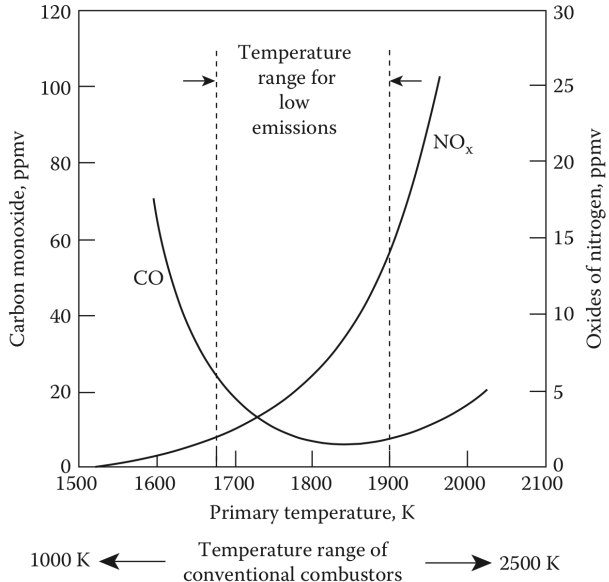


Figure 5.17: Influence of primary-zone temperature on CO and NO_x emissions [8].

5.2. Turbomachinery

Here, we will analyze compressor and turbine, both of which components can be treated using the same tools so that we will develop the theory by considering a compressor. Refer to Fig. 5.18 to remind yourself of the different components of gas turbine.

Main questions that we will consider are:

- Flow physics in turbomachineries;
- Efficiencies and losses;
- Analysis:
 - Velocity triangle;
 - Compressor map.

5.2.1. Flow Physics of Fan and Compressor. The compressor/fan raises the pressure of working fluid. For high bypass ratio turbofan, $\dot{m}_{\text{fan}} \sim 1 \text{ t/s}$, which corresponds to 75% of the engine thrust generation. Compression ratio can be as high as 50:1, $T_{03} \sim 700^\circ\text{C}$. Analysis of turbomachinery requires

- Aerodynamics;
- Noise;
- Mechanics;
- Manufacturing;
- Cost.

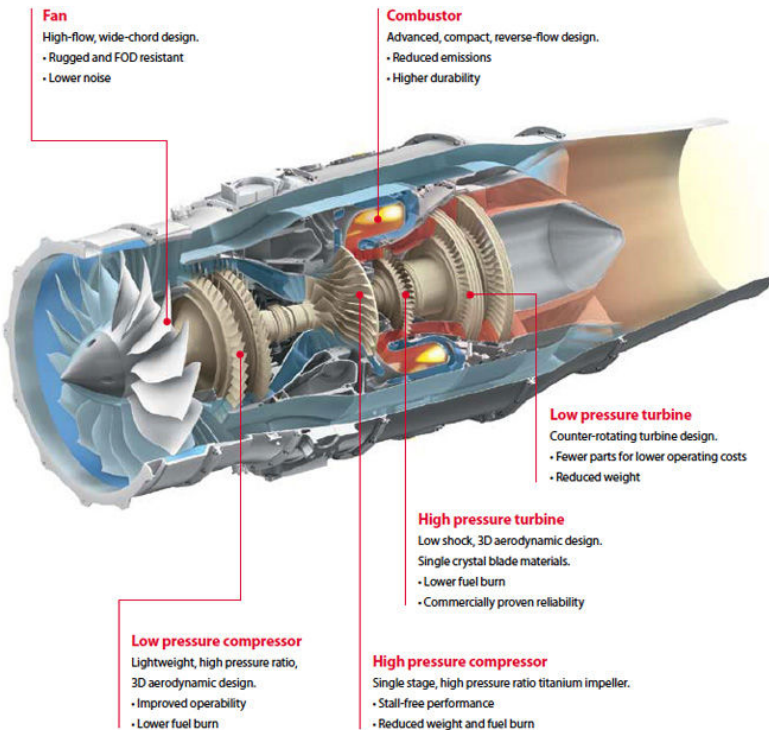


Figure 5.18: GE Honda HF120 turbofan engine (see <http://world.honda.com/HondaJet/Background/TurbofanEngine/>).

Optimal turbomachinery design is obtained from trade-study.

Our objectives are

- Perform component analysis of compressor stage;
- Derive relation between geometry, pressure increase and work input;
- Link flow kinetics to technical work.

There are three common compressor designs:

- Axial:
 - Most common for large engine;
 - combination of states to achieve specific pressure ratio.
- Centrifugal:
 - Limited pressure ratio (restricted to small engines).
- Axi-centrifugal:
 - Combination of axial and centrifugal compressor (Honda Jet).

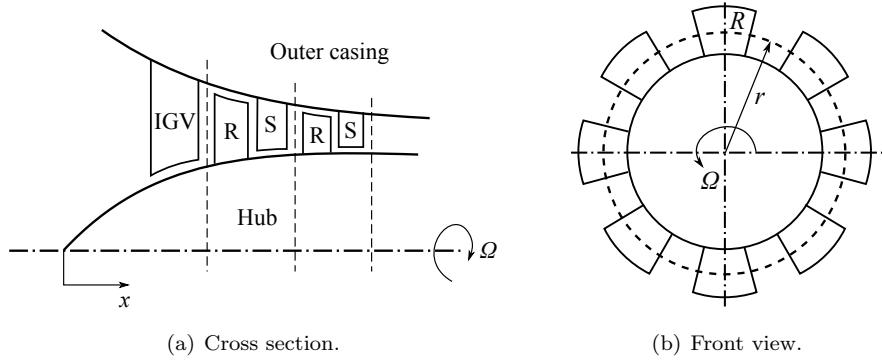


Figure 5.19: Cross section and front view of a typical axial compressor.

Due to the limitation on pressure raise given by flow-separation (adverse pressure gradient), we use multiple stages to facilitate the overall compression ratio. See Fig. 5.19(b), where IGV is short for inlet guide vane which straightens flow from compressor to be stationary w.r.t. the rotating hub, R is short for the rotor (rotates with the hub), and S is short for stator (stationary with the casing). Each R-S pair is a “compressor state”. Cross-sectional area changes through compressor. This is done to achieve constant axial velocity (raising hub, falling casing),

$$\frac{\dot{m}}{U} = \text{constant} = \rho A \quad \text{and} \quad \gamma \frac{dp}{\rho} = \frac{dp}{p}.$$

5.2.1.1. Work of Compressor Stage and Velocity Triangle.

Consider flow field around rotor-stator (see Fig. 5.20), we introduce the following terminology:

- $V_B = r\Omega$: azimuthal velocity of rotor (blade velocity);
- U : fluid velocity approaching blade in fixed coordinate frame (absolute velocity);
- W : fluid velocity relative to rotating blade (relative velocity);
- α : absolute angle of attack;
- β : relative approach angle.

As result of pressure force on blade surface, angular momentum changes as fluid travels through stage. The questions we want to ask are i) what is $\Delta p = p_c - p_a$? ii) what is w_{tac} (the technical work)?

To answer these questions, we perform a kinematic analysis around the rotor and stator (see Fig. 5.21). From kinematic relation, we have

$$W + V_B = U.$$

We can now reduce both velocity triangles to find the difference in azimuthal velocity, which determines torque and power requirements of engine.

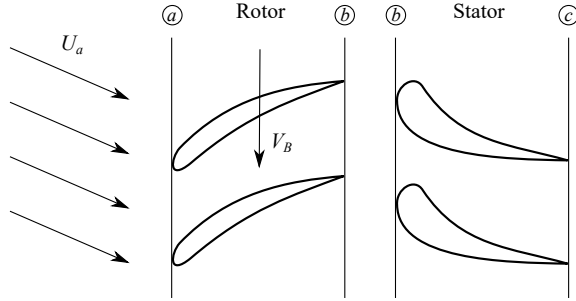
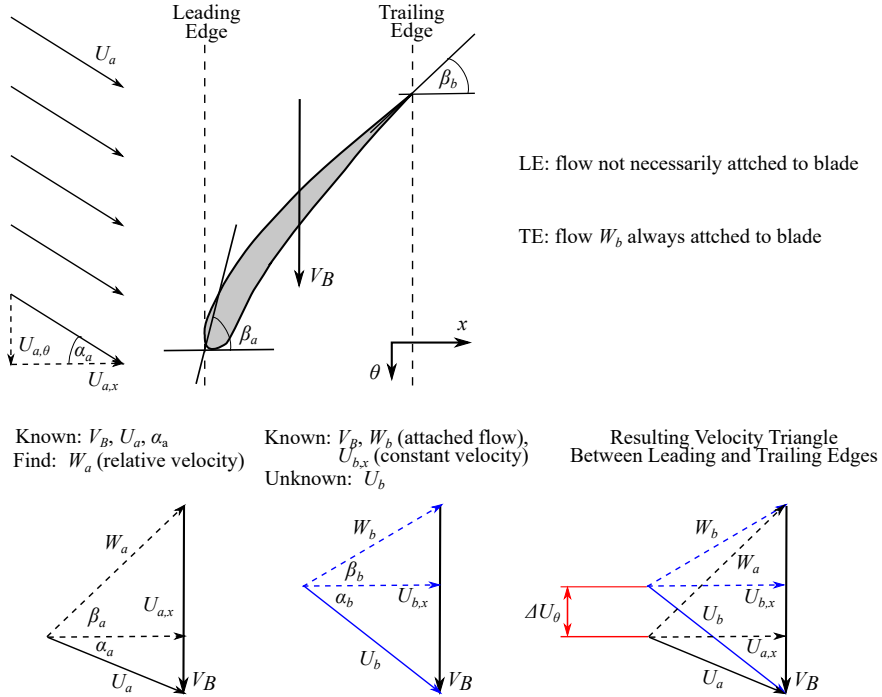
Figure 5.20: Azimuthal cut at radius r through stage.

Figure 5.21: Velocity triangle.

Increase in azimuthal velocity will result in torque. Consider torque in azimuthal direction in the control mass as shown in Fig. 5.22(a):

$$T = rF_\theta = \delta m \frac{d}{dt}(rU_\theta), \quad (5.52)$$

then the total torque is obtained by converting control mass into control volume

$$T_{\text{total}} = \frac{d}{dt} \int_{\text{CV}} \rho r U_\theta dV + \int_{\text{CS}} \rho r U_\theta (\mathbf{U} \cdot \mathbf{n}) dA. \quad (5.53)$$

With the time-dependent part neglected for steady state, we have

$$T_{\text{total}} = \int_{\text{CS}} \rho r U_\theta (\mathbf{U} \cdot \mathbf{n}) dA. \quad (5.54)$$

Since the velocity on the blade wall is always V_B (see Fig. 5.22(b)), so we have

$$T_{\text{total}} = \int_{A_b} (rU_\theta) \rho U_n dA - \int_{A_a} (rU_\theta) \rho U_n dA. \quad (5.55)$$

For the special case of constant (rU_θ) at each area (free vortex flow), we have

$$T_{\text{total}} = \dot{m}[(rU_\theta)_b - (rU_\theta)_a] [\text{N} \cdot \text{m}], \quad (5.56)$$

$$T_{\text{total}} = \dot{m}r\Delta U_\theta. \quad (5.57)$$

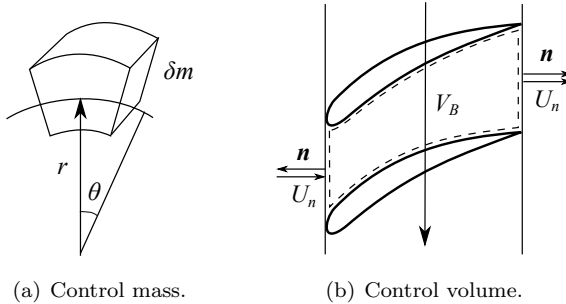


Figure 5.22: Control mass and control volume.

Work/Power of Compressor Stage. From Eq. (5.57), we have the total power

$$P_{\text{total}} = T_{\text{total}}\Omega = T_{\text{total}} \frac{V_B}{r} = \dot{m}V_B\Delta U_\theta. \quad (5.58)$$

Therefore, we have the work done by the compressor stage

$$P_C = -\dot{m}V_B\Delta U_\theta, \quad (5.59)$$

$$w_C = V_B\Delta U_\theta \quad (\text{specific work}). \quad (5.60)$$

Stage Pressure Ratio. Compute Δp across the stage. With the compressor work Eq. (5.60) and the first law

$$\begin{aligned} dh &= w_C = V_B\Delta U_\theta, \\ h_{0b} - h_{0a} &= V_B(U_{0b} - U_{0a}) = V_B\Delta U_\theta, \\ \frac{T_{0b} - T_{0a}}{T_{0a}} &= \frac{V_B\Delta U_\theta}{c_p T_{0a}}. \end{aligned}$$

By assuming adiabatic flow across stator $T_{0c} = T_{0b}$ (no work extraction from stator).

5.2.1.2. Characteristic Performance of Single Compressor Stage.

Consider single compressor stage (see Fig. 5.23). From velocity triangle:

$$\begin{aligned} U_{b,\theta} &= V_B - U_x \tan \beta_b \\ U_{a,\theta} &= U_x \tan \alpha_a \end{aligned}, \quad (5.61)$$

and from energy balance,

$$\begin{aligned} h_{0b} - h_{0a} &= V_B \Delta U_\theta = V_B (U_{b,\theta} - U_{a,\theta}) \\ &= V_B [V_B - U_x (\tan \beta_b + \tan \alpha_a)]. \end{aligned} \quad (5.62)$$

Normalized azimuthal velocity increment

$$\frac{\Delta U_\theta}{V_B} = \frac{h_{0b} - h_{0a}}{V_B^2} = 1 - \frac{U_x}{V_B} (\tan \beta_b + \tan \alpha_a). \quad (5.63)$$

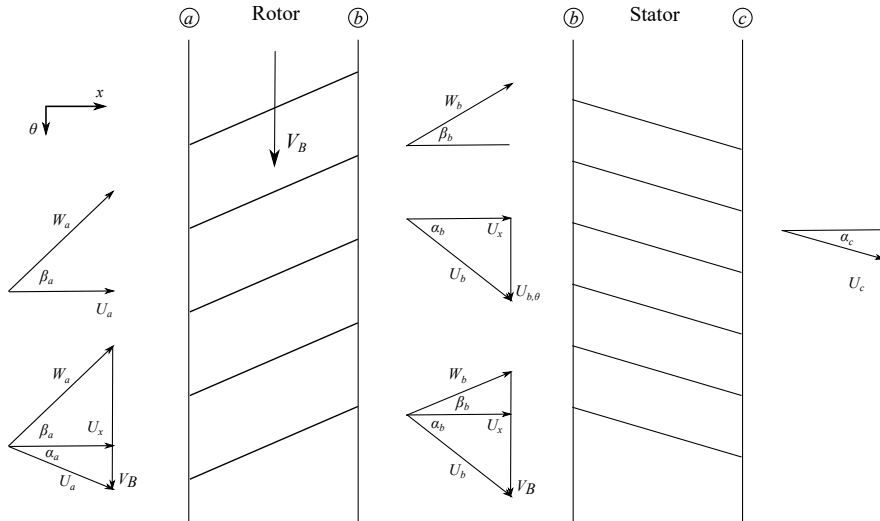


Figure 5.23: Single compressor stage.

We have two remarks:

- Changes in flow rate affect
 - Axial velocity;
 - Relative approach angle β_a .
- Changes in engine speed affect blade speed V_B .

One common assumption is that β_b (outflow angle) remains constant and not affected by changes in operating conditions, so we have

$$\tan \alpha_a + \tan \beta_b \equiv e \simeq \text{constant}, \quad (5.64)$$

$$\frac{\Delta U_\theta}{V_B} = \frac{h_{0b} - h_{0a}}{V_B^2} = \frac{h_0}{V_B^2} = 1 - \frac{U_x}{V_B} e, \quad (5.65)$$

which is called the ideal stage characteristics.

Stage efficiency is defined as

$$\eta_{st} = \frac{h_{0cs} - h_{0a}}{h_{0c} - h_{0a}}. \quad (5.66)$$

So we have

$$\frac{T_{0cs}}{T_{0a}} = 1 + \eta_{st} \left(\frac{T_{0c} - T_{0a}}{T_{0a}} \right) = 1 + \eta_{st} \left(\frac{V_B \Delta U_\theta}{c_p T_{0a}} \right), \quad (5.67)$$

with isentropic compression

$$\frac{p_{0c}}{p_{0a}} = \frac{p_{0cs}}{p_{0a}} = \left[1 + \eta_{st} \left(\frac{V_B \Delta U_\theta}{c_p T_{0a}} \right) \right]^{\frac{\gamma}{\gamma-1}}. \quad (5.68)$$

In general, we want p_{0c}/p_{0a} stage pressure ratio to be as large as possible to minimize number of stages required for given over pressure ratio (OPR), but if p_{0c}/p_{0a} is too large η_{st} becomes unacceptably low (due to flow separation).

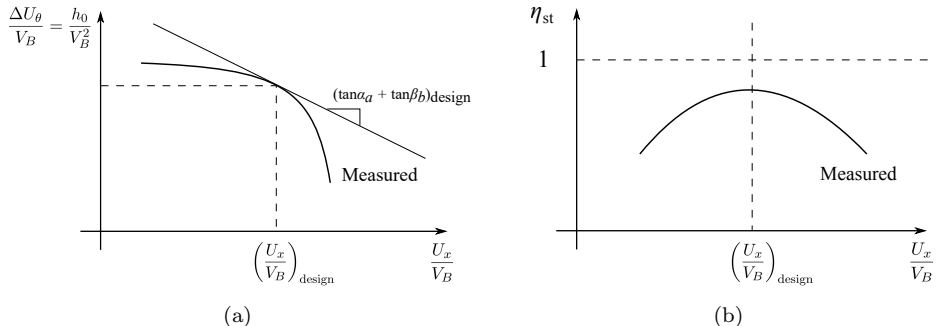


Figure 5.24: Ideal stage characteristics.

Fig. 5.25 shows changes in performance due to change in approach angle. Any deviation from design point leads to reduction in efficiency (stage efficiency drops). The implication for multi-stage compressor is that any departure from design point at entrance causes progressively increasing departure from design condition through the compressor. For example, at stage a, reduced U_x will cause

- More work on fluid;
- Higher density;
- Reduced U_x at stage b, ...

Most extreme engine mismatch between front and back stage during engine start-up (see **Fig. 5.26**). During startup, the engine has low compression ratio and $\rho_{0c}/\rho_c \approx 1$. Low U_x in first stage due to the initially low compression ratio. Compression remains small so that U_x increases due to constant work addition. This may result in engine choking! Operation at below-design-density-ratio causes variations in U_x that tend to overload leading stage, causing stall and improper compression.

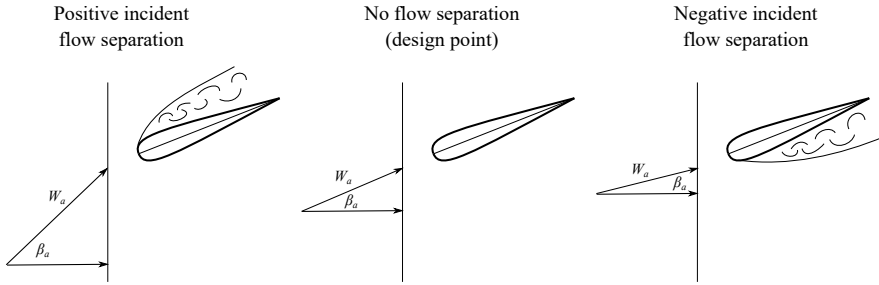


Figure 5.25: Changes in performance due to change in approach angle (constant absolute approach angle α_a).

Solutions for self-starting high pressure compressors:

- Air blast augmentation to increase U_x ;
- Blade speed variation not useful since different speeds for stages are needed
 - Blow-off valve to bypass air the second half of "bleed-port".
- Use of multi-spool compressor to drive LPC and HPC at different speed;
- Variable blade angle.

Recall stage pressure

$$\frac{p_{0c}}{p_{0a}} = \left[1 + \eta_{st} \frac{V_B^2}{c_p T_{0a}} \frac{\Delta U_\theta}{V_B} \right]^{\frac{\gamma}{\gamma-1}} = \left[1 + \eta_{st} \left(\frac{V_B}{\sqrt{\gamma R T_{0a}}} \right) \frac{\Delta U_\theta}{V_B} \right]^{\frac{\gamma}{\gamma-1}},$$

where $M_{BS} = \frac{V_B}{\sqrt{\gamma R T_{01}}}$ is the blade-speed Mach number.

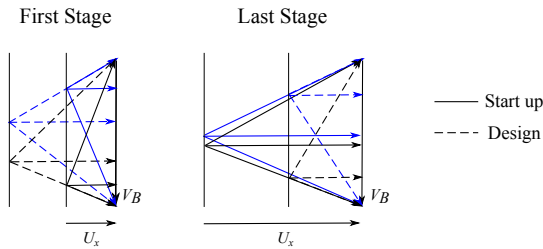


Figure 5.26: Velocity triangles at first and last stages.

5.2.1.3. Characteristic Performance of Multistage Axial Compressor.

See Fig. 5.27, where the overall stagnation pressure ratio is defined as p_{02}/p_{01} and the overall adiabatic efficiency is defined as

$$\eta_C = \frac{h_{02s} - h_{01}}{h_{02} - h_{01}}. \quad (5.69)$$

The dependence of the pressure ratio and efficiency on operating conditions is

$$\left(\frac{p_{02}}{p_{01}}; \eta_C \right) = f(\dot{m}, p_{01}, T_{01}, \Omega, \gamma, R, \nu, D),$$

where ν is the viscosity and D is the engine diameter. It can also be expressed in nondimensional parameters:

$$\left(\frac{p_{02}}{p_{01}}; \eta_C \right) = f\left(\underbrace{\frac{\dot{m}\sqrt{\gamma RT_{01}}}{p_{01}D^2}}_{\text{Momentum Pressure force}}, \underbrace{\frac{\Omega D}{\sqrt{\gamma RT_{01}}}}_{\text{Mach number}}, \underbrace{\frac{\Omega D^2}{\gamma}}_{\text{Reynolds number}}\right),$$

where . Since Reynolds number is not relevant, we have

$$\left(\frac{p_{02}}{p_{01}}; \eta_C \right) = f\left(\frac{\dot{m}\sqrt{\gamma RT_{01}}}{p_{01}D^2}, \frac{\Omega D}{\sqrt{\gamma RT_{01}}}\right). \quad (5.70)$$

A more common parameterization is obtained by introducing the non-dimensional temperature and pressure:

$$\Theta = \frac{T_{01}}{T_{\text{std}}}, \quad T_{\text{std}} = 288.15 \text{ K}, \quad (5.71)$$

$$\delta = \frac{p_{01}}{p_{\text{std}}}, \quad p_{\text{std}} = 101325 \text{ Pa}, \quad (5.72)$$

and we have

$$\left(\frac{p_{02}}{p_{01}}; \eta_C \right) = f\left(\frac{\dot{m}\sqrt{\Theta}}{\delta}, \frac{N}{\sqrt{\Theta}}\right), \quad (5.73)$$

where N is the shaft speed (RPM).

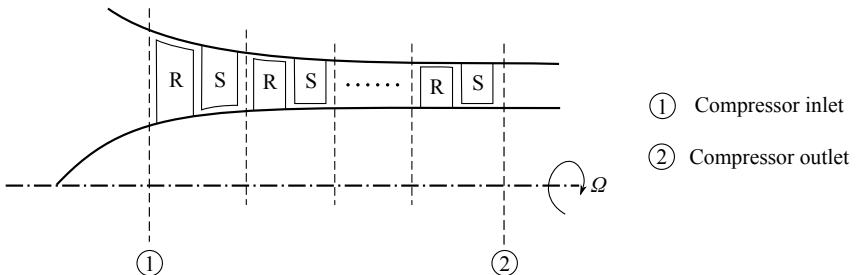


Figure 5.27: Multistage compressor.

See Fig. 5.28 for compressor/stage performance and Fig. 5.29 for compressor characteristics. The compressor map shows contributions from all stages. Mass flow rate and engine speed change during mission (cruise, take-off, landing and idling).

Surge line is the locus of unstable operation of the compressor, meaning the compressor is under the condition of unsteady flow as a result of boundary layer separation, which has rapid decrease in p_{02}/p_{01} at highest flow rate. This causes the choking condition (flow rate independent of pressure ratio). Consequences of

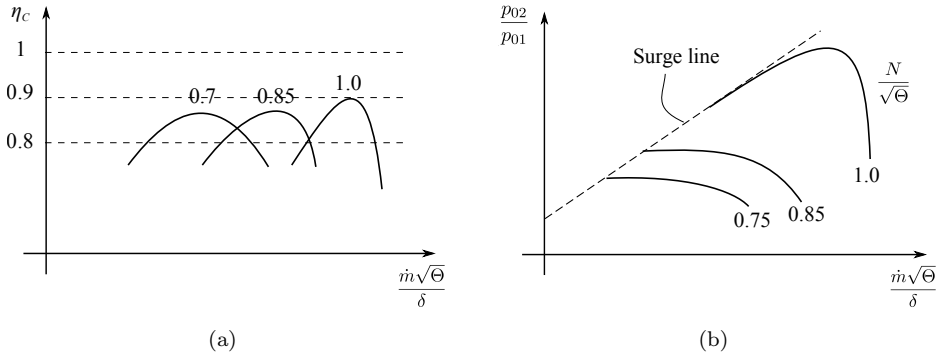


Figure 5.28: Compressor/stage performance.

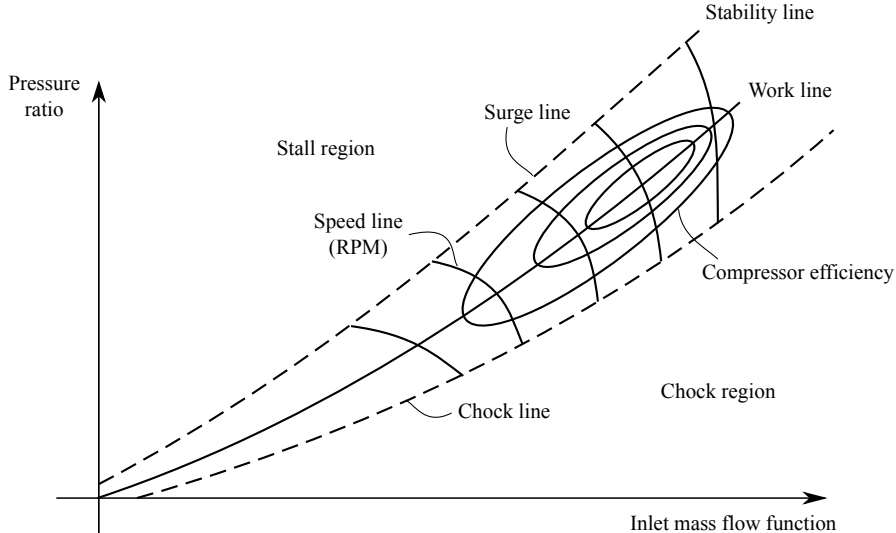


Figure 5.29: Compressor characteristics.

surge is the pressure oscillation that will damage or destroy the compressor blades. The principle of surge is displayed in Fig. 5.30.

Stall is boundary layer separation on compressor blade. Rotating stall is progression of local separation cell around compressor azimuthal direction. Rotation occurs due to local mass-flow blockage. This results in increase in mechanical stress on blade (potential resonant oscillation at blade vibrational frequency), large stress, and fatigue failure.

5.2.1.4. Compressor Efficiency.

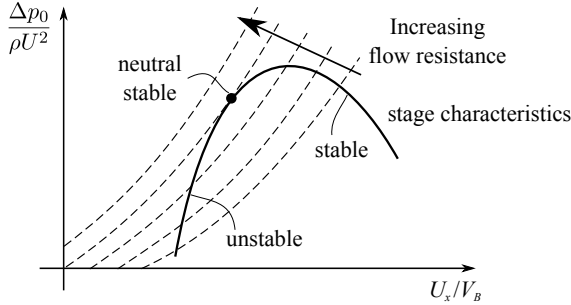


Figure 5.30: Principle of surge line.

Efficiency. Compressor efficiency η_C , which is the adiabatic efficiency across the entire compressor (see Fig. 5.31 for numbering), is defined as

$$\eta_C = \frac{h_{03s} - h_{02}}{h_{03} - h_{02}} = \frac{T_{03s}/T_{02} - 1}{T_{03}/T_{02} - 1} = \frac{(p_{03}/p_{02})^{\frac{\gamma-1}{\gamma}} - 1}{T_{03}/T_{02} - 1}. \quad (5.74)$$

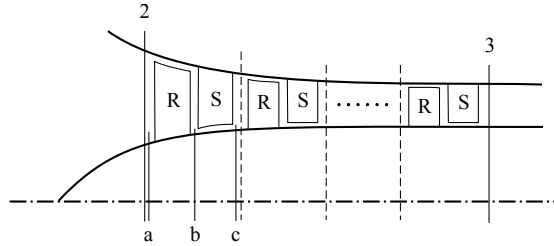


Figure 5.31: Numbering for compressor efficiency analysis.

Stage efficiency. Relate adiabatic stage efficiency to internal entropy generation. From Gibbs equation

$$\begin{aligned} ds &= c_p \frac{dT}{T} - R \frac{dp_0}{p_0} \quad (\text{integrate from } 0_{cs} \rightarrow 0_c), \\ \Delta s &= c_p \ln \left(\frac{T_{0c}}{T_{0cs}} \right), \\ \frac{T_{0c}}{T_{0a}} &= \frac{T_{0cs}}{T_{0a}} \exp \left(\frac{\Delta s}{c_p} \right), \end{aligned}$$

and with definition of adiabatic efficiency

$$\eta_{st} = \frac{h_{0cs} - h_{0a}}{h_{0c} - h_{0a}} = \frac{\frac{T_{0c}}{T_{0a}} \exp \left(-\frac{\Delta s}{c_p} \right) - 1}{\frac{T_{0c}}{T_{0a}} - 1} = \frac{\left(\frac{p_{0c}}{p_{0a}} \right)^{\frac{\gamma-1}{\gamma}} - 1}{\left(\frac{p_{0c}}{p_{0a}} \exp \left(\frac{\Delta s}{c_p} \right) \right)^{\frac{\gamma-1}{\gamma}} - 1}. \quad (5.75)$$

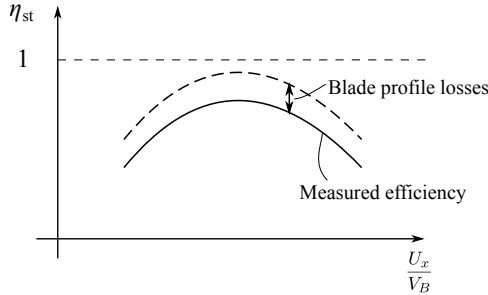


Figure 5.32: Stage efficiency.

5.2.1.5. Cascade Aerodynamics. Performance of turbomachinery stage is done in static cascade experiments/tests. Characterization of cascade experiments:

$$\beta_{ii}, \frac{\Delta p}{\frac{1}{2}\rho_1 w_i^2} = f(\beta_i; \underbrace{\frac{w_i C}{\gamma}}_{\text{Cord Reynolds number}}; \underbrace{\frac{w_i}{\sqrt{\gamma R T}}}_{\text{Mach number}}; \underbrace{\frac{C}{s}}_{\text{Solidity}}; \underbrace{\lambda}_{\text{Stagger angle}}), \quad (5.76)$$

where $\frac{\Delta p}{\frac{1}{2}\rho_1 w_i^2} \equiv \xi$ is the stagnation loss ratio, C is the cord length, s is the spacing, and *lambda* is the stagger angle.

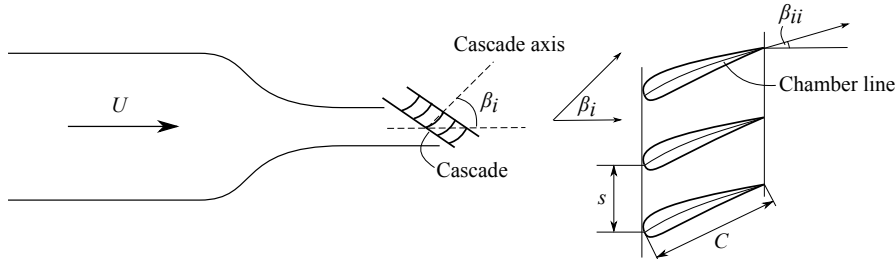


Figure 5.33: Cascade experiments/tests.

From velocity triangle, we know that β_i does not affect β_{ii} , but β_i increases adverse pressure gradient (which causes boundary layer separation).

5.2.1.6. Radial Equilibrium. So far, we neglected radial variations through compressor annulus, and only considered to mean radius. Compressor design requires consideration of radial variations in:

- Blade speed: $V_B = \Omega r$;
- Axial velocity: U_x ;
- Tangential velocity: U_θ ;
- Static pressure.

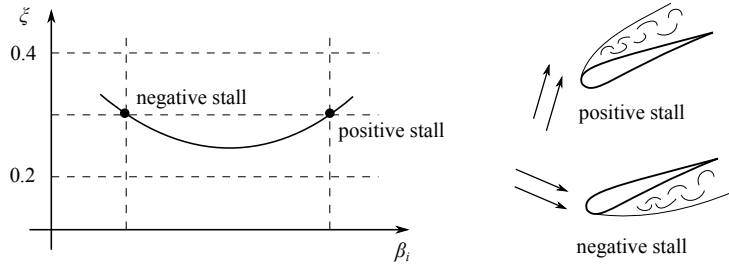


Figure 5.34: Stagnation loss ratio.

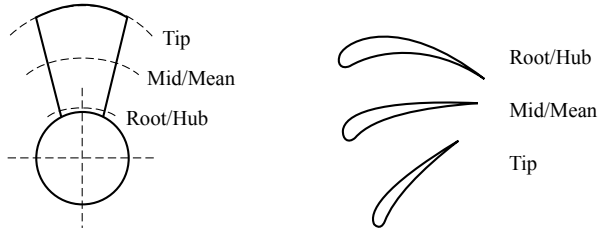


Figure 5.35: Radial variation.

The objective is to derive differential equation for enthalpy to consider radial variations of turbine annulus:

$$h_{02} - h_{01} = V_B \Delta U_\theta .$$

First, we will derive the pressure variation in the radial direction which will be useful later. Consider the control mass as shown in Fig. 5.36. The centripetal acceleration of the mass δm (centripetal force) is

$$F_r = -\delta m \left(\frac{U_\theta^2}{r} \right) . \quad (5.77)$$

The force balance with pressure is

$$F_r = prd\theta dx - (p + \frac{dp}{dr}dr)(r + dr)d\theta dx + 2(prdx)\frac{d\theta}{2} , \quad (5.78)$$

and hence we have

$$F_r = -r \frac{dp}{dr} dr d\theta dx . \quad (5.79)$$

With $\delta m = \theta r dr d\theta dx$, we have

$$\frac{dp}{dr} = \rho \frac{U_\theta^2}{r} . \quad (5.80)$$

From energy balance $\Delta h_0 = V_B \Delta U_\theta$ and differentiating

$$\frac{\partial}{\partial r}(\Delta h_0) = \Omega \frac{\partial}{\partial r}(r \Delta U_\theta) \quad (5.81)$$

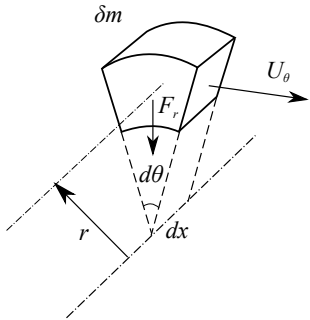


Figure 5.36: Force balance.

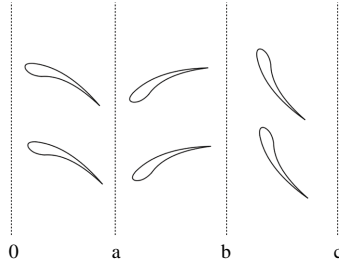


Figure 5.37: Schematic of a single compressor stage with the inlet guide vane (IGV) from stage 0 to a, rotor from stage a to b, and stator from stage b to c.

where $V_B = r\Omega$. To achieve constant stagnation enthalpy, we require that $r\Delta U_\theta$ to be constant and one way to achieve this is the free-vortex design where we have rU_θ is constant. So we have the velocity in the three radial locations:

$$\text{Mid-velocity: } U_{\theta,m}r_m = \text{const}, \quad (5.82)$$

$$\text{Hub-velocity: } U_{\theta,h} = U_{\theta,m} \frac{r_m}{r_h}, \quad (5.83)$$

$$\text{Tip-velocity: } U_{\theta,t} = U_{\theta,m} \frac{r_m}{r_t}. \quad (5.84)$$

Issue with this is that it requires large blade twist. To reduce the blade-twist angle, we can invoke $r\Delta U_\theta$ to be constant instead of rU_θ , which results in symmetric velocity triangle.

To further analyze the vortex design of the compressor, here we define the degree of reaction as the fraction of static enthalpy rise across the stage that is accomplished by the rotor, which is:

$$^oR = \frac{h_b - h_a}{h_c - h_a}, \quad (5.85)$$

with the labeling of stages shown in Fig. 5.37. Note that there is no work done by

the stator across stages b and c ($h_{0b} = h_{0c}$) but it works as a diffusor after which the velocity reduces and temperature increases.

Assuming that the compressor stages are repeated, i.e. $U_a = U_c$, the degree of reaction can be simplified as:

$$\begin{aligned}\circ R &= \frac{h_{0b} - h_{0a} - \frac{1}{2}(U_b^2 - U_a^2)}{h_{0c} - h_{0a} - \frac{1}{2}(U_c^2 - U_a^2)} \\ &= 1 - \frac{U_b^2 - U_a^2}{2(h_{0b} - h_{0c})} \\ &= 1 - \frac{U_x^2 + U_{\theta,b}^2 - U_x^2 - U_{\theta,a}^2}{2V_B(U_{\theta,b} - U_{\theta,a})} \\ &= 1 - \frac{U_{\theta,b} + U_{\theta,a}}{2V_B}.\end{aligned}\quad (5.86)$$

With this, the general stage vortex design (with IGV) takes the form:

$$rU_{\theta,a} = rU_{\theta,c} = -b + ar^n, \quad (5.87)$$

$$rU_{\theta,b} = b + ar^n. \quad (5.88)$$

When used in this context, a and b here are numerical constants (and do not refer to the stages). The degree of reaction is then:

$$\circ R = 1 - \frac{U_{\theta,b} + U_{\theta,a}}{2\Omega r} = 1 - \frac{ar^{n-2}}{2\Omega}. \quad (5.89)$$

For $n = 2$, the degree of reaction is constant; $n > 2$ the degree of reaction deceases along the span; $n < 2$ the degree of reaction increases along the span.

Without the IGV ($U_{\theta,a} = U_{\theta,c} = 0$), two designs are commonly used which are:

- Free vortex $rU_{\theta,b} = a$ (The flow field is a potential flow.)
- Forced vortex $rU_{\theta,b} = ar^2$ (The rotor induced swirl increases linearly with the radius, i.e. fluid experiencing a solid body rotation. This relies on the stator to remove the swirls induced by the rotor.)

Note that the general stage vortex design is a combination of solid body rotation (forced vortex) and a free-vortex swirl distribution.

Here is a summary of the vortex design choices:

- Free vortex: $rU_{\theta} = a$,
- Forced vortex: $rU_{\theta} = ar^2$,
- Exponential: $rU_{\theta} = ar + b$,
- Constant reaction: $rU_{\theta} = ar^2 + b$,

where $a > 0$ and b are constants.

5.2.1.7. Entropy Conservation. From entropy conservation (second law), we have

$$T \frac{ds}{dr} = \frac{dh}{dr} - \frac{1}{\rho} \frac{dp}{dr}. \quad (5.90)$$

With stagnation enthalpy $h_0 = h + \frac{1}{2}U^2$ and $U^2 \simeq U_\theta^2 + U_x^2$ (with U_r to be small), we have

$$T \frac{ds}{dr} = \frac{dh_0}{dr} - \frac{1}{2} \frac{d}{dr}(U_\theta^2 + U_x^2) - \frac{1}{\rho} \frac{dp}{dr}, \quad (5.91)$$

and with dp/dr substituted from Eq. (5.80), we have

$$T \frac{ds}{dr} = \frac{dh_0}{dr} - \frac{1}{2} \frac{d}{dr}(U_\theta^2 + U_x^2) - \frac{U_\theta^2}{r}. \quad (5.92)$$

With requirement for vanishing radial gradients of entropy and enthalpy, we have

$$\frac{d}{dr}(U_x^2) = -\frac{1}{r^2} \frac{d}{dr}(rU_\theta)^2. \quad (5.93)$$

For free vortex ($rU_\theta = a$):

$$\frac{d}{dr}(U_x^2) = -\frac{1}{r^2} \frac{d}{dr}a^2,$$

so we have U_x is constant in this case.

5.2.1.8. Examples of Blade Designs. Here, we show examples of blade designs using the four vortex design choices discussed above. From radial equilibrium, we have

$$\begin{aligned} F_r &= -r \frac{dp}{dr} dr d\theta dx \\ &= -r\rho \frac{U_\theta^2}{r} dr d\theta dx \\ &= -\rho \frac{(rU_\theta)^2}{r^2} dr d\theta dx. \end{aligned} \quad (5.94)$$

where $dp/dr = \rho U_\theta^2/r$. Integrate over the radial and azimuthal direction:

$$\begin{aligned} F_r &= \int_{r_h}^{r_t} \int_0^{2\pi} -\rho \frac{(rU_\theta)^2}{r^2} dr d\theta dx \\ &= -2\pi\rho \int_{r_h}^{r_t} \frac{(rU_\theta)^2}{r^2} dr dx. \end{aligned} \quad (5.95)$$

Therefore, for each of the blade designs obtained with the four velocity profiles:

- Free vortex

$$\begin{aligned} F_r &= -2\pi\rho \int_{r_h}^{r_t} \frac{a^2}{r^2} dr dx \\ &= \frac{2\pi\rho a^2 dx}{r} \Big|_{r_h}^{r_t} \\ &= 2\pi\rho a^2 \left(\frac{1}{r_t} - \frac{1}{r_h} \right) dx. \end{aligned} \quad (5.96)$$

- Forced vortex

$$\begin{aligned}
 F_r &= -2\pi\rho \int_{r_h}^{r_t} \frac{a^2 r^4}{r^2} dr dx \\
 &= -\frac{2}{3}\pi\rho a^2 r^3 dx|_{r_h}^{r_t} \\
 &= -\frac{2}{3}\pi\rho a^2 (r_t^3 - r_h^3) dx.
 \end{aligned} \tag{5.97}$$

- Exponential

$$\begin{aligned}
 F_r &= -2\pi\rho \int_{r_h}^{r_t} \frac{a^2 r^2 + 2abr + b^2}{r^2} dr dx \\
 &= -2\pi\rho (a^2 r + 2ab \ln r - \frac{b^2}{r}) dx|_{r_h}^{r_t} \\
 &= -2\pi\rho [(r_t - r_h)a^2 + 2 \ln(r_t/r_h)ab - (1/r_t - 1/r_h)b^2] dx.
 \end{aligned} \tag{5.98}$$

- Constant reaction

$$\begin{aligned}
 F_r &= -2\pi\rho \int_{r_h}^{r_t} \frac{a^2 r^4 + 2abr^2 + b^2}{r^2} dr dx \\
 &= -2\pi\rho \left(\frac{a^2}{3} r^3 + 2abr - \frac{b^2}{r} \right) dx|_{r_h}^{r_t} \\
 &= -2\pi\rho \left[\frac{r_t^3 - r_h^3}{3} a^2 + 2(r_t - r_h)ab - (1/r_t - 1/r_h)b^2 \right] dx.
 \end{aligned} \tag{5.99}$$

Assume the centrifugal force for the four designs are the same, from the free vortex design we have:

$$\begin{aligned}
 a_{\text{free vortex}} &= r_h U_{\theta,h} \\
 &= r_h (r_h \Omega - u_x \tan \beta_{a,h}),
 \end{aligned} \tag{5.100}$$

and the centrifugal force is computed using Eq. (5.96). Now, substituting F_r into Eqs. (5.97) to (5.99), the parameters a and b are obtained. The orientation of the blade for each vortex design is then computed as:

$$\beta_a(r) = \tan^{-1} \left(\frac{r\Omega - rU_\theta/r}{u_x} \right). \tag{5.101}$$

Assume $u_x = 325$ m/s, $V_{B,m} = 200$ m/s, $r_m = 0.5$ m, $r_h/r_t = 0.33$, $\beta_{a,h} = 5^\circ$, β_a for each vortex design is shown in Fig. 5.38. The CAD drawings for the compressor blades with the four vortex designs obtained in this example are shown in Fig. 5.39.

5.2.1.9. Design of Single-Stage Subsonic Axial Compressor. Our objective is the basic system design of axial compressor and to determine flow field that is compatible with high efficiency, given pressure ratio, and minimum compressor size. Design approaches are low-order (0/1D) models and multidimensional models such as

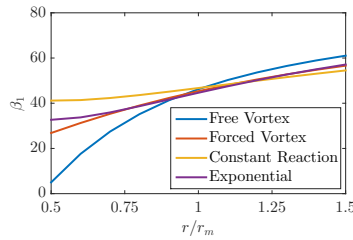


Figure 5.38: Example of vortex designs.

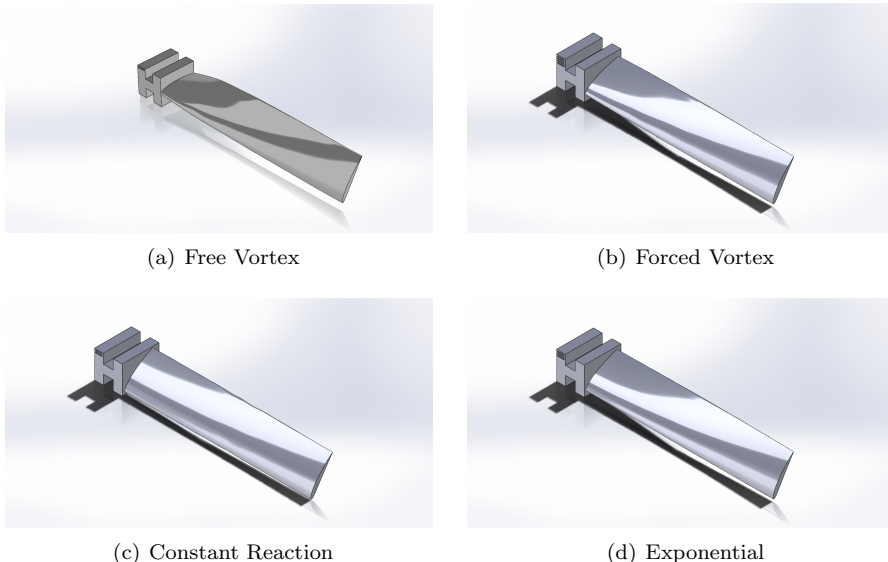


Figure 5.39: CAD drawings for the compressor blade following the vortex designs in the example.

- Streamline/stream function/potential flow;
- Euler equation (most common).

Here, we consider a preliminary design to address:

- Radial equilibrium;
- Velocity triangles;
- Number of stages;
- Compressor size;
- Consequences of small departures.

The design strategy is that we will assume high Reynolds number turbulent flows through the compressor so that we have small or attached boundary layer. The shock waves and flow separations are avoided.

Approximations are that we have negligible radial velocity such that $U_r^2 \ll U_\theta^2, U_x^2$, and we have calorically perfect gas and the friction effects are neglected.

(1) Stagnation temperature:

- No radial variation in stagnation temperature;
- Adiabatic compressor.

(2) Entropy:

- Frictionless and adiabatic compressor so that we have constant entropy in stage;
- Fluid entering compressor with uniform state:

$$\frac{ds}{R} = \frac{\gamma}{\gamma - 1} \frac{dT_0}{T_0} - \frac{dp_0}{p_0} .$$

Since $s \neq s(r)$ and $T \neq T_0(r)$, we have $p_0 \neq p_0(r)$. So we have constant along the radial direction.

(3) Mass flow rate:

- Mass flow rate upstream of rotor leading edge:

$$\dot{m} = \int_{r_{\text{Hub}}}^{r_{\text{Tip}}} \rho U_x 2\pi r dr .$$

- Relation between density and velocity is

$$\frac{\rho}{\rho_{0a}} = \left(\frac{T}{T_{0a}} \right)^{\frac{1}{\gamma-1}} ,$$

$$T_{0a} = T + \frac{U^2}{2c_p} = T + \frac{U_\theta^2 + U_x^2}{2c_p} ,$$

$$\frac{\rho}{\rho_{0a}} = \left[1 - \frac{U_\theta^2 + U_x^2}{2T_{0a}c_p} \right]^{\frac{1}{\gamma-1}} .$$

(4) Work and pressure ratio:

- Pressure ratio across stage:

$$\frac{p_{0c}}{p_{0a}} = \left[1 + \eta_{st} \frac{V_B \Delta U_\theta}{c_p T_{0a}} \right]^{\frac{\gamma}{\gamma-1}} .$$

- Good estimate for η_{st} is about 0.88.

(5) Rotor inlet relative Mach number:

- Highest relative Mach number is assumed to be in the inlet to the rotor at the tip

$$M_{a,\text{Tip}} = \frac{\omega_{a,\text{Tip}}}{\sqrt{\gamma R T_{a,\text{Tip}}}} \leq 0.75 \dots 0.8 ,$$

and $\omega_{a,\text{Tip}}^2 = U_{xa,\text{Tip}}^2 + (V_B - U_{\theta,a,\text{Tip}})^2$ from velocity triangle.

(6) Radial equilibrium:

- From Eq. (5.93), we have

$$\frac{d}{dr}(U_x^2) = -\frac{1}{r^2} \frac{d}{dr}(rU_\theta)^2,$$

and design choice of angular momentum distribution

$rU_\theta = ar + b$ (assume to be exponential distribution)

to ensure constant work

$$\Delta(rU_\theta) = (rU_\theta)_b - (rU_\theta)_a = \text{const}$$

with $V_B = r\Omega$ and $rU_\theta = ar + b$, we have

$$\frac{V_B}{\Omega} \Delta U_\theta = (a_{\text{at stage b}} r + b_{\text{at stage b}}) - (a_{\text{at stage a}} r + b_{\text{at stage a}})$$

so we have

$$a_{\text{at stage a}} = a_{\text{at stage b}} + a \quad \text{and} \quad b_{\text{at stage b}} = b_{\text{at stage a}} + \frac{V_B \Delta U_\theta}{\Omega}$$

$$r_{\text{Tip}} U_{\theta,a,\text{Tip}} = ar_{\text{Tip}} + b_{\text{at stage a}}.$$

Axial Compressor Design Example:

Consider mid-radius of compressor with constant axial velocity component

$$U_{xa}|_{r_m} = U_{xb}|_{r_m}.$$

Design process:

- Stagnation point:
 - Overall stage pressure ratio: p_{0c}/p_{0a} ;
 - Stage efficiency: η_{st} ;
 - Maximum relative Mach number: $M_{a,\text{rel}}$;
 - Degree of reaction (coupling between rotor and stator):

$$R = \frac{h_b - h_a}{h_{0c} - h_{0a}}.$$

- Iterative solution to find:
 - Dimensional tip speed;
 - Dimensional swirl number;
 - Hub-to-tip radius ratio: $\xi = r_{\text{Hub}}/r_{\text{Tip}}$.

5.2.2. Turbine and Compressor Matching. Matching turbine and compressor performance is essential to achieve maximum overall engine performance over the wide range of operating conditions to which an engine may be subject, including inlet pressure and temperature and flight Mach number. For a turbojet engine at steady-state with all bleed valves closed, the matching conditions are continuity of flow and power balance, expressed $\dot{m}_t = \dot{m}_c + \dot{m}_f$ and $w_t = -w_c$, respectively. Enforcing these two conditions simultaneously using the known performance maps for the compressor and turbine is generally an iterative procedure for each shaft

speed at which the engine is to operate. For a given shaft speed, the iterative matching procedure is as follows:

- Assume turbine inlet temperature T_{04} ;
- Assume compressor pressure ratio π_c ;
- Calculate compressor work per unit mass w_c ;
- Calculate turbine pressure ratio π_t required to produce compressor work;
- Check mass conservation between compressor and turbine. If mass is not conserved, use new π_c and repeat;
- Compute pressure ratio across jet nozzle;
- Compute area of nozzle outlet. If area is not equal to designed nozzle area, assume new T_{04} and repeat.

Having followed this procedure, the engine performance in terms of available thrust and efficiency can subsequently be computed for the given shaft speed following the analysis of Sec. 4.2. A shaft speed for which both matching conditions have been satisfied in the manner described above is a point on the engine operating ‘line’, discussed below.

5.2.3. Engine Operating Line. The engine operating line, or ‘equilibrium running line’, is the locus points representing shaft speeds for which the compressor and turbine could be successfully matched based on the procedure above. Whereas the compressor and turbine maps represent all the steady-state conditions those components can achieve independently, the operating line constitutes all the steady-state conditions achievable by the integrated engine at a given altitude and flight Mach number. The operating line is thus directly influenced by the performance of the individual turbomachinery components. The matching conditions discussed above restrict the range of operating conditions achievable for the individual turbomachinery components, resulting in the operating line being represented by a single line on the compressor and turbine maps. In Fig. 5.40, the operating line is shown as a line on a compressor map.

As was discussed above, a single shaft speed represents a single point on the engine operating line, resulting in a particular available thrust and efficiency. During flight, the operator must be able to vary the performance of the engine dynamically to achieve operation at different points on the operating line. For a given engine, the operating point achieved on the operating line is determined principally by the throttle position i.e. fuel/air ratio, and the flight conditions in terms of ambient conditions due to altitude and flight Mach number. The engine designer must therefore ensure that all conditions possible within the aircraft’s operating envelope e.g. takeoff, cruise and approach are achievable on the engine’s operating lines, and furthermore that the design point i.e. the cruise condition corresponds closely to the maximum efficiency point for the turbomachinery.

It should be noted that the lines of constant T_{04}/T_{02} in Fig. 5.40 are plotted as straight lines radiating from the origin. Rewriting the ordinate variable in terms

of T_{04}/T_{02} we have

$$\frac{\dot{m}\sqrt{\Theta}}{\delta} = \frac{\dot{m}\sqrt{T_{04}}}{p_{04}} \frac{p_{04}}{p_{02}} \frac{p_{03}}{p_{02}} \sqrt{\frac{T_{02}}{T_{04}}} \frac{p_{\text{std}}}{\sqrt{T_{\text{std}}}}, \quad (5.102)$$

where $\Theta = T_{02}/T_{\text{std}}$ and $\delta = p_{02}/p_{\text{std}}$. The combustor pressure ratio $p_{04}/p_{03} \approx 1$ for all stable operating conditions. If we further assume that the turbine inlet nozzle is choked, then $\frac{\dot{m}\sqrt{T_{04}}}{p_{04}} = \text{const}$, and thus

$$\frac{p_{03}}{p_{02}} \propto \sqrt{\frac{T_{04}}{T_{02}}} \frac{\dot{m}\sqrt{\Theta}}{\delta}, \quad (5.103)$$

which yields the form of the lines of constant T_{04}/T_{02} shown in Fig. 5.40.

To illustrate these concepts, consider an aircraft in steady level flight, whose engine operating line corresponds to that shown in Fig. 5.40. During cruise, the engine operates near its design point A, which is near the maximum efficiency point of the compressor. If greater thrust is desired, the throttle position is advanced, increasing the fuel/air ratio. This results in a near-immediate increase in T_{04} . Since the rotor has significant inertia, it is slower to accelerate, during which time the compressor moves along a line of constant $N/\sqrt{\Theta}$, increasing p_{03}/p_{02} , but also bringing operation closer to the surge line. The increased T_{04} results in an increase in w_t , which results in a gradual increase in N and \dot{m} . This cascade of events thus results in the operating point moving from A to B, where thrust has increased and efficiency has reduced, and also shows the importance of gradual throttle control: a rapid change can result in compressor surge. Reducing the throttle to reach point C, where thrust is reduced below its cruising level for approach and landing, is also seen to result in reduced efficiency.

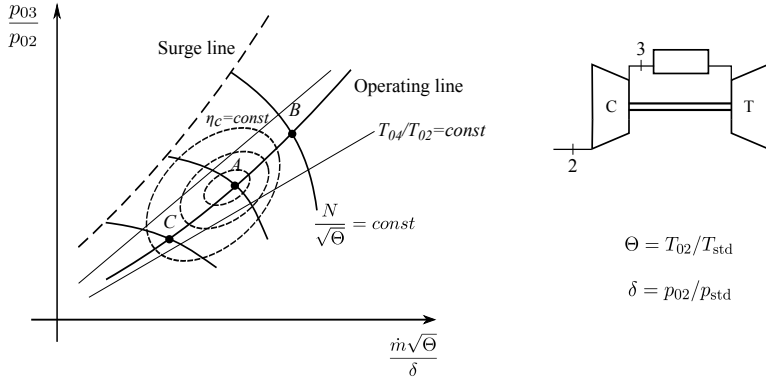


Figure 5.40: Compressor map showing operating line of an integrated engine.

5.2.3.1. Double-Choked Turbojet Operating Line.

The discussion above focused on the general case of unchoked flow through a gas turbine engine, which necessitates an iterative approach to compressor-turbine matching. However, for turbojet engines, some simplifying assumptions can be

applied to the analysis. Specifically, for a high pressure-ratio turbojet, the turbine inlet nozzle and propulsion nozzle will be choked for most operating conditions i.e. $M_4 = M_5 = 1$. This occurs at high pressure conditions, as shown in Fig. 5.41. The double-choked condition implies that

$$\frac{\dot{m}\sqrt{T_{04}}}{p_{04}} = \text{const}, \quad \frac{\dot{m}\sqrt{T_{05}}}{p_{05}} = \text{const}, \quad (5.104)$$

from which it is seen that

$$\frac{p_{05}}{p_{04}} \sim \left(\frac{T_{05}}{T_{04}} \right)^{1/2}. \quad (5.105)$$

Assuming for simplicity that the turbine consists of a single stage, the temperature change across the turbine can be expressed as in Sec. 5.2.1 using the blade geometry and velocities as

$$\frac{T_{05}}{T_{04}} = 1 - \frac{V_B}{c_p T_{04}} [U_x (\tan \alpha_a + \tan \beta_b) - V_B]. \quad (5.106)$$

A choked turbine inflow implies that $U_x/\sqrt{\gamma R T_{04}}$ is constant. The above equation implies then that $V_B/\sqrt{\gamma R T_{04}}$ is constant, and thus $V_B \propto \sqrt{T_{04}}$, from which it follows that $N \propto \sqrt{T_{04}}$. Furthermore, if both $U_x/\sqrt{\gamma R T_{04}}$ and $V_B/\sqrt{\gamma R T_{04}}$ are constant, then U_x/V_B is constant. This is important, since it means that all the flow angles of the stage's velocity triangles remain constant. Hence, even as T_{04} , p_{04} and N vary along the operating line, so long as both turbine inlet and outlet nozzles remain choked, the turbine operates at the same non-dimensional operating point.

The double choked condition on the turbine yields the form of the engine operating line on the compressor map. Expressing the compressor flow rate as

$$\frac{\dot{m}\sqrt{R T_{01}}}{p_{01} D^2} = \frac{\dot{m}\sqrt{R T_{04}}}{p_{04} D^2} \frac{p_{04}}{p_{03}} \frac{p_{03}}{p_{02}} \frac{p_{02}}{p_{01}} \sqrt{\frac{T_{01}}{T_{04}}}, \quad (5.107)$$

where $\frac{\dot{m}\sqrt{R T_{04}}}{p_{04} D^2}$ is constant and $\frac{p_{04}}{p_{03}} \approx 1$. Since for the double-choked turbine $T_{04} \propto N^2$, the compressor pressure ratio can be expressed explicitly as a function of the shaft speed as

$$\frac{p_{03}}{p_{02}} \propto \frac{N}{\sqrt{T_{01}}} \frac{\dot{m}\sqrt{R T_{01}}}{p_{01} D^2}. \quad (5.108)$$

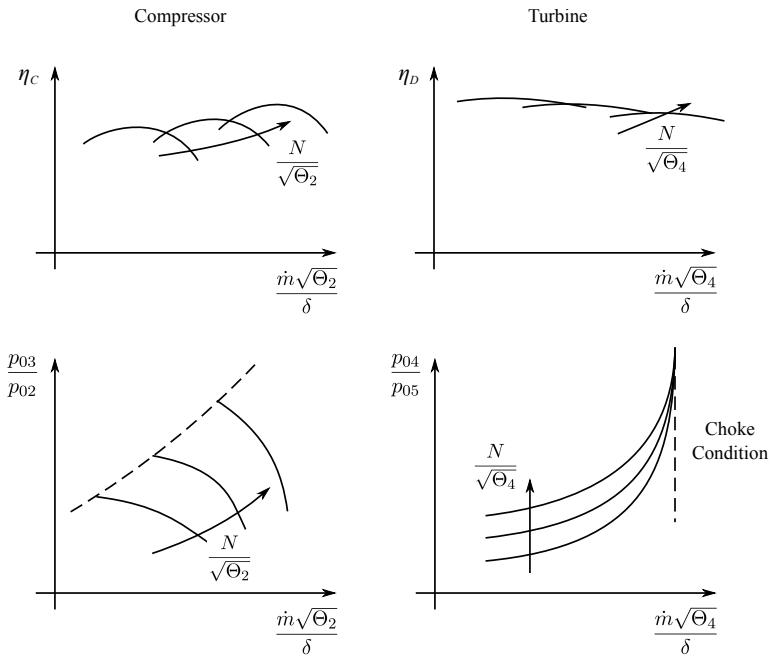


Figure 5.41: Compressor and turbine maps, showing compressor surge and turbine choke conditions.

Mechanical Design of Gas Turbines

So far in this text, gas turbine engines have been analyzed in the context of their thermodynamic cycle and the aero-thermodynamics of the associated internal and external fluid flow. In this chapter, the mechanical design of engine components is considered. The mechanical design of an engine requires a preliminary aerodynamic design of the individual engine components in terms of their size, dimension, number of stages, etc.

6.1. Engine Development Cycle

Engine mechanical design can be considered in the context of the following question: can the materials in the engine sustain the loads to which they are subject? These include thermal, structural and vibrational loads arising from steady-state and dynamic processes during engine operation. This question is addressed during the mechanical design phase of the engine development cycle, shown in Fig. 6.1 below.

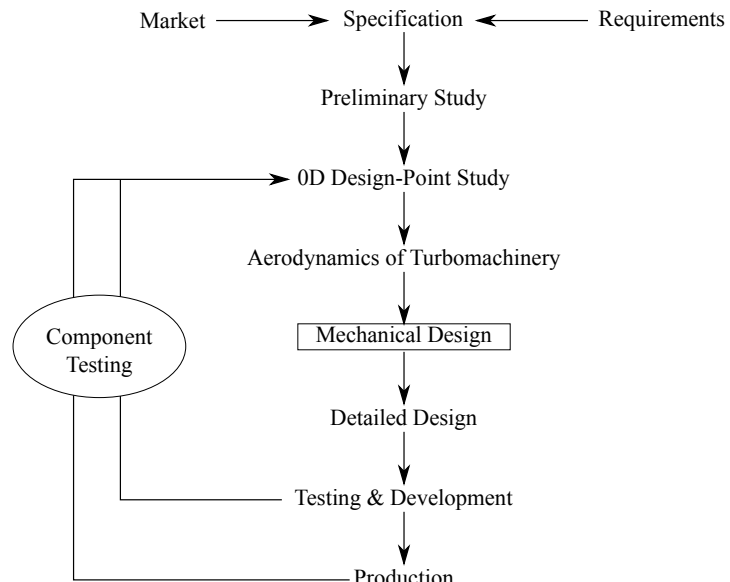


Figure 6.1: General outline of the development cycle for a gas turbine engine.

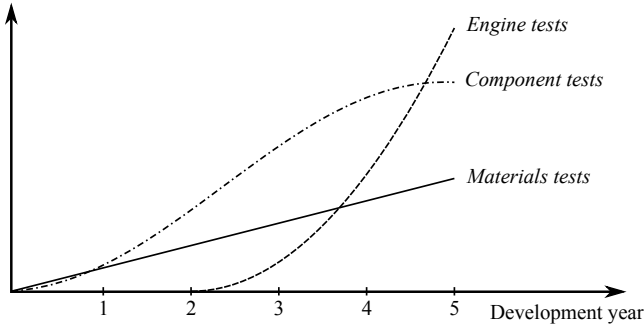


Figure 6.2: Typical engine testing schedule.

Ultimately, engine design is driven by two often competing forces: the engine market, which demands certain features and capabilities, and the regulatory agencies, which require adherence to wide range of standards. Market research and an understanding of the regulatory environment ultimately lead to the development of a detailed set of design requirements. Those design requirements have an associated set of certification requirements set by the regulator. Certification is then achieved through a combination of experiments and analysis.

Certification for a complete engine is achieved following a building block approach. At the first stage, the materials used for construction of individual components must be certified. Next, components are tested individually. Subsystems consisting of multiple components are then tested. Only once all these stages have been successfully completed is the full engine tested and certified.

Given the number of tests requiring successful completion to achieve engine certification, the engine development cycle is necessarily long. Figure 6.2 shows a typical testing schedule for engine development. A typical development cycle will require some 10,000 hours of testing, including the test of ten to thirty full-scale engines. So much testing places an enormous financial burden on the engine manufacturer, and hence strategies for acceleration of the development cycle are often employed. These are often the use of industry-accepted best practices, and increasingly the use of virtual testing i.e. the use of simulation tools to predict component behavior.

6.2. Engine Loads

The loads experienced by components in a gas turbine engine can be divided into two distinct categories: external loads and internal loads. It is noted that the external loads listed are not relevant for stationary gas turbine engines.

External loads:

- Aerodynamic loads
 - Taxiing
 - Take-off
 - Landing

- Maneuvering
- Impact loads
 - Birds, etc.

Internal loads:

- Rotational forces
- Pressure/temperature loading
- Start-up loads
- Transient processes

Among internal loads, the rotational loads in particular can be understood in the context of classical kinematic analysis. The centripetal force F_c on any object of mass m displaced from an instantaneous center of rotation by a distance r moving at a tangential velocity u is $F_c = m\frac{u^2}{r}$ directed toward the instantaneous center. For an object rotating about a fixed axis at a constant rate of rotation Ω , $u = \Omega r$, and thus

$$F_c = m\Omega^2 r. \quad (6.1)$$

6.3. Failure Modes

Engine failure is driven by sub-system failures, which are in turn driven by component failures. Component failure is characterized as a change in component configuration, size, surface properties or other material property from its nominal design limits. There are numerous failure modes of relevance to gas turbine engines. Below, a non-exhaustive list of component failure types is provided.

- Fan blade: fatigue, bird strikes, erosion
- Fan disc: burst, fatigue
- Compressor blades: fatigue, erosion, corrosion
- Shaft(s): creep, low cycle fatigue
- Combustor: thermal fatigue, creep, stress
- Turbine blades: (high cycle) fatigue, creep, stress, corrosion

6.3.1. Static Failure. The behavior of materials under static loading conditions can be described by a stress-strain diagram, as in Fig. 6.3. Such a diagram is obtained by applying various static axial loads F on a material sample of unloaded cross-sectional area A_0 and length L_0 . Upon loading, the material changes in both length and cross-sectional area. The strain is defined as the ratio of the change in axial length to the unloaded length, $\epsilon = \frac{\Delta L}{L_0}$. At any given level of loading F , the axial stress is defined as $\sigma = \frac{F}{A}$, where in an engineering stress-strain diagram the A is taken as A_0 .

Most engineering materials exhibit a linear stress-strain behavior at low loads. This is known as the ‘linear-elastic’ regime, and is characterized by the Young’s modulus (or ‘modulus of elasticity’), $E = \frac{d\sigma}{d\epsilon}$. The larger the Young’s modulus, the ‘stiffer’ a material is said to be. For ductile materials, including most engineering metals, the end of the linear-elastic regime is quantified by the yield stress σ_y . Increasing the stress beyond σ_y results in plastic deformation and necking up to the ultimate tensile strength σ_f , at which point the material undergoes failure.

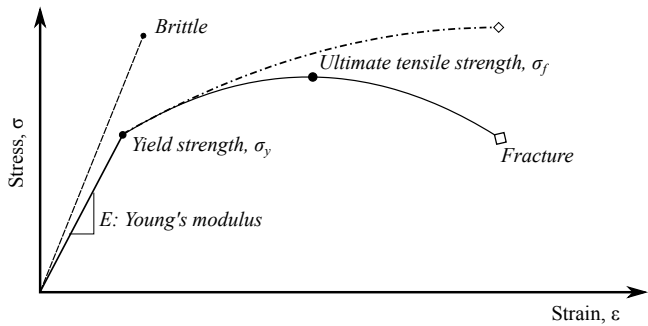


Figure 6.3: Stress-strain behavior of common engineering materials.

In engineering stress-strain diagrams of ductile materials, the failure stress is often shown as being at a higher strain and lower stress than σ_f . This is simply a consequence of the engineering convention of normalizing the applied axial load by the initial sample cross-sectional area A_0 , even though the material undergoes significant reduction in cross-sectional area due to necking beyond σ_y . The ‘true’ stress-strain behavior is shown by the dash-dotted line in Fig. 6.3. This is not of relevance to engineering design, however, since any ductile material will undergo failure if loaded to σ_f . In fact, for ductile materials, σ_f is not the relevant failure metric, but rather σ_y , since at σ_f the component has already undergone a significant change in size, which was noted above as a characteristic of component failure. For context, type 304 stainless steel has $\sigma_y \approx 215\text{MPa}$, $\sigma_f \approx 505\text{MPa}$, and $E \approx 200\text{GPa}$.

Brittle materials, including most ceramic materials, do not exhibit a significant plastic regime i.e. $\sigma_y \approx \sigma_f$. Hence, under the assumption of linear-elastic behavior, brittle materials are described by σ_f and E . For context, alumina Al_2O_3 , has $70\text{MPa} < \sigma_f < 650\text{MPa}$ and $200\text{GPa} < E < 400\text{GPa}$. The very large range of these properties, especially for σ_f , is indicative of a major drawback of brittle materials, namely that they are susceptible to fracture-driven failure, which is strongly influenced by production quality and is difficult to characterize using linear-elastic parameters. Furthermore, due to their not having a plastic deformation regime, brittle materials fail in a sudden and catastrophic manner. By contrast, when σ_y is used as the failure criterion, ductile materials fail in a gradual and predictable manner. For these reasons, high-strength ductile materials are preferred for the design and construction of engine components, especially structural members.

Though materials are often characterized for their static failure properties using tensile failure testing, static failure can occur in a number of ways, including tensile, compressive (buckling), shear and bearing failure modes. Apart from tensile failure, these failure modes are characterized by a combination of material and geometric properties. Within the limits of linear-elastic behavior, *material* properties needed for the computation of the limit strength under most static failure modes can be estimated using tensile strength properties.

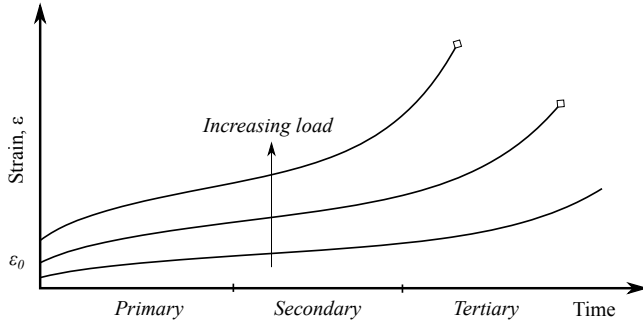


Figure 6.4: Creep characterized as an increase in strain over time under a constant loading.

6.3.2. Creep. Creep is a phenomenon which results in the deformation of components, potentially resulting in their failure due to a significant change in size or configuration, which was noted as a relevant failure characteristic above. As a macroscopic phenomenon it is characterized by a gradual increase in strain over time under a constant loading, shown in Fig. 6.4. It is rendered more severe with increasing load and with increasing temperature. There are numerous micro and meso-scale phenomena which result in creep, and different materials are susceptible to different phenomena under particular thermo-mechanical loading scenarios.

Creep must be considered in the mechanical design of any component subject to continuous loading, particularly those whose size must remain within tight tolerances. A salient example in gas turbine engines is the creep of turbine blades. A minimal blade-casing gap is desired for minimal leakage and hence maximal engine efficiency, but due to blade creep under centrifugal loading resulting from continuous operation at high shaft speeds, gap sizes must be designed against the possibility of blade-casing contact. A simple model for component creep divides the creep process into three stages and is expressed as

$$\epsilon = \epsilon_0 + \theta_1 [1 - \exp(-\theta_2 t)] + \theta_3 [\exp(-\theta_4 t) - 1], \quad (6.2)$$

where ϵ_0 is the initial (linear-elastic) strain due to the applied loading, and θ_1 , θ_2 , θ_3 , and θ_4 are model constants.

6.3.3. Fatigue Failure. Fatigue is the reduction of material strength due to cyclic loading and unloading. As a macroscopic phenomenon, it is characterized by the catastrophic failure of a component after a period of time subject to cyclic loading. It is caused by the nucleation of cracks within the material and their subsequent propagation with each loading cycle, leading eventually to failure. Assuming sinusoidal loading as in Fig. 6.5, it is characterized by a stress ratio $R = \frac{\sigma_{min}}{\sigma_{max}}$, where σ_{min} and σ_{max} are the minimum and maximum stresses of the loading cycle, $\sigma_m = \frac{\sigma_{min} + \sigma_{max}}{2}$, the mean stress of the cycle and N_f , the number of cycles until failure.

Though more difficult to accurately predict than static modes of failure, the fatigue failure of many engineering materials can be described using stress-cycle

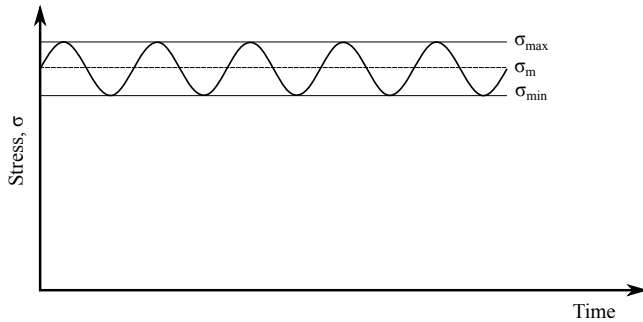


Figure 6.5: Idealization of cyclic loading leading to fatigue failure.

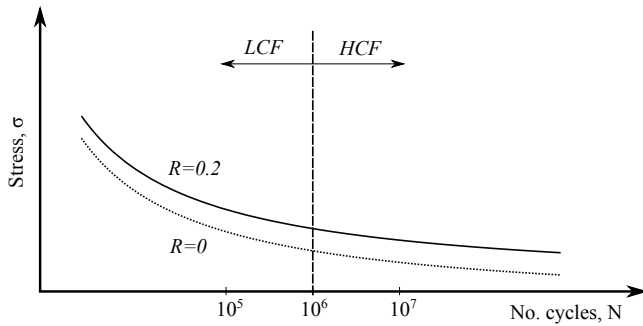


Figure 6.6: Stress-cycle diagram for the fatigue failure of engineering materials.

diagrams as in Fig. 6.6. From the figure, it is clear that for a given mean loading σ , increased R results in fewer cycles to failure. It is common to divide the fatigue failure of components into two categories: high-cycle fatigue and low-cycle fatigue.

6.3.3.1. High-Cycle Fatigue (HCF). HCF is typically defined as fatigue failure occurring after more than 10^6 loading cycles. It is often associated with vibrational loads due typically to their high frequency and low amplitude. For example, a vibrational load having a frequency $f = 1\text{kHz}$ applied to a component for 3 hours results in approximately 10^7 cycles. In the context of gas turbine engines, HCF is often associated with cyclic loads arising from shaft rotation, since shaft speeds are typically $\mathcal{O}(1)\text{kHz} < \Omega < \mathcal{O}(100)\text{kHz}$, with loading cycles leading to fatigue failure accumulating over the course of a single flight and across the multiple flights between maintenance cycles. An important means for reducing HCF is thus the reduction of the mean stress to which a component is subject.

6.3.3.2. Low-Cycle Fatigue (LCL). LCL is defined as fatigue failure occurring after less than 10^6 loading cycles. It is often associated with loads which remain approximately constant throughout each flight. Hence in LCL, each loading cycle corresponds to one flight. An example of such loading in the engine is the thrust

loading applied to the structure of the engine during operation, which must be transferred to the airframe in order to provide motive force.

An important aspect of fatigue failure is thermomechanical fatigue. This failure mode is associated with the cyclic thermal loading of mechanically loaded components. In an engine, this is of particular relevance to the durability of turbine blades. Due to the presence of inlet guide vanes and stator blades, turbine blades are subject to temporally-varying thermal loads during steady operation, irrespective of the combustor exit flow's thermal pattern factor. This is due to the static geometry providing a level of thermal shielding from the incoming flow of combusted gases, which results in a variation of the thermal loading to which a turbine blade is subject each time it passes behind one of these components.

Another time-dependent failure mode is oxidation and hot corrosion. Though not strictly a fatigue failure mode, it is a gradual degradation of material strength which can lead to failure. It is relevant in the 'hot' sections of the engine, in particular the combustor and the turbine, where the combination of high temperatures and the presence of highly reactive chemical species due to combustion can result in the degradation of the surface properties of those components. Various methodologies are thus employed for shielding exposed surfaces from the potentially destructive effects of the combusted gases, including coatings, claddings and air films.

6.4. Design Against Failure

The design of components against failure is motivated by an abundance of caution for the safety of the integrated system, recognizing that the failure of any given component can compromise the operation of the entire engine, potentially placing the lives of the public at risk. Aircraft design strategies are therefore highly conservative, while recognizing that an excess of conservatism in design is generally detrimental to aircraft weight and efficiency, and ultimately compromises the economic viability of the design.

6.4.1. Static Failure. Individual components are generally designed at a 'three-sigma' level of confidence relative to material properties. Due to variability in the quality and manufacturing processes of engineering materials, material properties are generally provided in a probabilistic manner, with a mean and standard deviation. A three-sigma design strategy thus considers the design value of any material property x having a mean value x_μ and standard deviation x_σ as $x_{design} = x_\mu - 3x_\sigma$. In this way, it is ensured that 99.99% of the materials used in the construction of each component have *at least* a property value (for example, yield strength σ_y) of x_{design} .

Other criteria for design against static failure include:

- No yield of materials allowed at maximum nominal load, referred to as the 'design limit'
- No failure allowed at $1.5 \times$ the maximum nominal load, referred to as the 'design ultimate load'
- No combustor failure at $2 \times$ the maximum operating pressure

- No rotor failure at 122% of the maximum operating speed

6.4.2. Fatigue Failure. The design against fatigue failure requires the consideration of the entire operational life cycle of each component. Different aspects of operation (e.g. takeoff, landing, cruise) will cause different amounts of damage to different engine components. One means for estimating component life is through the consideration of damage accumulation. An estimate for damage accumulation is provided by Miner's rule

$$D_f = \sum_{i=1}^k \frac{n_i}{N_i}, \quad (6.3)$$

where D_f is the accumulated damage due to fatigue, k is the number of different stress levels σ to which the component is exposed, N_i is the number of cycles to fatigue failure at a particular stress level σ_i , and n_i is the number of cycles incurred at stress σ_i . The condition $D_f = 1$ is considered to result in failure due to fatigue. This estimation method has an accepted accuracy of around $\pm 50\%$.

6.5. Blade Design Criteria

The design of turbomachinery blades must satisfy three major criteria in addition to static stress requirements:

- Avoid HCF
- Adequate LCF life
- Adequate creep life

Steady-state blade stresses must be computed for a given blade design in order to inform design against HCF and creep. Below, a number of stresses to which a turbomachinery blade is subject during steady operation are analyzed.

6.5.1. Centrifugal Stress. As was noted in Sec. 6.2, a point mass translating along a path displaced from its instantaneous center of rotation is subject to a centripetal force. In the case of a blade rotating about a shaft along a circular path at a constant rotational rate Ω , each differential radial blade element of height dr is subject to an inertial force

$$F = \delta m(r\Omega^2) = \rho A dr(r\Omega^2), \quad (6.4)$$

where A is the blade cross-sectional area and ρ is the density of the blade material. When considered in the frame of reference attached to the blade, this is manifest as a centripetal force in the outward radial direction. This has the important consequence that the blade is subject to a *tensile* applied load. Applying a static force balance on the differential blade element as in Fig. 6.7 gives

$$(\sigma + d\sigma)(A + dA) + F - \sigma A = 0, \quad (6.5)$$

from which the differential form of the blade stress expression is obtained as

$$Ad\sigma + \sigma dA = -\rho A\Omega^2(rdr). \quad (6.6)$$

This equation shows that both the local blade radial stress $\sigma(r)$ and cross-sectional area $A(r)$ may vary with radial position. If a profile is selected for one of these

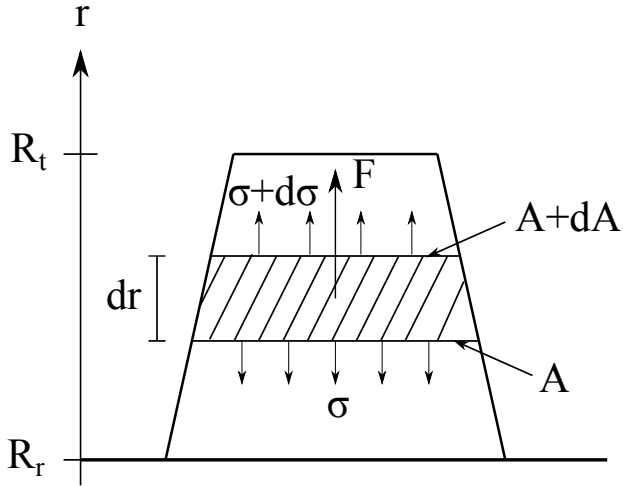


Figure 6.7: Force balance on a blade rotating about a shaft at steady-state.

variables, the other may then be directly determined. Below, two such cases are considered.

6.5.1.1. *Constant Section Blade:* $dA = 0$. Following Eq. 6.6, this gives

$$Ad\sigma + \rho A\Omega^2 r dr = 0 d\sigma = -\rho\Omega^2 r dr \sigma(r) = -\frac{\rho\Omega^2}{2} r^2 + c, \quad (6.7)$$

where c is a constant of integration. Applying the boundary condition $\sigma(R_t) = 0$, where R_t is the tip radius gives $c = \frac{\rho\Omega^2}{2} R_t^2$, and thus

$$\sigma(r) = \frac{\rho\Omega^2}{2} (R_t^2 - r^2). \quad (6.8)$$

From this equation, the blade location with the maximum radial stress is thus the position of minimum radius i.e. the blade root at $r = R_r$. The variation of radial blade stress with radial position for this blade geometry is shown in Fig. 6.8.

6.5.1.2. *Optimum Blade:* $\sigma(r) = \sigma_0 = \text{const.}$. Following Eq. 6.6 with $d\sigma = 0$, this gives

$$\frac{dA}{A} = -\frac{\rho\Omega^2}{\sigma_0} (r dr) \ln \left(\frac{A}{A_r} \right) = -\frac{\rho\Omega^2}{2\sigma_0} (r^2 - R_r^2), \quad (6.9)$$

where A_r is the area at the blade root $r = R_r$, and thus

$$A(r) = A_r \exp \left[-\frac{\rho\Omega^2}{2\sigma_0} (r^2 - R_r^2) \right] \quad (6.10)$$

The area profile required for a constant radial stress profile is thus seen to be an exponential decay, and is shown in Fig. 6.9. It is important to note that a constant stress is only achieved in this manner for a blade of infinite radius. However, a reasonable approximation may be achieved for blades with a low hub-tip radius ratio.

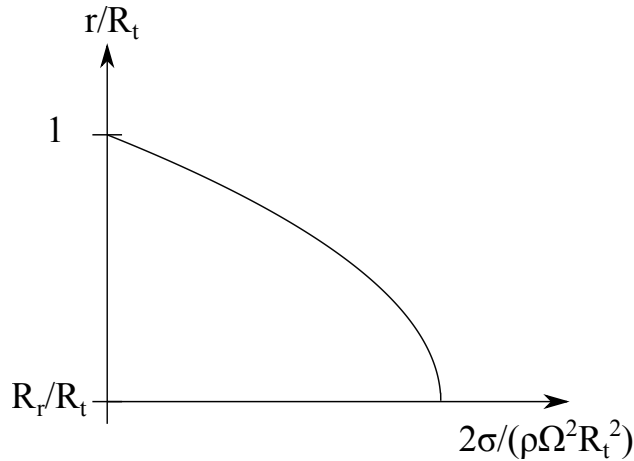


Figure 6.8: Variation of radial stress with radial position in a blade of constant cross-sectional area at steady-state conditions.

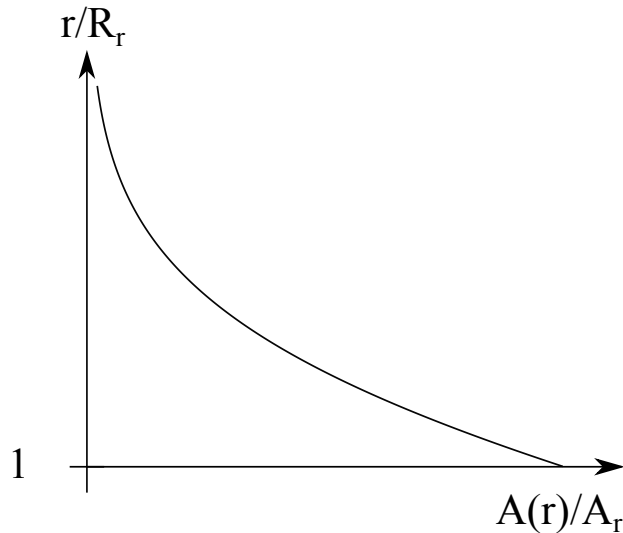


Figure 6.9: Variation of cross-sectional area with radial position for a blade with constant radial stress at steady-state conditions.

6.5.2. Gas Bending. In addition to the inertial stresses associated with rotation, blades also incur aerodynamic loading. The rotating blade causes a change in the gas momentum, and hence experiences a reaction force. This reaction force results in a bending moment, as shown in Fig. 6.10. The reaction force incurred by the blade is a result of the leading-edge and trailing-edge blade angles employed, which

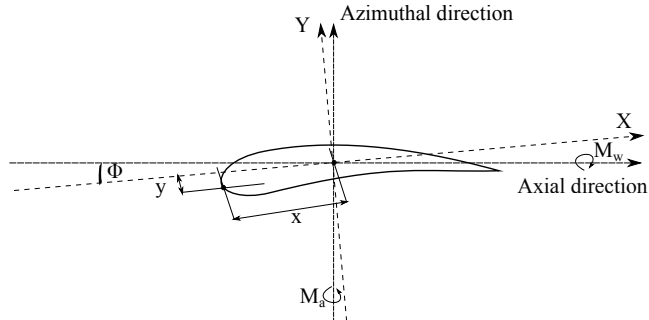


Figure 6.10: Principal axes associated with gas bending stress and associated bending moments along local coordinate axes.

are selected to ensure fully-attached flow along the length of the blade according to the Kutta condition. Attaching a coordinate system (X, Y) to the center of pressure of the blade and aligning it with the resultant forces applied at that point such that bending moments in the plane of the blade cross-section are eliminated, then a gas bending stress σ_{gb} about the principal axis can be defined from bending theory as

$$\sigma_{gb} = \frac{x}{I_{yy}} (M_a \cos \Phi - M_w \sin \Phi) - \frac{y}{I_{xx}} (M_w \cos \Phi - M_a \sin \Phi), \quad (6.11)$$

where $I_{xx} = \int y^2 dm$ and $I_{yy} = \int x^2 dm$ are the second moments of inertia in the (X, Y) coordinate system, (x, y) are the distances in (X, Y) coordinates from the center of pressure to the leading edge point, Φ is the transformation angle between the nominal flow-aligned coordinate system and the (X, Y) system, and M_w and M_a are the bending moments about the flow-aligned axial and azimuthal directions, respectively. The gas bending stress can be shown to be a tensile stress. For conventional blade geometries, $M_w \gg M_a$ and $\Phi \approx 0$, giving

$$\sigma_{gb} \approx \frac{y}{I_{xx}} M_w = f(\Delta u_\theta, n, h, c), \quad (6.12)$$

where Δu_θ is the azimuthal velocity change (related to the stage work), n is the number of blades, h is the blade height and c is the blade chord length.

Bibliography

- [1] Y. A. Cengel and M. A. Boles. *Thermodynamics: An Engineering Approach*. McGraw-Hill, 7th edition, 2010.
- [2] W. C. Reynolds and H. C. Perkins. *Engineering Thermodynamics*. McGraw-Hill, 2nd edition, 1977.
- [3] J. D. Anderson Jr. *Introduction to Flight*. McGraw-Hill, 7th edition, 2012.
- [4] J. D. Anderson Jr. *Modern Compressible Flow: With Historical Perspective*. McGraw-Hill, 7th edition, 2004.
- [5] J. Mattingly. *Gas Turbines and Rockets*. American Institute of Aeronautics and Astronautics, 2006.
- [6] H. I. H. Saravanamuttoo, G. F. C. Rogers, H. Cohen, and P. V. Straznicky. *Gas Turbine Theory*. Pearson Education, 2008.
- [7] P. Hill and C. Peterson. *Mechanics and Thermodynamics of Propulsion*. Addison-Wesley, 1992.
- [8] A. H. Lefebvre. *Gas Turbine Combustion*. Taylor & Francis, 2nd edition, 1999.
- [9] S. Farokhi. *Aircraft Propulsion*. Wiley, 2009.
- [10] N. N. Cumpsty. *Jet Propulsion - A Simple Guide to the Aerodynamic and Thermodynamic Design and Performance of Jet Engines*. Cambridge University Press, 1997.
- [11] *The Jet Engine - A Complete Overview of the Modern Gas Turbine*. Key Publishing, 6th edition, 2005.
- [12] J. B. Heywood. *Internal Combustion Engine Fundamentals*. McGraw-Hill, 1988.
- [13] R. Stone. *Introduction to Internal Combustion Engines*. Palgrave MacMillan, 3rd edition, 1999.
- [14] J. L. Lumley. *Engines-An Introduction*. Cambridge University Press, 1999.
- [15] G. P. Sutton and O. Biblarz. *Rocket Propulsion Elments*. Wiley, 2010.
- [16] D. K. Huzel and D. H. Huang. *Modern Engineering for Design of Liquid-Propellant Rocket Engines*. American Institute of Aeronautics and Astronautics, 1992.
- [17] W. G. Vincenti and C. H. Kruger. *Introduction to Physical Gas Dynamics*. John Wiley, 1965.
- [18] B. J. McBride, M. J. Zehe, and S. Gordon. NASA Glenn coefficients for calculating thermodynamic properties of individual species. NASA/TP-2002-211556, NASA, 2002.
- [19] C. K. Law. *Combustion Physics*. Cambridge University Press, Cambridge, 2006.
- [20] Arijana Bušić, Nenad Mardetko, Semjon Kundas, Galina Morzak, Halina Belskaya, Mirela Ivanić Šantek, Draženka Komes, Srđan Novak, and Božidar Šantek. Bioethanol production from renewable raw materials and its separation and purification: A review. *Food Technology and Biotechnology*, 56(3):289–311, 2018.
- [21] Biodiesel production and distribution, https://afdc.energy.gov/fuels/biodiesel_production.html.
- [22] Ethanol, <https://afdc.energy.gov/fuels/ethanol.html>.
- [23] Biodiesel, <https://afdc.energy.gov/fuels/biodiesel.html>.
- [24] G. I. Taylor. The mechanics of swirl atomisers. *Proceedings of the 7th International Congress for Applied Mechanics*, 1948.
- [25] E. Giffen and A. Muraszew. *The Atomisation of Liquid Fuels*. John Wiley and Sons Inc., 1953.

- [26] D. P. Schmidt, I. Nouar, P. K. Senecal, C. J. Rutland, J. K. Martin, and R. D. Reitz. Pressure-swirl atomization in the near field. *SAE Technical Paper 1999-01-0496*, 1999.
- [27] P. K. Senecal, D. P. Schmidt, I. Nouar, C. J. Rutland, R. D. Reitz, and M. L. Corradini. Modeling high-speed viscous liquid sheet atomization. *Int. J. Multiphase Flow*, 25:1073–1097, 1999.
- [28] P. J. O'Rourke and A. A. Amsden. The tab method for numerical calculation of spray droplet breakup. *SAE Technical Paper 872089*, 1987.